IMPROVING THE REPRESENTATION OF IRRIGATION AND GROUNDWATER IN GLOBAL LAND SURFACE MODELS TO ADVANCE THE UNDERSTANDING OF HYDROLOGY-HUMAN-CLIMATE INTERACTIONS

By

Farshid Felfelani

A DISSERTATION

Submitted to
Michigan State University
in partial fulfillment of the requirements
for the degree of

Civil Engineering – Doctor of Philosophy

2019

ABSTRACT

IMPROVING THE REPRESENTATION OF IRRIGATION AND GROUNDWATER IN GLOBAL LAND SURFACE MODELS TO ADVANCE THE UNDERSTANDING OF HYDROLOGY-HUMAN-CLIMATE INTERACTIONS

By

Farshid Felfelani

Hydrological models and satellite observations have been widely used to study the variations in the Earth's hydrology and climate over multitude of scales, especially in relation to natural and human-induced changes in the terrestrial water cycle. Yet, both satellite products and model results suffer from inherent uncertainties, calling for the need to improve the representation of critical processes in the models and to make a combined use of satellite data and models to examine the variations in the terrestrial hydrology. The representation of irrigation and groundwater—two major hydrologic processes with complex reciprocal interplay—in large-scale hydrological models is rather poorly parameterized and heavily simplified, hindering our ability to realistically simulate groundwater-human-climate interactions. This dissertation advances the physical basis for irrigation and groundwater parameterizations in global land surface models, leveraging the potential of emerging satellite data (i.e., data from GRACE and SMAP satellite missions) toward a more realistic quantification of the impacts of human activities on the hydrological cycle. A comprehensive global analysis is developed to examine the historical spatial patterns and long-term temporal response, i.e., the terrestrial water storage (TWS), of two models to natural and human-induced drivers. Human-induced changes in TWS are then quantified in the highly managed global regions to identify the uncertainties arising from a simplistic representation of irrigation and groundwater. The potential of improving irrigation representation in the Community Land Model version 4.5 (CLM4.5) is then investigated by assimilating the soil moisture data from SMAP satellite mission using 1-D Kalman Filter assimilation approach. The new irrigation scheme is then tested over the heavily irrigated central U.S. Next, the existing groundwater module of CLM5 is broadly evaluated over conterminous U.S. and a new prognostic groundwater module is implemented in CLM5 to account for lateral groundwater flow, pumping, and conjunctive water use for irrigation. In particular, an explicit parameterization for the steady-state well equation is introduced for the first time in large-scale hydrological modeling. Finally, the impacts of climate change on global TWS variabilities and the implications on sea level change are examined for the entire 21^{st} century using multi-model hydrological simulations. The key findings and conclusions from the aforementioned multi-scale analysis and model developments are: (1) in terms of TWS, notable differences exist not only between simulations of hydrological models and GRACE but also among different GRACE products, therefore, TWS variations from a single model cannot be reliably used for global analyses; (2) these differences significantly increase in projections of TWS under climate change, however, models agree in sign of change for most global areas; (3) TWS is expected to decline in many regions in southern hemisphere, but increase in northern high latitudes, projected to accelerate sea level rise by the mid- and late-21^{st} century; (4) constraining the target soil moisture in CLM4.5 using SMAP data assimilation with 1-D Kalman Filter reduces the bias in the simulated irrigation water by up to 60% on average, improving irrigation and soil moisture simulations in CLM4.5; (5) the new groundwater model significantly improves the simulation of groundwater level change and promisingly captures most of the hotspots of groundwater depletion across the U.S. overexploited aquifers; and (6) the simulation with the lateral groundwater flow substantially enhances the TWS trends relative to the default CLM5. These results and findings could provide a basis for improved large-scale irrigation and groundwater modeling and improve our understanding of hydrology-human-climate interactions.

To my wife, my love, Behnaz

ACKNOWLEDGEMENTS

I would like to express my gratitude to all who have contributed to my Ph.D. research. In the first place, I am deeply grateful to my Ph.D. advisor, Dr. Yadu Pokhrel, for his great mentoring, support, illuminating guidance and encouragement throughout my doctoral program. I would also like to express my great appreciation to my committee members, Dr. Shu-Guang Li, Dr. Phanikumar Mantha, and Dr. Kyla Dahlin for their persistent help and meticulous comments and suggestions. This dissertation was partially supported by the National Science Foundation (Award #: 1752729). I gratefully acknowledge the high-performance computing support from the Institute for Cyber-Enabled Research at Michigan State University and Cheyenne provided by NCAR's Computational and Information Systems Laboratory (doi:10.5065/D6RX99HX). I thankfully acknowledge Dr. David Lawrence, Dr. Yoshihide Wada, Dr. Laurent Longuevergne, and Dr. Kaiyu Guan, my co-authors in Chapter 2 and Chapter 3, for being critical to my research and providing helpful comments. I am thankful to Dr. Jonas Jägermeyr for providing irrigation data. I also wish to extend my thanks to the ISIMIP group for providing simulation results and sharing invaluable thoughts for Chapter 5. I am thankful of my dear friends Sanghoon Shin, Suyog Chaudhari and Mateo Burbano for their fruitful discussions and spending cheerful time together. God has blessed me in so many ways, but the biggest of all is my wonderful family. I wish to express my most special appreciation to my dear parents, Ahmad and Marziyeh, and to my kind sisters, Mahshid and Parichehr, for all the love they have given me and for helping me to shape my life.

TABLE OF CONTENTS

LIST OF TABLES

LIST OF FIGURES

CHAPTER 1

1. Introduction

1.1. Research Motivation

1.1.1. Global Freshwater Systems and Human Land-Water Management Activities

The question of how terrestrial water systems have been changing under the dual influence of natural climate variability and increasing human activities (e.g., damming, flow regulation, groundwater pumping, and irrigation) has been a subject of growing concern and debate in the face of increasing water scarcity and crisis around the world (Alley et al., 2002; Famiglietti, 2014; Fan, 2015; Gleeson et al., 2012). Profound changes in regional terrestrial water storages such as the stores in rivers and groundwater systems have been reported, which are suggested to have been primarily caused by the acceleration in human alteration of land and water systems, and unsustainable use of freshwater resources (Giordano, 2009; de Graaf et al., 2019; Pokhrel, Hanasaki, Yeh, et al., 2012; Pokhrel et al., 2015; Rodell et al., 2009; Scanlon, Faunt, et al., 2012; Trancoso et al., 2017). The changes in regional terrestrial water storages not only affect terrestrial hydrologic systems but also exert influence on the climate systems (Boucher et al., 2004) and contribute to the global mean sea level (GMSL) change (Pokhrel, Hanasaki, Yeh, et al., 2012; Wada et al., 2016). However, the lack of long-term and continuous in-situ observations of water, carbon, and energy fluxes and states worldwide restricts our ability to fully understand the changing dynamics of the hydrology-human-climate interactions and the impacts on freshwater systems and discharge to oceans (Alley et al., 2002; Döll et al., 2016; Pokhrel et al., 2016; R. G. Taylor et al., 2013).

Large-scale (i.e., regional to global) hydrological models play an irreplaceable role to bridge this gap by providing a spatially complete and temporally continuous simulations of hydrological fluxes and stores for a verifiable assessment and a realistic prediction of water resources by representing the effects of human activities and climate change. Large number of global terrestrial hydrology models have been developed in the recent past. The earliest efforts to incorporate the human impacts in hydrological models were made in the early 2000s by implementing simple irrigation schemes (i.e., with simple parameterizations for irrigation water calculations, crops, and sources of water withdrawal, etc.) in the WaterGAP (Alcamo et al., 1997; Döll et al., 1999; Döll & Siebert, 2002) and ORCHIDEE (de Rosnay et al., 2003; Vérant et al., 2004) models. Noteworthy progress has been made since then to improve the large-scale hydrological models from different aspects (Bierkens, 2015) and to advance the representation of anthropogenic water management (Döll et al., 2012; Koirala et al., 2014; Pokhrel, Hanasaki, Koirala, et al., 2012; Wada et al., 2014, 2017). However, the emphasis was initially put more on improving hydrological fluxes such as river discharge and evapotranspiration and less on terrestrial water storage (TWS) due the challenges in explicitly representing all TWS components (Haddeland, Lettenmaier, et al., 2006; Liang et al., 2003; Overgaard et al., 2006; Pitman, 2003; Pokhrel, Hanasaki, Yeh, et al., 2012; Pokhrel et al., 2015).

Further, physically-based advancements of the models' subsurface representation, including the enhancement of soil configuration, coupling of prognostic groundwater model, and improvement of boundary conditions in the soil column (Fan et al., 2007; Maxwell & Miller, 2005; Pokhrel et al., 2015; X. Zeng & Decker, 2009), have led to more accurate simulation of TWS in some of the hydrological models. These advancements have enabled us to quantify the contribution of the human activities to the changes in freshwater systems over the past century and thereby to partition the total TWS change into the natural and human-induced changes; however, the progress has been hindered by the inability to capture the effects of heterogeneity present, especially below the land surface (Sivapalan, 2018). Further, the use of coarse grid resolution in global studies has inhibited the representation of many processes that are relevant at fine scales (e.g., lateral ridge-to-valley surface and groundwater flow, capturing sunny and shady slopes processes in the context of hillslope hydrology) and therefore, the representation of the subsurface dynamics is relatively simplistic in most global models (Pokhrel et al., 2015, 2016), mainly due to our limited knowledge of the subsurface (Fan et al., 2019). Another aspect of human impact representation in large-scale models that remains still poorly characterized is irrigation, which accounts for the largest portion of human water use globally and is known to affect land hydrology and climate over varying spatial (local to global) and temporal scales (e.g., long-term climate and short-term weather fluctuations). Therefore, challenges remain in better parameterizing irrigation, groundwater, and aquifer pumping on a physical basis to better capture sub-(surface) heterogeneity and the fine-scale details of land-water management practices.

1.1.2. Advancing Irrigation and Groundwater Representation in Hydrological Models to Improve Our Understanding of Human Impacts on the Water Cycle

Irrigation water use, which accounts for ~90% of consumptive water use globally (Döll, 2002; Scanlon, Faunt, et al., 2012) and ~40% of total freshwater withdrawals in the U.S. (Dieter et al., 2018), has increased significantly over the past several decades and is expected to increase further in the future due to growing food demands and rising temperatures (Haddeland et al., 2014; Wada et al., 2015). As such, irrigation modeling has become a subject of intense research for hydrology, water resources, and climate modeling communities, due to its importance for both practical applications and scientific investigations (Pokhrel et al., 2016). Irrigation not only affects local (first-order) to regional (second-order) water resources (Kustu et al., 2010), but also alters local to regional climate system (Boucher et al., 2004; J. Jin & Miller, 2011; Lo & Famiglietti, 2013; Pei et al., 2016; Wei et al., 2012) as well as short-term weather fluctuations (Yamada & Pokhrel, 2019) through changes in surface energy budget (Ozdogan et al., 2010; Pokhrel, Hanasaki, Koirala, et al., 2012) and carbon fluxes (Foley et al., 2005). For example, intensive irrigation in California's Central Valley Aquifer (CVA) changes local climate and water resources but also strengthens water vapor transport toward the southwest, increasing summer precipitation in the southwestern US by 15% and streamflow in the Colorado River by 30% (Lo & Famiglietti, 2013). There have also been clear evidences that development of irrigation in the U.S. High Plains Aquifer (HPA) has increased downwind summer precipitation by 20-30%, consequently increasing late-summer streamflow in the Midwest.

Mechanistically, irrigational pumping first enhances soil moisture (i.e., by removing water from deep in the ground and adding it to the land surface), then impacts surface energy fluxes (e.g., evapotranspiration and atmospheric water vapor), and eventually affects precipitation in the regions with strong land-atmosphere (i.e., soil moisture-precipitation) coupling mainly in the northern hemisphere (Koster, 2004). Today, there is a growing number of global land surface models (LSMs) that can be potentially coupled with atmospheric/climate models to simulate irrigation and examine the hydrologic and climate impacts at regional to global scales (Nazemi & Wheater, 2015a; Pokhrel et al., 2016).

Despite of all the progress that have been made, outstanding challenges and opportunities still remain to better simulate irrigation water requirement and soil moisture (SM) in irrigated areas (e.g., by refining the grid resolution and benefiting from new high resolution datasets to better represent the land surface and subsurface heterogeneity) (Nazemi & Wheater, 2015a; Pokhrel et al., 2016; Wada et al., 2017). For example, the threshold and target SM, as the key variables in the irrigation schemes used in many LSMs, have been set to largely varying values in different studies because no guidelines or data exist on the thresholds used by farmers in different regions (Haddeland, Lettenmaier, et al., 2006; Harding & Snyder, 2012; Lawston et al., 2015; Ozdogan et al., 2010; Pokhrel, Hanasaki, Koirala, et al., 2012; Sorooshian et al., 2011; Vahmani & Hogue, 2014; X. Z. Zhang et al., 2017).

Such differences in the representation of irrigation can lead to strongly varying irrigation estimates among models (Pokhrel et al., 2016), which in turn can result in a varying degree of change in surface energy balance and associated climate impacts. Moreover, the spatially-constant bulk coefficients and parameters employed in the threshold and target SM parameterizations in most irrigation schemes cause a small temporal and spatial variability of threshold and target SM which in turn underrepresent the heterogeneity in irrigation attributes (e.g., irrigation practices, crop-specific water requirements, and irrigation timing).

Further uncertainties can be added in irrigation modeling due to uncertainties in other model parameterizations that are coupled with irrigation, which include an inaccurate representation of crop phenology and crop calendar (Peng et al., 2018) and oversimplification in the simulation of water availability and extraction from surface water and groundwater resources. In particular, groundwater dynamics in large-scale hydrological models is rather poorly parameterized (e.g., linear representation of groundwater, lack of SM-groundwater interactions, lack of lateral groundwater flow, fixed allocation of total irrigation withdrawals to surface water and groundwater sources, lack of fully-coupled surface water-groundwater representation) or even completely ignored in many models (Döll et al., 2012; Leng et al., 2015; Pokhrel et al., 2015; Wada et al., 2014; Y. Zeng et al., 2018).

For example, in the Community Land Model (CLM) which is a state-of-the-art LSMs that is widely used globally, despite the presence of a bulk aquifer reservoir at the bottom of the soil layer, irrigation water is only extracted from surface water (i.e., from the total runoff in version 4.5 and from river water storage and ocean model in version 5) as the sole and unlimited source for irrigation (Lawrence et al., 2011, 2019; Leng, Huang, Tang, Sacks, et al., 2013). Considering the coarse resolution in global simulations (e.g., 0.5°), the lateral groundwater flow is assumed to be insignificant and hence ignored (Krakauer et al., 2014), which is not anymore a valid assumption in higher resolution model grids (e.g., <0.05°) (Y. Zeng et al., 2018). Further, another key characteristic of groundwater model in CLM is the unlimited amount of water in the aquifer as well as unlimited source of irrigation water which, for example, results in unrealistic response to drought periods (Swenson & Lawrence, 2015). To address these issues and toward developing a comprehensive irrigation modeling framework (i.e., consistently integrates surface water, groundwater, and irrigation system), it is essential to improve the representation of groundwater and irrigation interactions by explicitly simulating groundwater pumping and water table dynamics globally, combined with other recent advancements in the literature, e.g., implementation of lateral groundwater flow and accounting for a realistic conjunctive water use for irrigation.

1.1.3. Leveraging the Potential of Emerging Satellite Data in the Hydrological Modeling

In recent years, emerging satellite-based observations related to hydrological fluxes and states have significantly enhanced our ability to map the global heterogeneity in hydrology, to monitor and investigate the changes in global freshwater systems and thus, to enhance sustainable water resources management (Sheffield et al., 2018). The satellite products and hydrological models complement each other; the use of information from the satellites in combination with hydrological models has transformed the way we study global hydrology in many different ways (van Dijk & Renzullo, 2011; Famiglietti et al., 2015). Satellite data have been extensively used to validate model simulations, particularly over regions with poor in-situ observation networks and for the hydrological variables that are difficult to measure at site (e.g., TWS) (Alkama et al., 2010; Decharme et al., 2010; Döll et al., 2014; Eicker et al., 2016; Freedman et al., 2014; Grippa et al., 2011; Landerer et al., 2010, 2013; Rosenberg et al., 2013; Swenson & Lawrence, 2015; H. Xie et al., 2012; Yang et al., 2011).

Satellite data assimilation techniques have been utilized to improve global hydrological simulations. For example, the TWS derived from the Gravity Recovery and Climate Experiment (GRACE) satellite mission as well as the remotely sensed SM products from the satellites such as the Soil Moisture Active Passive (SMAP) have been assimilated into the land surface or ecosystem models to enhance the estimate of various hydrological components such as TWS and SM (X. Chen et al. 2017; Eicker et al. 2014; Girotto et al. 2016; Houborg et al. 2012; Li et al. 2012; Li and Rodell 2015; Zaitchik, Rodell, and Reichle 2008; Khaki and Awange 2019; Alvarez-Garreton et al., 2016; He et al., 2017; Kumar et al., 2015; Lievens et al., 2017, 2015).

SMAP, launched in 2015, is one of the most recent satellite missions of the National Aeronautics and Space Administration (NASA) with hydrologic applications that provides global surface SM retrievals with original spatial resolution of 36 km from its radiometer instrument. Numerous studies have evaluated SMAP data with ground-based observations (Chan et al., 2016; M. Pan et al., 2016), showing that SMAP generally provides SM data with lower errors across different climate regions compared to the other remotely sensed SM products (Kumar et al., 2018). A recent study reported that SMAP data can also be used to detect the seasonal timing and spatial signature of irrigation (Lawston, Santanello Jr., & Kumar, 2017). Given the increasing length of SMAP data record and the high-quality data, there has been an increased use of SMAP data in hydrologic research. However, to my best knowledge, the potential of using SMAP data to improve irrigation modeling by mimicking the heterogeneity in irrigation has not yet been examined. All in all, the improvements in the physics and structure of the models in concert with the emerging indispensable satellite remote sensing have enhanced our understanding of the big picture of global hydrological changes (Famiglietti et al., 2015).

1.1.4. Global TWS under Climate Change and the Implications on GMSL

One of the primarily goals in large-scale hydrologic studies—towards which efforts for models' advancements are directed—is to investigate the impacts of climate change on terrestrial hydrology and to assess the resulting consequences on other global changes such as drought severity, flood occurrence and GMSL change. TWS is an inclusive compartment of terrestrial hydrology which represents water resources availability and is inherently linked to droughts, floods, and GMSL change (Pokhrel, Hanasaki, Yeh, et al., 2012; Reager et al., 2016; Tapley et al., 2019; Thomas et al., 2014; Wada et al., 2016; M. Zhao et al., 2017). Evaluation of the GMSL budget shows that land water/hydrology (other than ice sheets and glaciers) is one of the key contributors to the GMSL change; however, the magnitude and even the net sign of its contribution remain uncertain and heavily debated (Chambers et al., 2017; Reager et al., 2016; Wada et al., 2016). While a large body of literature exist on the impacts of projected climate change and socio-economic scenarios on global water availability and use, water scarcity, runoff, and river discharge (Alcamo et al., 2003; Arnell, 1999, 2004; Gosling & Arnell, 2016; Haddeland et al., 2014;

Hanasaki et al., 2013a, 2013b; Oki & Kanae, 2006; Schewe et al., 2014; Veldkamp et al., 2017), impacts of projected climate change on TWS, GMSL change, and drought severity are currently unknown.

The high uncertainties in the projections of climate models in magnitude and even sign of changes, together with the secondary uncertainties associated with the physics and structure of different components in hydrological models make our assessment of the climate change impacts on hydrology and water resources highly uncertain (Schewe et al., 2014). Therefore, it is essential to bring together a large ensemble of global terrestrial hydrologic simulations forced by different climate models outputs under the various climate change scenarios to first, reduce the above uncertainties in the analysis and second, to encompass a wide range of future scenarios of greenhouse gases concentration and socio-economic conditions describing the human influences such as land use and land management in response to growing population and water demand (Frieler et al., 2017).

Leveraging the multi-model simulations of TWS projection from a large ensemble of hydrological models, the future projections of global TWS change can be investigated under different climate change and socio-economic scenarios. Future global hotspots of TWS deficit can be detected and from a broader perspective, the future TWS contribution to the GMSL can be quantified, as yet rarely investigated.

1.2. Research Goal, Science Questions, and Objectives

As discussed above, there are both gaps/challenges and opportunities to improve hydrological models to advance our understanding of hydrology-human-climate interactions. The necessity of using hydrological models to quantify the influence of human activities on terrestrial hydrology (Section 1.1.1) and the need to advance the simplified representation of irrigation and groundwater schemes in hydrological models (Section 1.1.2) by leveraging the available data from satellite missions (Section 1.1.3) lead me to pursue the **overarching goal** of my Ph.D. dissertation, which is to advance our understanding of hydrology-human-climate interactions by improving the irrigation and groundwater parameterizations in the large-scale hydrological models. The advancements in irrigation and groundwater models enhance the surface water-groundwater-irrigation coupling and aquifer depletion simulation which then have broader hydrological applications toward assessing the impacts of terrestrial hydrology on GMSL change as well as the food, energy, and water nexus under climate change. I ask the following overarching scientific question: How can we overcome some of the critical existing challenges in the state-of-the-art global LSMs by utilizing novel approaches and emerging datasets? This overarching question is addressed by answering the specific science questions under each chapter of the dissertation followed by the objectives.

Chapter 2. How are human land-water management activities affecting the spatial and temporal patterns of global terrestrial water storage variations?

Obj. 1: Examine the historical spatiotemporal variations in TWS over global river basins to explain water deficits worldwide.

Obj. 2: Quantify the contribution of human activities to the total TWS variations.

Obj. 3: Assess the contribution of different TWS components (e.g., snow water, river discharge, SM, and groundwater) to the total TWS variations over different global regions/basins.

Chapter 3. Can irrigation parameterizations in global land surface models be improved by using the emerging soil moisture data from satellites?

Obj. 1: Present a parsimonious parameterization for SMAP SM extrapolation to the entire root zone.

Obj. 2: Enhance irrigation representation in large-scale hydrological models by assimilating SMAP data in the target SM parameterization using a 1-D Kalman Filter (KF) in CLM version 4.5 (CLM4.5).

Chapter 4. How can we improve the simulation of groundwater dynamics and pumping-induced aquifer storage change in global land surface models?

Obj. 1: Implement a prognostic groundwater module which accounts for lateral groundwater flow, conjunctive use of groundwater and surface water for irrigation, and pumping in the CLM version 5 (CLM5).

Obj. 2: Examine the role of lateral groundwater flow on simulation of continental-level groundwater and TWS.

Obj. 3: Investigate the impacts of conjunctive surface water-groundwater use for irrigation over groundwater and TWS dynamics.

Chapter 5. How will the global terrestrial water storage change under climate change?

Obj. 1: Quantify the variations in global TWS under climate change scenarios and detect the future global hotspots of TWS deficit.

Obj. 2: Investigate the implications of projected global TWS change on GMSL change under climate change and explore whether the land hydrology have its current positive contribution to GMSL change under climate change scenarios.

The scientific question and objectives posed in Chapter 2 are addressed by using the global simulations from two hydrological models, i.e., HiGW-MAT (Pokhrel et al., 2015; Pokhrel, Hanasaki, Koirala, et al., 2012) and PCR-GLOBWB (van Beek et al., 2011; Wada et al., 2010). The new irrigation scheme in Chapter 3 and groundwater model in Chapter 4 are implemented in CLM4.5 and CLM5, respectively, and verified across highly irrigated and data-rich regions in U.S. i.e., CVA and HPA. While the present model development is conducted at regional and continental scales (chosen to reduce the computational cost), the newly developed approaches can be incorporated into any LSM and applied and validated globally. Finally, the scientific question and objectives posed in Chapter 5 are addressed by utilizing the global simulations of future projections of TWS under climate change from seven terrestrial hydrology models, namely five global hydrological models (GHMs): CWatM (Burek et al., 2019), H08 (Hanasaki et al., 2008a, 2008b, 2018), MPI-HM (Stacke & Hagemann, 2012), PCR-GLOBWB (Wada et al., 2014), and WaterGAP (Müller Schmied et al., 2016); one global LSM: CLM4.5 (Oleson et al., 2013); and one dynamic global vegetation model (DGVM): LPJmL (Bondeau et al., 2007).

1.3. Dissertation Outline

The research questions of this dissertation are addressed in separate chapters (Chapter 2 through Chapter 6). A brief summary of the remaining five chapters is provided as below.

Chapter 2. Natural and Human-induced Terrestrial Water Storage Change: A Global Analysis using Hydrological Models and GRACE

The global spatiotemporal TWS variations are investigated and TWS variations are attributed to climate and human-induced factors.

Chapter 3. Utilizing SMAP Soil Moisture Data to Improve Irrigation Parameterization in Land Surface Models

A new irrigation modeling framework is presented that assimilated SMAP SM data to set the target SM in LSMs.

Chapter 4. Implementing a Prognostic Groundwater Model with Lateral Groundwater Flow, Conjunctive Water Use for Irrigation and Pumping

Continental-scale groundwater simulations, including lateral flow and pumping, are improved by using a newly developed groundwater scheme for CLM5

Chapter 5. Global Terrestrial Water Storage Change under Climate Change and Implications on Global Mean Sea Level

The future projections of the global TWS is investigated and the implications on the GMSL change is quantified by using multi-model ensemble global hydrological simulations.

Chapter 6. Summary and Conclusions

CHAPTER 2

2. Natural and Human-induced Terrestrial Water Storage Change: A Global Analysis using Hydrological Models and GRACE

Based on:

Felfelani, F., Wada, Y., Longuevergne, L., & Pokhrel, Y. N. (2017). Natural and human-induced terrestrial water storage change: A global analysis using hydrological models and GRACE. Journal of Hydrology, 553, 105–118. https://doi.org/10.1016/j.jhydrol.2017.07.048.

2.1. Introduction

The question of how freshwater systems are changing under the dual influence of climate variability and increasing human water exploitation has been a topic of great concern and debate in the face of growing water scarcity around the world (Alley et al., 2002; Famiglietti, 2014; Fan, 2015; Gleeson et al., 2012). Ground-based monitoring of surface water and groundwater systems suggests profound changes in surface water flows and groundwater storages globally due to accelerating human alteration of land and water systems (Giordano, 2009; Scanlon, Faunt, et al., 2012) which can be both direct, e.g., flow regulation and groundwater pumping and indirect, e.g., changes in climate forcing, CO_2 concentrations and impacts on photosynthetic activities (Trancoso et al., 2017). However, the lack of in-situ observations worldwide limits our understanding of the dynamic relationship between natural climate variability and direct and indirect human impacts (HI) on freshwater systems (Alley et al., 2002; Döll et al., 2016; R. G. Taylor et al., 2013). Large-scale hydrological models play an irreplaceable role in filling this data gap and provide an improved understanding of the changes in the water cycle, which is crucial for the accurate assessment and realistic prediction of water availability and use. In recent years, satellite-based observations of water flows and storages have substantially advanced our ability to better monitor the changing water systems at the global scale. In particular, the combined use of the satellite data and hydrological models has revolutionized the way we study global freshwater systems (van Dijk & Renzullo, 2011; Famiglietti et al., 2015).

Large-scale hydrological models have been widely used to study global freshwater systems and human water use (Nazemi & Wheater, 2015b; Pokhrel et al., 2016). These models can be classified into two general types: (i) land surface models (LSMs) and (ii) global hydrological models (GHMs) (Haddeland et al., 2011). LSMs, such as the MATSIRO (Takata et al., 2003) and CLM (Lawrence et al., 2011), are designed to simulate the land hydrology within the general circulation models (GCMs) and Earth system models (ESMs), but GHMs, such as the WaterGAP (Alcamo et al., 2003; Döll et al., 2003) and PCR-GLOBWB (van Beek et al., 2011; Wada et al., 2010), have been traditionally developed as stand-alone models for offline water resource assessment. While LSMs simulate various hydrological processes on a physical basis and solve both surface water and energy balances at the land surface, GHMs simulate these processes using relatively simple and conceptual approaches even though they are more comprehensive in simulating human land-water management practices (Pokhrel et al., 2016). As such, LSMs and GHMs have certain limitations in simulating the natural or human-induced changes in various branches of the water cycle. In particular, despite noteworthy progress that has been made in model improvements over the years (Overgaard et al., 2006; Pitman, 2003; Sellers et al., 1997), water table dynamics and groundwater pumping still remain largely ignored or poorly simulated (Nazemi

& Wheater, 2015b; Pokhrel et al., 2016), making the models incapable of accurately capturing subsurface water flows and storages in general, and the human-induced groundwater storage depletion in particular. While the hydrological fluxes such as river discharge can be simulated with relatively high accuracy either by calibrating the model with observations (Döll et al., 2003) and/or by employing lumped routing schemes to explicitly simulate shallow groundwater flows (Kim et al., 2009), these approaches do not guarantee the correct simulation of soil moisture (SM) and groundwater storage. Moreover, the uncertainties arising from these deficiencies in model parameterizations can be further amplified by the uncertainties in meteorological forcing datasets used to drive these models (Decharme & Douville, 2006).

Advances in satellite observations have enabled us to address some of the challenges in using hydrological models for large-scale hydrological studies (Pail et al., 2015). For example, the assimilation of terrestrial water storage (TWS) derived from the GRACE satellite mission into LSMs has been used to improve global simulation of TWS and its components by model calibration and assimilation techniques (Chen et al., 2017; Eicker et al., 2014; Girotto et al., 2016; Houborg et al., 2012; B. Li et al., 2012; B. Li & Rodell, 2015; Zaitchik et al., 2008) and to quantify the changes in certain variables that are not explicitly simulated by the models (e.g., groundwater storage) (Castellazzi et al., 2016; Famiglietti et al., 2011; Feng et al., 2013; S. Jin & Feng, 2013; Long et al., 2016; Nanteza et al., 2016; Rodell et al., 2009; Scanlon, Longuevergne, et al., 2012). GRACE data has also been extensively used to benchmark the accuracy of hydrological model simulations (Alkama et al., 2010; Decharme et al., 2010; Döll et al., 2014; Eicker et al., 2016; Freedman et al., 2014; Grippa et al., 2011; Landerer et al., 2010, 2013; Rosenberg et al., 2013; Swenson & Lawrence, 2015; H. Xie et al., 2012; Yang et al., 2011); conversely, LSMs have also proved useful to evaluate the performance of different GRACE products and processing methods

(Klees et al., 2008; Werth et al., 2009) and used as a priori information to restore signal attenuation and leakage errors arising from the low spatial resolution of GRACE (Landerer & Swenson, 2012; Long, Longuevergne, et al., 2015; Long, Yang, et al., 2015).

The GRACE and hydrological models complement each other to better constrain the different components on the water cycle; however, GRACE products are affected by various limitations and uncertainties. First, it provides a large-scale estimate of vertically integrated water storage variations, limiting safe interpretation to relatively large regions (>200,000 km^2) (Longuevergne et al., 2010). Second, GRACE products are affected by latitude-dependent uncertainties with higher uncertainties in mid and low latitudes compared to the poles (Wahr et al., 2006). Moreover, varying uncertainties can be found even among different GRACE solutions i.e., spherical harmonic (SH) products and mascons (Long et al., 2017; Scanlon et al., 2016; Watkins et al., 2015) which vary across different global regions.

GRACE measures the vertically integrated TWS variations caused by both natural and anthropogenic drivers. Therefore, hydrological models or other supplementary data are required to disintegrate the total TWS into separate components and to partition it into the natural and human-induced changes. For example, Human-induced TWS variations are estimated by computing the difference between GRACE that includes the human factors and hydrological models that simulate only the natural part of the water cycle (Huang et al., 2015; Y. Pan et al., 2016). Some other studies have used GRACE-based TWS variations and observed or simulated surface water storage variations to derive groundwater storage change in depleted aquifer systems where in some cases, the GRACE-detected TWS signature is mostly due to human-induced groundwater storage change (Famiglietti et al., 2011; Rodell et al., 2009; Scanlon, Longuevergne, et al., 2012) and in some cases it is due to specific climatic events such as climate variability or droughts (Russo & Lall, 2017; Scanlon et al., 2015). Although these approaches are useful for extracting human-induced TWS variations from models that do not account for human activities, they can involve significant uncertainties arising from the errors and uncertainties in two independent products (GRACE and models). The recent advancements in representing human activities in models (e.g., Pokhrel et al., 2016) provide the opportunity to directly isolate the human-induced TWS variations from models (e.g., Pokhrel et al., 2017) and compare the results with GRACE-based approaches.

Given the above background, we use multiple GRACE SH products and results from two hydrological models (one LSM and one GHM) to examine the spatio-temporal patterns of TWS variations and the uncertainties arising from the use of different GRACE products and hydrological models. To limit the propagation of some GRACE errors, we use the strategy to filter model output as GRACE before performing a comparison. Both models explicitly simulate the human-induced changes in TWS, including the changes in groundwater storage due to pumping, making the results directly comparable with GRACE. A detailed analysis is presented for the selected river basins located in different geographic regions and having different extent of human alterations in terms of flow regulation and groundwater use. Results from the simulation with natural settings (without considering human factors) are then used in conjunction with GRACE data to isolate the human-induced TWS variations from the total TWS change measured by GRACE. Our specific objectives are to: (1) examine the global spatial patterns in TWS variations over different river basins, especially by quantifying the contribution of different components to the total TWS variations; (2) carry out a temporal comparison among multiple GRACE SH products and two models and attribute the TWS variations to climate and human-induced factors in the basins where human land-water management has largely altered the terrestrial water balance; and (3) quantify the uncertainties in simulated TWS caused by the use of different sets of meteorological forcing data. These objectives provide the structural sub-headings used in the Methods, Results, and Discussion sections.

2.2. Models and Data

2.2.1. Models

We use two state-of-the-art hydrological models, namely the HiGW-MAT, an LSM (Pokhrel et al., 2015) and the PCR-GLOBWB, a GHM (Wada et al., 2014) to simulate the global terrestrial water fluxes and storages (excluding Antarctica and Greenland). Both models simulate the natural and human-induced changes in flows and storage of water, explicitly taking into account groundwater abstractions and the resulting changes in subsurface storage, which is crucial to realistically simulate the variations of TWS in regions with intensive groundwater mining. However, the two models use different groundwater representations; while PCR-GLOBWB simulates the groundwater storage as a linear reservoir model without explicitly representing water table dynamics, HiGW-MAT uses a more sophisticated groundwater scheme that explicitly simulates the water table dynamics. A detailed description of both models can be found in our earlier works (Pokhrel et al., 2015; Wada et al., 2014) but for completeness, we provide a brief summary of the models below.

The HiGW-MAT model is based on the Minimal Advanced Treatment of Surface Interactions and Runoff (MATSIRO) (Takata et al., 2003) LSM. In MATSIRO, effects of vegetation on the surface energy balance are calculated on the basis of the multi-layer canopy model of Watanabe (1994) and the photosynthesis-stomatal conductance model of Collatz et al.

(1991). The vertical movement of SM is estimated by numerically solving the Richards equation (Richards, 1931) for the soil layers in the unsaturated zone. Surface and subsurface runoff parameterizations are based on the simplified TOPMODEL (Beven & Kirkby, 1979; Stieglitz et al., 1997). In our recent studies, we enhanced MATSIRO by first representing HI schemes such as reservoir operation and irrigation (Pokhrel, Hanasaki, Koirala, et al., 2012; Pokhrel, Hanasaki, Yeh, et al., 2012) and then groundwater pumping (Pokhrel et al., 2015), resulting in the latest development called the HiGW-MAT.

In HiGW-MAT, irrigation is simulated by using a SM-deficit-based scheme described in Pokhrel et al. (2012). Gridded irrigated areas are based on the Pokhrel et al. (2012). The pumping scheme described in Pokhrel et al. (2015) explicitly simulates the amount of water withdrawn from aquifer and the associated changes in groundwater storage. The water table dynamics is simulated by using the scheme of Koirala et al. (2014). All soil and vegetation parameters and land cover data are prescribed based on the Global Soil Wetness Project 2 (GSWP2) (Dirmeyer et al., 2006). Subgrid variability of vegetation is represented by partitioning each grid cell into two tiles: natural vegetation and irrigated cropland. The crop growth module, based on the crop vegetation formulations and parameters of the Soil and Water Integrated Model (SWIM) (Krysanova et al., 1998), estimates the growing period necessary to obtain mature and optimal total plant biomass for 18 different crop types. The leaf area index (LAI) is resolved according to Hirabayashi et al. (2005). Surface runoff is routed through the river network using the Total Runoff Integrating Pathways (TRIP) (Oki & Sud, 1998). The reservoir operation is based on Hanasaki et al. (2006). Data for large and medium-sized reservoirs are same as in Pokhrel et al. (2012), which account for the majority of dams having a height of 15m or more.

The original MATSIRO and the HI schemes in HiGW-MAT have been extensively validated using observed river discharge, TWS, irrigation water withdrawals, groundwater pumping, and water table depth (Koirala et al., 2014; Pokhrel et al., 2015; Pokhrel, Hanasaki, Koirala, et al., 2012; Pokhrel, Hanasaki, Yeh, et al., 2012; F. Zhao et al., 2017). The results of evapotranspiration (ET) have not been validated due to the lack of reliable global ET products, but as in any typical global model, the underlying assumption is that since the models are forced by observed meteorological data and they perform reasonably well in reproducing river flow, ET simulations are also reasonable.

PCR-GLOBWB is an offline GHM that simulates the interaction of surface water and subsurface water through the atmosphere, land surface, two vertically stacked soil layers and an explicit underlying groundwater reservoir that is represented as a linear reservoir model (Kraijenhoff Van De Leur, 1958). PCR-GLOBWB explicitly simulates the water demands for agriculture, industry and households, and associated use from different water sources. The irrigation water requirement including the losses is calculated for paddy and nonpaddy crops based on the MIRCA2000 dataset (Portmann et al., 2010). The irrigation scheme is dynamically linked to the surface and subsurface hydrology schemes to provide a more realistic SM content and ET over irrigated croplands (Wada et al., 2014). Other water demands including livestock, industry and domestic are calculated based on various available socio-economic data and country statistics including livestock densities, GDP, electricity production, energy consumption, and population (Wada et al., 2014).

The vegetation and land cover are parameterized according to the Global Land Cover Characteristics Data Base version 2.0 (GLCC 2.0; https://lta.cr.usgs.gov/glcc/globdoc2_0#avhrr) and the Land Surface Parameter dataset (LSP2) (Hagemann, 2002). Soil properties are obtained from the vector-based FAO Digital Soil Map of the World (DSMW) (FAO, 2003) and the ISRIC-WISE global dataset of derived soil properties (Batjes, 2005). Using Simulated Topological Network (STN30) (Vörösmarty et al., 2000), surface and subsurface runoff are routed along the river network. The Global Reservoir and Dam database (GRanD) (Lehner et al., 2011) is used to locate the reservoirs on the river network based on the construction year. Reservoir regulation and release is simulated based on Hanasaki et al. (2006) and van Beek et al. (2011) to satisfy downstream water demands (Wada et al., 2010, 2014). The PCR-GLOBWB model is also validated with the observations of river discharge and runoff, TWS, irrigation water requirement, and groundwater withdrawal (van Beek et al., 2011; Wada et al., 2014).

2.2.2. Climate Forcing

We use forcing data from multiple sources. HiGW-MAT is driven by three forcing datasets: (1) the WFDEI (WATCH Forcing Data methodology applied to ERA-Interim reanalysis data) (Weedon et al., 2014), (2) the forcing data from Princeton University (Sheffield et al., 2006), and (3) the JRA-25 atmospheric reanalysis data provided by Japanese Meteorological Agency (JMA) Climate Data Assimilation System (JCDAS) (Kim et al., 2009; Onogi et al., 2007). The results from the third forcing data, which are validated in our previous studies, are used for the analysis of TWS, and the other two datasets are used to examine the uncertainty arising from the climate forcing data (see Section 2.3.3). PCR-GLOBWB is forced only by WFDEI data and is not considered for uncertainty analysis.

2.2.3. GRACE Data

The GRACE data along with model results are used to analyze the TWS variations. We use different level-3 SH-based GRACE products of equivalent water height (EWH) from three processing centers, namely: (i) the Center for Space Research (CSR) at University of Texas at Austin, (ii) Jet Propulsion Laboratory (JPL) at California Institute of Technology, and (iii) the German Research Center for Geoscience (GFZ) (available for download from JPL website; http://grace.jpl.nasa.gov/data/get-data/) for model evaluation and to characterize the uncertainty within the three GRACE products. In general, while the three official products (CSR, JPL, and GFZ) underestimate GRACE uncertainties (Sakumura et al., 2014), they provide a fair estimate to evaluate hydrological models. The GRACE satellite level 2 data processing delivers the dimensionless Stokes' coefficients (C_{lm} and S_{lm}) complete to degree and order 96 ($l = m = 96$). Corrections and adjustments are needed to reduce noises and isolate the TWS changes from other signals visible in GRACE. The GRACE data from aforementioned sources already carry corrections and filtering including atmospheric mass changes removal, glacial isostatic adjustment (GIA), truncation of SH coefficients at degree 60, and application of destriping filter alongside with a 300-km Gaussian smoother.

It is important to consider observational errors when using GRACE data to evaluate models. The GRACE error budget can be separated into three types (Longuevergne et al., 2010): (1) errors associated with fundamental GRACE measurements satellite to satellite range rate (~5 mm EWH at the scale of GRACE resolution limit, ~400 km), (2) errors in atmospheric and oceanic corrections (~10 to 20 mm EWH at ~400 km scale) and (3) bias and leakage correction errors which can be the largest depending on basin area and context (~30 mm EWH for a 200,000 km^2 basin). In this work, rescaling factors are not used, and the model results are filtered as GRACE to compare at an equivalent resolution and avoid type (3) errors. This method has been highlighted as a robust approach for model evaluation (Güntner, 2008; H. Xie et al., 2012).

2.3. Methods

2.3.1. Spatial Patterns in TWS Variations and Contribution of Different Components

We use the results from the fully coupled versions of both models (i.e., by activating all human impacts schemes) to evaluate the model performance in capturing the spatial variability in TWS rates measured by GRACE. For consistent comparison with GRACE data, the spatial map of simulated TWS rates from both models is transformed into SH domain, truncated at degree and order 60, and smoothed by the 300-km Gaussian filter, following Wahr et al. (1998). The spatial filtering process reduces the errors and noises as well as the true signals. The use of same filtering processes for model outputs, as used for GRACE products, offsets the necessity to reconstruct the attenuated signals when directly comparing GRACE-based and simulated TWS (Landerer & Swenson, 2012).

Additionally, understanding how different storage compartments (i.e., snow and ice, soil water, river water, and groundwater) contribute to the variations of total TWS is crucial to investigate how the changes in these individual compartments can potentially affect the availability and utilization of water resources. Isolation of the individual components also provides key insights on the interactions and feedback among different components under changing hydrologic regime. Here, we use a dimensionless metric called the component contribution ratio (CCR) proposed by Kim et al. (2009) to determine the role of different TWS components in modulating the total TWS variations in river basins from different climate regions. The ratio is calculated as:

$$CCR = \frac{MAD}{TV} \tag{2-1}$$

where MAD is the mean absolute deviation of a TWS component ($\frac{1}{N}\sum_{t}^{N}|S_t - \bar{S}|, S_t$ is the value of component S at time t and N is the number of months), TV is the total variability and is calculated as summation of all components MADs ($\sum_{i=S}^{components} MAD_i$). The CCR values are calculated by using HiGW-MAT model results.

2.3.2. Temporal Variability of TWS in Global Basins: Human-induced TWS Change

We make an integrated use of GRACE data and models to examine the temporal variability of TWS over the selected global river basins and isolate the human-induced TWS change. To estimate basin-scale water storage, a simple basin function (which has the value 1 for inside the basin and 0 outside) is used. The function is then multiplied by different model and GRACE signals to form the basin scale water storage. Since the data are in 1-degree resolution with varying grid cell area, an area-weighted arithmetic mean is finally calculated as:

$$H(x,t) = \frac{\sum_{i=1}^{n} S_i(x,t)}{A}, \quad S_i(x) = \begin{cases} 1 \times s \times a_i & \textit{inside the basin} \\ 0 & \textit{outside the basin} \end{cases} \tag{2-2}$$

where s is the LSM or GRACE estimate, a_i is the cell area, S_i is the weighted estimate for each cell inside the basin, n is the number of cells in a basin, A is the total area of the basin, and $H(x,t)$ represents the estimate of water storage for basin at time t.

We quantify the human-induced TWS change using GRACE and hydrological models in some of the basins affected by human activities. First, we estimate the long-term linear trend in TWS from GRACE observations, PCR-GLOBWB, and HiGW-MAT (simulations with HI). Then, we estimate the similar trend using the model results from the simulation with natural setting in which all HI schemes are deactivated. We then calculate the difference between the two trends as an estimate of the direct human-induced changes in TWS. To estimate the variations in monthly TWS from model results, we use two different approaches. First, for simulations with HI, we directly integrate the individual TWS components (i.e., snow water, canopy water, river water, SM, and groundwater). Due to explicit representations of human activities in both HiGW-MAT and PCR-GLOBWB, all TWS components are explicitly simulated, also taking into account the impacts of human activities. In this approach, the vertically integrated TWS is expressed as:

$$TWS = SW + SnW + SM + GW + CW \tag{2-3}$$

where, SW, SnW, SM, GW, and CW denote surface water, snow water, SM, groundwater, and canopy water storages (all terms have the dimension [L]), respectively. The changes in storage terms (Equation 2-3) include groundwater storage and water table changes due to pumping; changes in surface water reservoirs, and changes in SM due to human water management (e.g., irrigation).

Second, for the simulation with natural setting, we use the water balance approach (Famiglietti et al., 2011; Nanteza et al., 2016; Rodell et al., 2004; Syed et al., 2008; N. Zeng et al., 2008) in which the TWS change is deduced from monthly precipitation, evapotranspiration, and runoff as:

$$\frac{dTWS}{dt} = P - ET - R \tag{2-4}$$

where, P is the observed precipitation, ET is the simulated actual evapotranspiration, and R is the simulated runoff (all terms have the dimension [LT^{-1}]). Equation 2-4 can be used over large river basins and long-term simulation period with the assumption of no lateral groundwater fluxes in the boundaries (Long et al., 2017). However, we use the water balance method only for the simulation with natural setting (and not for HI simulations) due to high uncertainties in flux variables, particularly in ET and R (Long et al., 2014, 2017; Wang, Pan, et al., 2015) that are strongly influenced by HI such as irrigation, surface water flow regulation, and groundwater storage change due to pumping. While we use Equation 2-3 to derive the TWS from model simulations with all HI schemes activated which is used for model evaluation with GRACE, the TWS estimated by using Equation 2-4 (based on HiGW-MAT model) is combined with GRACE data to isolate the human-induced TWS variations in the highly-managed river basins.

To better investigate the performance of models in TWS simulations, we decompose the observation data and simulated time series into general trend and seasonality using moving averages and applying convolution filter. In the decomposition progress, the data ($Y[t]$) is disaggregated into general trend ($T[t]$), seasonality ($S[t]$), and residuals ($e[t]$) to form the additive model: $Y(t) = T(t) + S(t) + e(t)$.

2.3.3. The Uncertainty from Climate Forcing Data

We examine the uncertainty in the simulated TWS by using different forcing datasets listed in Section 2.2.2. For this purpose, we use only the HiGW-MAT model which is driven by the three forcing datasets. Among the three datasets, we use the data from Kim et al. (2009) to derive the TWS used for the spatio-temporal analysis, including the comparison with the results from PCR-GLOBWB model which is driven by the WFDEI data, and the estimation of CCR because the same data has been used in our previous model validation studies (Pokhrel et al., 2015; Pokhrel, Hanasaki, Koirala, et al., 2012; Pokhrel, Hanasaki, Yeh, et al., 2012). The other two datasets are then used to examine the uncertainties in simulated TWS that are caused by the use of different forcing data. We did so to ensure that the HiGW-MAT simulations used to derive the key conclusion are well-validated before.

The results from the uncertainty analysis are derived from filtered simulations and are not directly compared with GRACE. Therefore, it is necessary to account for the true signal losses (caused by filtering and smoothing) by rescaling the simulations. Here, we use the scaling factor approach (Landerer and Swenson, 2012; Long et al., 2015a, 2015b) which estimates the scaling factors, also referred as multiplicative factors, from the least squares fit (Equation 2-5) between the gridded filtered and unfiltered TWS changes from the model (see Landerer and Swenson, 2012 and Long et al., 2015a for details) as:

$$M = \sum_{T} (S_t - kS_f)^2 \tag{2-5}$$

where, M is the objective function to be minimized, S_t is the true signal (model output), S_f is the filtered signal, T is the time steps (here, months in 2002-2008), and k is the scaling factor.

2.4. Results

2.4.1. Spatial Patterns in TWS Variations and Contribution of Different Components

We first evaluate the spatial variability of the long-term trend in total TWS variations simulated by the two models with GRACE (the mean of CSR, JPL, and GFZ) TWS trend (Figure 2-1). Due to high susceptibility of the linear trend to the selection of time window, we use the 2002-2008 period that represents high diversity in signal patterns with relatively distinct spatial variations in positive and negative trends among natural and human-affected global regions, especially the downward TWS trends due to groundwater depletion. Overall, a good agreement can be seen between GRACE (Figure 2-1a), and both HiGW-MAT (Figure 2-1b), and PCR-GLOBWB (Figure 2-1c) models in terms of the direction of change; however, significant discrepancies are also apparent in terms of the magnitude. For example, the global hotspots of groundwater depletion such as the northwestern India and parts of Pakistan, the North China Plain, and parts of Middle East (where the changes in total TWS are known to be dominated by groundwater storage change) are detected in both GRACE and models but the magnitude of changes varies largely among the three estimates. In northwest India, clear differences can be seen; while GRACE data suggest a small downward trend, HiGW-MAT suggests a much larger TWS depletion and PCR-GLOBWB shows little change. In the California's Central Valley Aquifer (CVA), HiGW-MAT simulates a larger decrease in TWS compared to the other two estimates, which is likely due to overestimation of groundwater pumping as suggested by Pokhrel et al. (2015). The performance of PCR-GLOBWB is generally good in many of these regions that are affected by human activities, but it doesn't reproduce the GRACE-detected negative trends in parts of southeastern Australia and northeastern China.

In some of the regions with relatively low human influence such as the Amazon, Orinoco, and Parana River basins in South America and southern parts of Africa, significant variations are obvious among the models and GRACE both in the sign and magnitude. In the Amazon and Orinoco, the HiGW-MAT model captures the GRACE trend reasonably well while the PCR-GLOBWB shows a larger deviation. On the contrary, in the southern parts of Africa HiGW-MAT simulates a large positive trend while PCR-GLOBWB simulates a milder trend, consistent with GRACE. In the river basins in the northern high latitude such as the Yukon, GRACE detects a large negative TWS trend during 2002-2008 which has been suggested to be due to glacier melts, permafrost thaw, and snow cover shrinkage (Ge et al., 2013; Spence, 2002; St. Jacques & Sauchyn, 2009; Wang, Huang, et al., 2015), processes that are not explicitly simulated by both models.

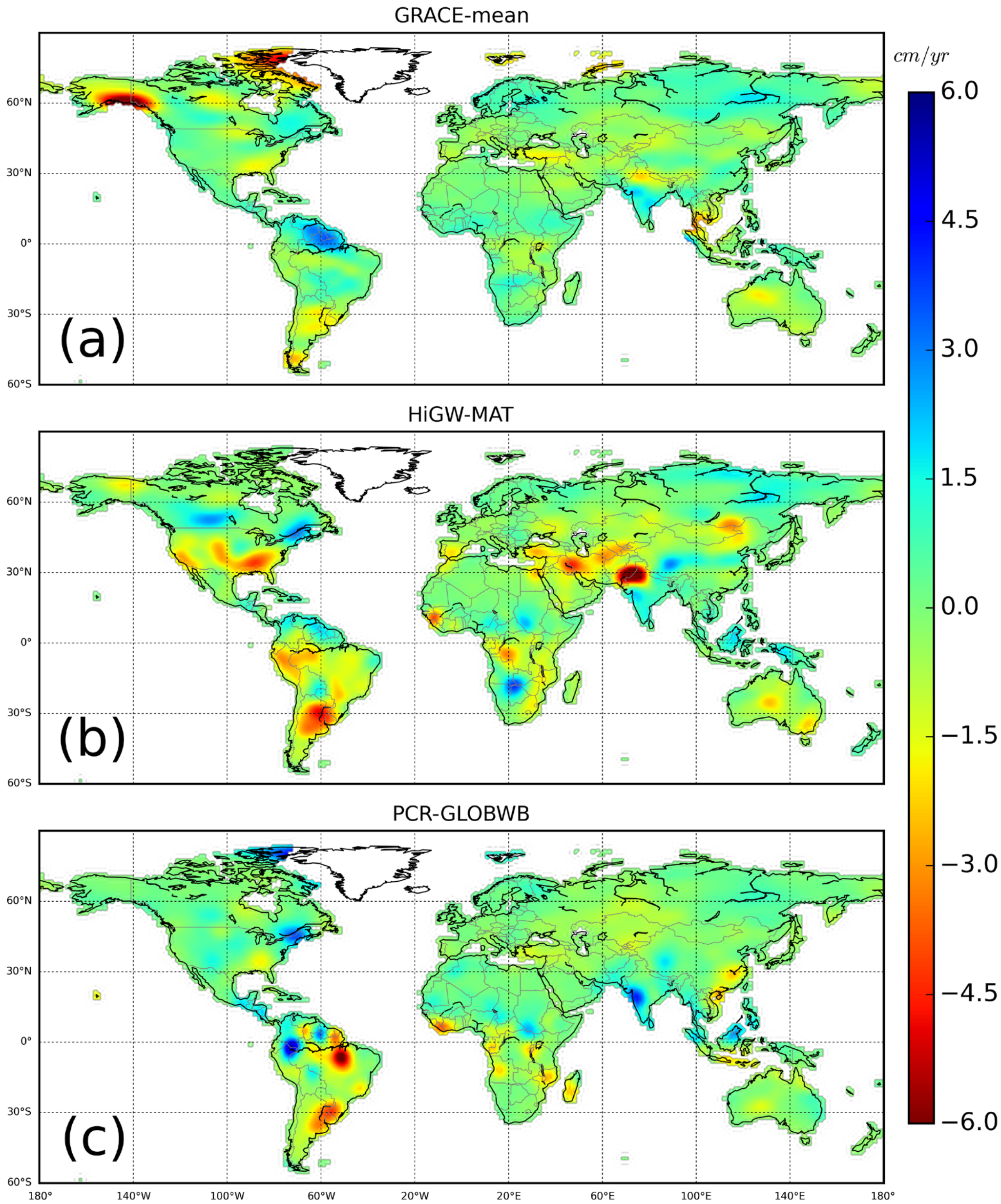

Figure 2-1. Spatial pattern of TWS trend from GRACE, and the two models (HiGW-MAT and PCR-GLOBWB) for 2002-2008. GRACE results are shown as the mean of the solutions from three different processing centers (i.e., CSR, JPL, and GFZ).

The contribution of the individual storage components to total TWS is quantified for 30 river basins. The river basins are selected considering: (a) a wide coverage over different climatic regions and continents, and (b) a good balance between natural and human-affected regions. Figure

2-2 depicts the river basins along with the CCR calculated by using HiGW-MAT model results. The size of the circles is proportional to the seasonal amplitude of the total TWS variation, with the largest amplitude being 500 mm in the Orinoco River basin. Both models used in the study do not explicitly simulate glacier processes, so the surface water component includes only snow and river water. As expected, in the northern high latitudes and polar regions snow storage component dominates the TWS. The highest contribution of snow is found in the Yenisey (61%), Mackenzie (60%), Yukon (59%), Lena (54%), and OB (54%) river basins. Moving toward the mid-latitudes and the subtropical area, high snow storage is substituted by surface and subsurface storages. The highest contribution of surface water storage can be seen in the Yangtze (33%), Brahmaputra (28%), and Ganges (20%), all located in the subtropics and managed by large number of reservoirs (Lehner et al., 2011). Subsurface water storage dominatingly modulates the total TWS variations in the temperate and tropical regions such as the Niger (97%), Parana (90%), Tocantins (90%), and Congo (89%) river basins, and also in river basins with semi-arid climates such as the Murray–Darling (95%) and Euphrates (88%) basins. The contribution of subsurface water storage is also found to be large in the river basins with strong human influence, particularly in regions where excessive groundwater is used for irrigation (e.g., the Indus, Huang-He, Euphrates, and Murray-Darling basins).

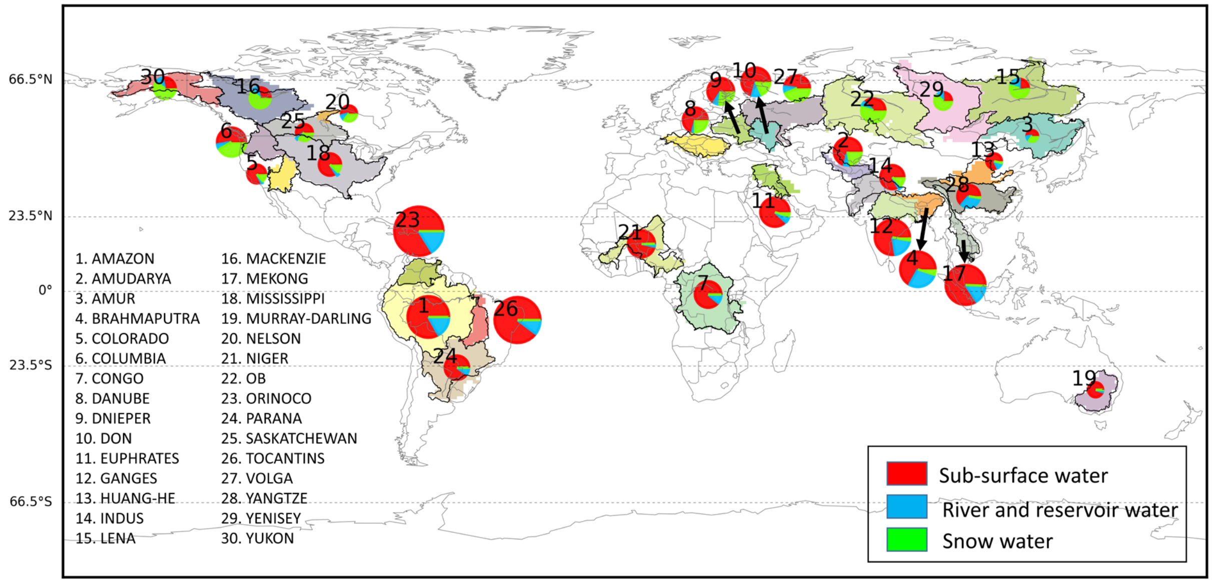

Figure 2-2. Map showing the selected 30 river basins with the component contribution ratio (CCR) for snow water, surface water (rivers and reservoirs), and subsurface water (SM and groundwater) storages, shown as pie charts for each of the basins. The CCR values are calculated by using HiGW-MAT model results. The size of pie chart is proportional to the seasonal amplitude of TWS variation, with the largest amplitude being 500 mm in the Orinoco river basin.

2.4.2. Temporal Variability of TWS in Global Basins: Human-induced TWS Change

Figure 2-3 presents the seasonal cycle of TWS variations from GRACE, HiGW-MAT, and PCR-GLOBWB for the selected basins. We present the range of variations among the three SH solutions (CSR, JPL, and GFZ) as the gray-shaded band. In this figure, the basins have been classified into three categories, namely the natural, managed, and snow-dominated which are shown with white, yellow, and light-blue background, respectively. Similar to the spatial patterns of the long-term trend (Figure 2-1), a generally good agreement can be seen between GRACE products and models, especially in the basins with less human influence and snow contribution (white background). In some of the managed and snow-dominated basins such as the Huang-He

(Yellow River), Amur, Murray-Darling, and Yukon the GRACE-model agreement is generally poor for both models. In the basins such as the Huang-He, Indus, Amur, Lena, Mackenzie, and Yukon notable difference between the two models are also obvious both in terms of the seasonal amplitude and timing of peak.

Also shown in Figure 2-3 are the individual TWS components (i.e., snow, river, soil, and groundwater storages) to scrutinize how different storage compartments modulate the total TWS signal in different geographic and climatic regions. For clarity of view we present these details only from the HiGW-MAT model. In many of the selected basins where the contribution of snow is relatively small, the seasonal TWS signal is strongly modulated by the variations in subsurface storage, which is governed by the inverse relationship between SM and groundwater. These two components compete for the same storage space and thus evolve over time in opposite phase (Duffy, 1996; Pokhrel et al., 2013). Note that in HiGW-MAT, the SM and groundwater are estimated as water stored above and below the water table depth, respectively, which is different than in typical global LSMs and GHMs that consider SM to be the water stored within the fixed soil depth (typically top 1-2m) resulting in the same-phase relationship between SM and groundwater storages, but with certain time lag. The dominance of surface water can be seen in basins such as the Ganges, Brahmaputra, and Mekong where the seasonal flood pulse transports large volume of water during the monsoon season. In snow-dominated basins such as the Mackenzie, Yenisey, and Yukon a strong seasonal signal of snow accumulation can be seen during the boreal spring which is followed by an increase in river water arising from snowmelt.

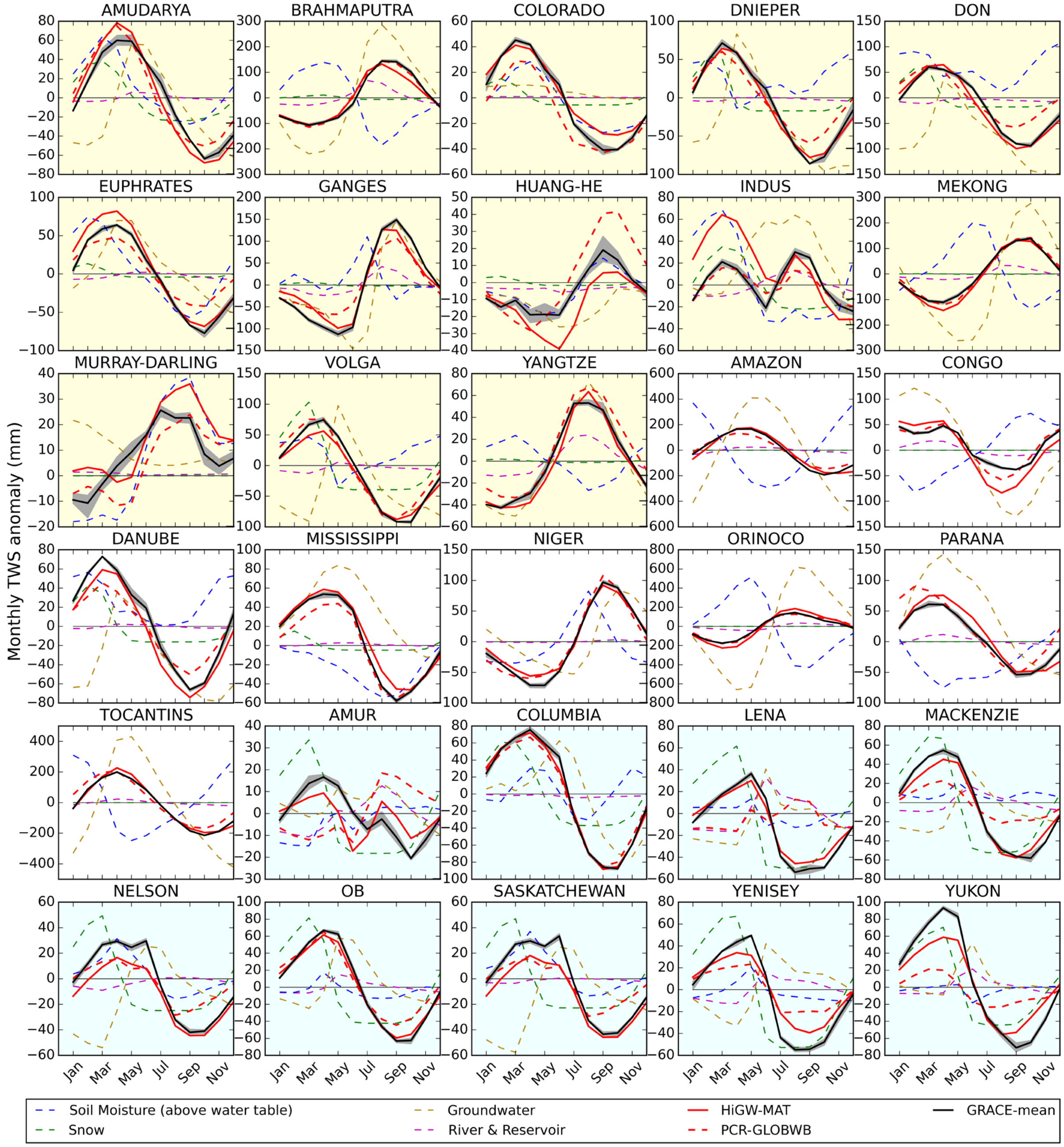

Figure 2-3. Seasonal cycle of simulated and observed TWS and components for the selected river basins. Yellow background indicates the region with human impacts and light blue background represents snow-dominated basin. Basins with relatively less human influence and contribution from snow are shown with white background. The thick black line represents the mean of three GRACE products from CSR, JPL, and GFZ and the gray-shaded band shows the range of variations among the three GRACE products. While the simulated total TWS from both

Figure 2-3 (cont'd) models are shown, the individual components (i.e., snow, river and reservoir, SM, and groundwater storages) are shown only from the HiGW-MAT model for clarity of view.

In Figure 2-4, we provide further details on the inter-annual variability of TWS from different GRACE solutions (shown as shaded range) and both models along with the individual components from HiGW-MAT. All results are shown as anomalies relative to the 2004-2009 time-mean baseline to be consistent with GRACE. The simulated TWS from both expansions (Equation 2-3 and Equation 2-4) is truncated at degree and order 60 and smoothed by the 300-km Gaussian filter in all figures corresponding to GRACE products. In Figure 2-4, the slopes of the trend lines from GRACE, models (with activated HI modules), and the water balance analysis (i.e., the simulation without human activities) are shown at the bottom of each panel. The p-value approach is used to measure the statistical significance of linear trends from GRACE and model outputs, i.e., to determine the probability of whether the simulated trends are non-zero and that is statistically significant (Zhou et al., 2014). Results indicate that the TWS trend in natural simulation, which is mostly close to zero, is not statistically significant (p values > 0.05) in most of the managed basins. Further, the p values indicate that the PCR-GLOBWB trend for Euphrates, Indus, Murray-Darling, and Volga basins, the GRACE trend for Brahmaputra, Euphrates, Ganges, Indus, and Volga basins, and the HiGW-MAT trend for most of the managed basins are statistically significant (p values < 0.05).

For most of the managed river basins (except for the Colorado and Murray-Darling), the long-term negative trend in the total TWS is larger in GRACE solutions than in the results from water balance, suggesting that these basins experienced certain loss of water during the analysis period. The PCR-GLOBWB model mostly follows the GRACE trends in most river basins but the HiGW-MAT model suggests a substantially larger negative trend in TWS in the managed basins that is primarily due to the decline in groundwater storage (noticeable in the Indus and Huang-He basins). This also implies that the pumping scheme in HiGW-MAT may have overestimated groundwater pumping as discussed earlier in Figure 2-1. Colorado and Murray-Darling, show unexpected increase in GRACE TWS that represents smaller deficit rate than in the natural simulation. The positive trend in GRACE data in these basins is primarily due to some wet cycles (e.g., year 2005 and year 2010) in their long-term inter-annual variability of TWS. For instance, the precipitation increases in the wet year of 2010 in Murray-Darling basin and also the snow amount change that is followed by two wet cycles around the years 2005 and 2010 in the Colorado basin resulted in such positive overall trends during 2002-2010. As such, if the wet cycles of 2005 and 2010 are excluded from the analysis, Murray-Darling and Colorado basins also show a significant TWS loss.

The largest difference between GRACE and natural trends can be seen in the Euphrates, a transboundary river basin between Iraq, Turkey, Jordan, and Saudi Arabia. While GRACE TWS regression line drops at rate of 2.13 cm year^{-1}, only 0.06 cm year^{-1} of that is caused by natural variability, and the rest (2.07 cm year^{-1}) is caused by direct HI. The Ganges River basin with the second largest divergence between the natural and GRACE trend lines also experiences a 1.99 cm year^{-1} human-induced TWS loss. For this basin, HiGW-MAT performs well especially in simulating the drought years (negative peaks). In the Indus, despite a relatively constant and positive precipitation trend as well as a small negative P-ET-R trend (0.01 cm year^{-1} of water storage loss), GRACE shows a larger drop in TWS that is 0.82 cm year^{-1}. Clearly, this huge difference is due to the widely reported depletion of groundwater resources in part of the basin (Rodell et al., 2009; Tiwari et al., 2009). For river basins with considerable snow water component (distinguished by light blue background color), HiGW-MAT performs better. In particular, HiGW-

MAT shows the seasonal variations consistent with GRACE (Figure 2-3 and Figure 2-4) likely due to advanced energy balance scheme. In other basins that represent low human influence and small contribution from snow (e.g., Amazon, Danube, and Niger), both models simulate TWS variability and seasonal cycle well.

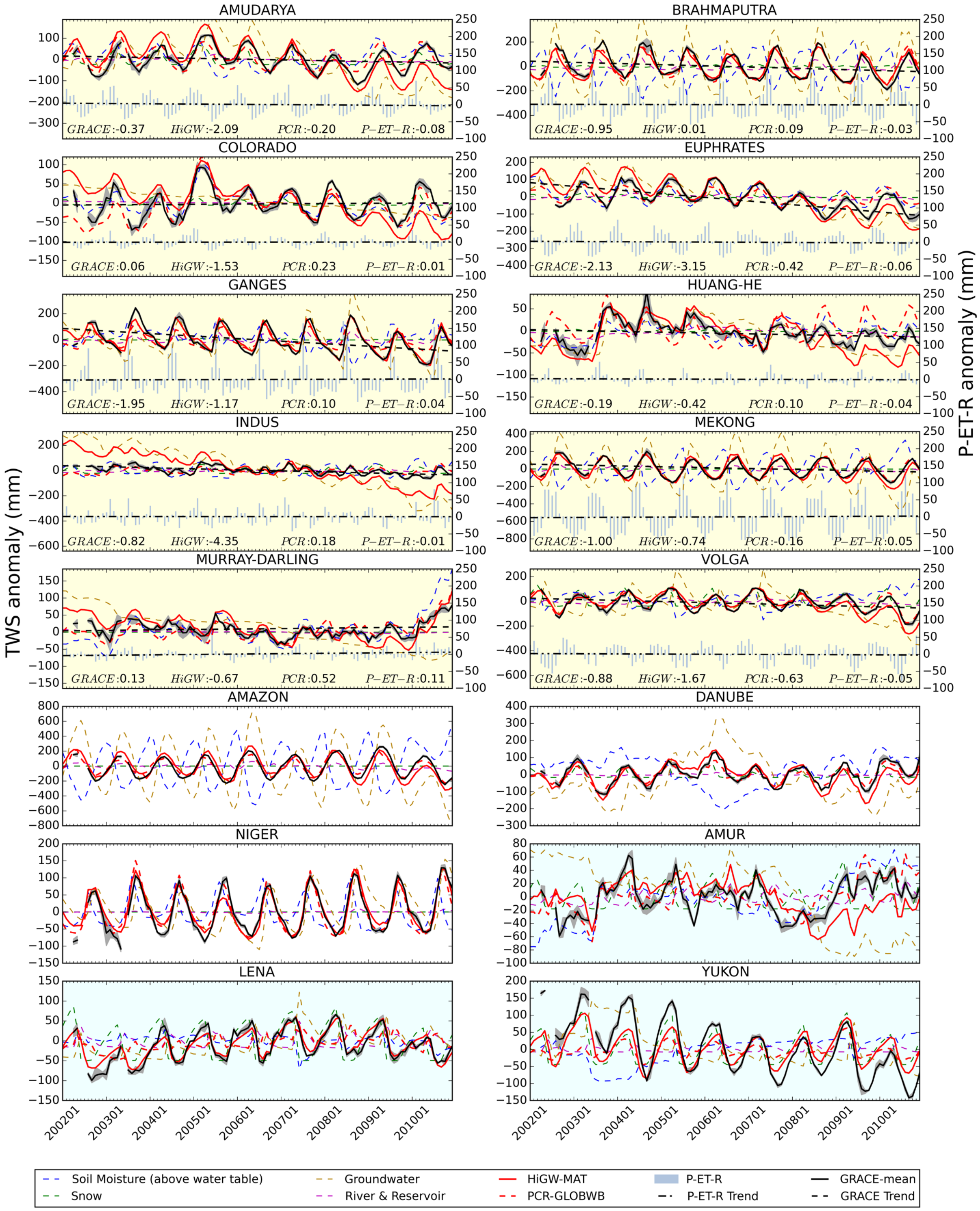

Figure 2-4. Inter-annual variability in TWS from GRACE and the two models. Background colors represent the same as in Figure 3. For the managed basins (top five rows with yellow background), the GRACE data and model results are plotted as line diagram on the top and the

Figure 2-4 (cont'd) results from the water balance analysis using the natural simulations (Equation 2-4) are shown on the bottom as bars. The gray-shaded range represents the range of variations of the GRACE products (CSR, JPL, and GFZ) along with the thick black line that shows the mean. The individual water storage components are shown only from the HiGW-MAT model for clarity of view.

To provide further insights, we present a decomposition of the TWS signal into the general trend and seasonality for two selected river basins, namely the Indus (managed) and the Lena (snow-dominated). As shown in Figure 2-5, for the Indus while the PCR-GLOBWB simulates both the trend and seasonality in line with GRACE, HiGW-MAT doesn't capture the long-term trend despite simulating the seasonality relatively well. This further confirms that the issue in HiGW-MAT could be the overestimation of groundwater pumping that results in a larger depletion rate even though the model simulates the seasonal dynamics of the various land surface hydrologic processes as well as water table dynamics. The results for the Lena are contrasting. Here, both models capture the general trend rather accurately but the PCR-GLOBWB fails to simulate the seasonality and timing of TWS anomaly. Analysis of the results for other basins such as the Amudarya, Colorado, and Euphrates (not shown) suggests that the performance of HiGW-MAT in these basins is similar to that in the Indus but it performs relatively well in the Brahmaputra, Ganges, and Volga basins. The performance of PCR-GLOBWB in most of the other snow-dominated basins is similar to that in the Lena.

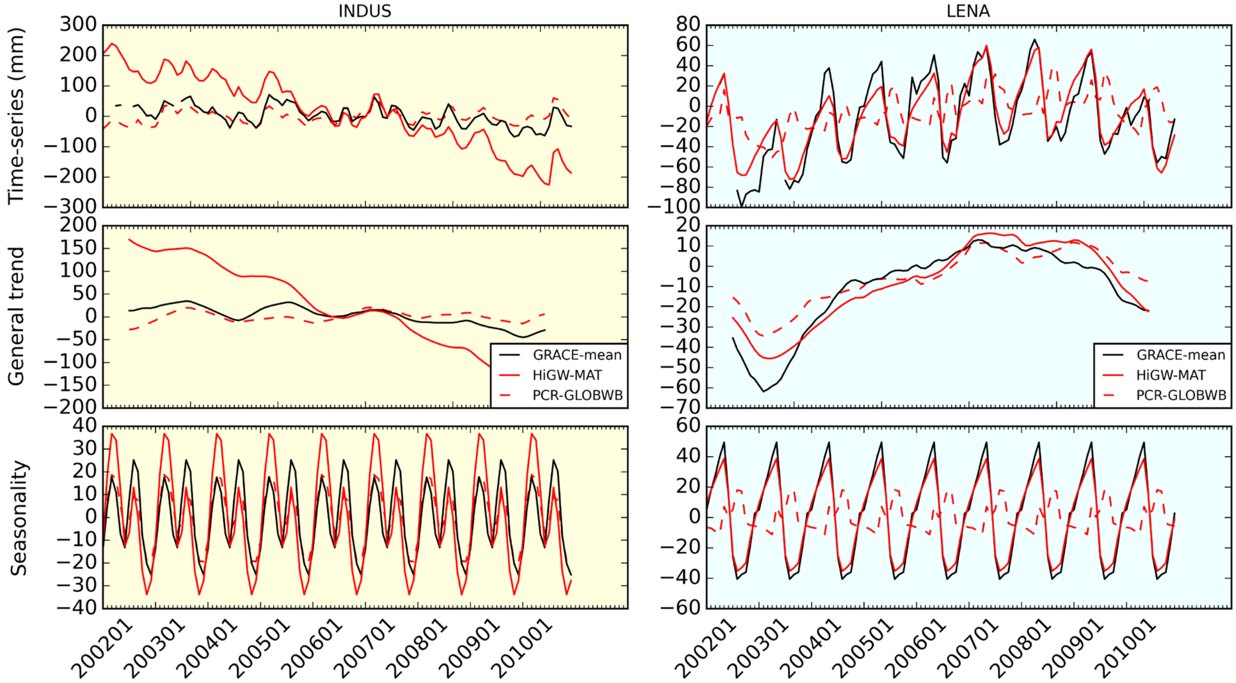

Figure 2-5. Decomposition of TWS time series into the general trend and seasonality for the Lena (snow-dominated) and Indus (managed) river basins.

2.4.3. The Uncertainty Arising from the Climate Forcing Data

The standard deviation of 2002-2008 trend map from three climate forcing datasets illustrates high uncertainty in the order of 10 cm year^{-1} (Figure 2-6a), highlighting the significant impact of forcing data selection in model results. Since the results presented here are based on the filtered products that we used for comparison with GRACE, it is necessary to consider the multiplicative factors (Equation 2-5) to restore the original signals. As seen in Figure 2-6b, the scaling factors are in the order of 1-3 for some regions which means that the trends in Figure 2-6a could be 1-3 times larger. The spatial pattern of standard deviation in TWS trend using three different forcing datasets (Figure 2-6) in comparison with the discrepancies between the spatial pattern of TWS trend from GRACE and HiGW-MAT (Figure 2-1a vs Figure 2-1b) notes that the discrepancies between model results and GRACE could partly be contributed by high uncertainties arising from forcing datasets. Furthermore, high standard deviation is particularly obvious over the human affected areas comprising northwest of India, northeastern China, southern Australia, Argentina, central U.S., and west regions of the Caspian Sea. This is reasonable because the forcing datasets are based on reanalysis (e.g., Onogi et al., 2007), which are produced by assimilating the available observations with the results from atmospheric models that typically do not account for human activities. That is, the forcing datasets, particularly precipitation, may have relatively larger biases in the highly managed regions.

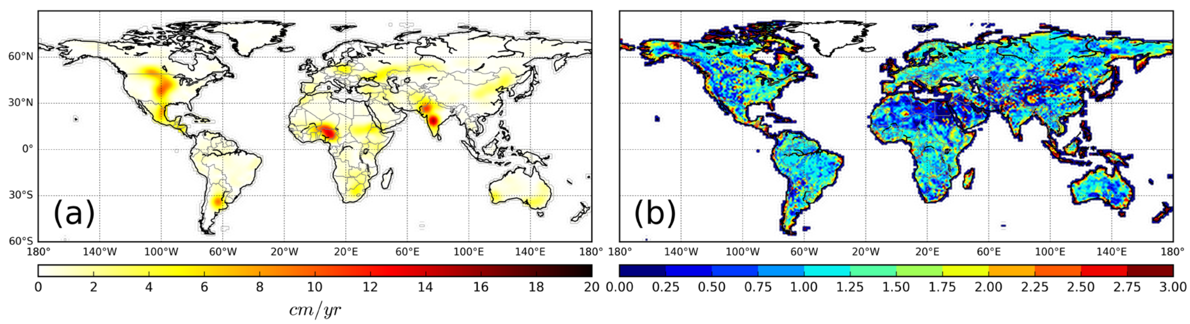

Figure 2-6. Standard deviation of TWS trend for 2002-2008 based on the results from HiGW-MAT model simulated by using three different forcing datasets (a), and the spatial distribution of scaling factors derived from the HiGW-MAT model (b). Since the TWS trend is calculated from filtered products that we used for comparison with GRACE, it is necessary to consider the scaling factors (when model results are not directly comparing with GRACE) to restore the original signals.

2.5. Discussion

2.5.1. Spatial Patterns in TWS Variations and Contribution of Different Components

The spatial patterns of the long-term trend in total TWS from models show a generally good agreement with GRACE in capturing the direction of change; however, significant differences are found in the magnitude of TWS signal between the two models and GRACE as well as between the two models. These differences are highly pronounced especially in the global hotspots of groundwater overexploitation identified by various previous studies. This is found to be caused partly by the overestimation of groundwater abstraction and the associated change in subsurface storage in the HiGW-MAT model. In other regions, such as the northern high latitudes where the TWS variations are largely modulated by snow water storage, the HiGW-MAT model generally captures the GRACE-based TWS trend but the PCR-GLOBWB model shows a larger deviation from the GRACE trend. The differences between GRACE and models in the high latitudes is likely due to glacier melts, permafrost thaw, and snow cover shrinkage processes that are not explicitly represented in the models as in any other current-generation LSMs and GHMs (Chen et al., 2017; Long et al., 2017). In most of the regions with relatively less human influence and snow contribution (e.g., parts of Europe, western Australia, central Asia and northern Africa) both models perform relatively well, suggesting higher reliability of model results in these areas.

These analyses contribute to the discussion on how the two models that include HI representations regenerate the spatial patterns of the long-term trend in TWS observed by GRACE. Our results corroborate the findings of previous studies that have reported certain discrepancies between GRACE and models in some of the river basins studied here by using other GHMs and LSMs such as the CLM (Swenson & Lawrence, 2015), WaterGAP model (Döll et al., 2014), and GLDAS (S. Jin & Feng, 2013) models. Together, these findings suggest that a single model cannot be identified as the best model over all global regions, implying that an ensemble model mean could provide a better estimate of TWS variations.

2.5.2. Temporal Variability of TWS in Global Basins: Human-induced TWS Change

An in-depth analysis of the seasonal cycle of TWS variations further suggests that the PCR-GLOBWB tends to perform better in some of the managed basins (e.g., the Indus), in line with studies such as Wada et al. (2014). However, it is found that both models do not accurately capture the seasonal dynamics of TWS in some of these managed basins such as the Huang-He and Murray-Darling. It is also evident from the results that while one model captures the amplitude of the positive seasonal anomaly accurately, it fails to reproduce the negative seasonal anomaly with similar accuracy, and this applies to both models (see Huang-He, Indus, Murray-Darling basins). This implies that while certain human water management practices such as reservoir operation may have been well simulated, the model may have failed to accurately simulate other processes such as groundwater dynamics that can act as a buffer during high and low flow seasons. It is also important to note that there are differences among the GRACE products in some of these basins making it difficult to evaluate the model performance with high confidence. In the snow-dominated basins (e.g., the Lena, Amur, Mackenzie, and Yukon), the performance of HiGW-MAT is relatively good likely due to its relatively robust and physically-based snow melt scheme which is based on multi-layer snow energy balance (Takata et al., 2003).

The partitioning of inter-annual TWS changes into natural and human components in the highly-managed basins such as the Indus, Amudarya, Ganges, Brahmaputra, Euphrates, and Volga suggests a large deviation in the natural trend from the trend in GRACE data, indicating an expansion of human influence in these basins during 2002-2010. It is worth noting that the rates of TWS change from HI simulations are remarkably different from GRACE observations in many basins, which highlights the uncertainties in simulated trends. The groundwater extraction scheme in HiGW-MAT tends to consistently overestimate groundwater withdrawals in some of the human affected basins such as Amudarya, Colorado, Euphrates, Huang-He, and Indus, causing larger TWS decline compared with both GRACE and the PCR-GLOBWB model. However, in other basins such as the Brahmaputra, Ganges, Mekong, and Volga, which also include some managed agricultural regions, no such overestimation of groundwater depletion is found. The varying performance of HiGW-MAT in the managed basins is likely owing to the use of inaccurate parameters such as the specific yield or overestimation of agricultural demands caused by overestimated irrigated areas (Giordano, 2009; Pokhrel et al., 2015). Similar to the results for the spatial variability, the PCR-GLOBWB performs relatively better in the managed basins but simulates large deviations from both GRACE and HiGW-MAT in the snow-dominated basins such as the Amur, Lena, and Yukon.

Further, the analysis of the general trend and seasonal variability in the Indus and Lena river basins shows that while one model captures the general trend in one basin the other model performs better in capturing the seasonal variability. These large differences in capturing different aspects of the TWS variations in river basins located in different regions again suggest that a single model cannot be used with high reliability in all global regions or to simulate all aspects of TWS variations.

2.5.3. The Uncertainty Arising from the Climate Forcing Data

Results from the HiGW-MAT TWS simulations with three different meteorological forcing datasets reveal that, in some regions, the uncertainties in TWS trends due to the uncertainty in forcing datasets are as high as the differences among different models, or among different models and GRACE data. The forcing uncertainties are particularly pronounced in the highly managed regions, possibly due to the large uncertainties in the reanalysis products in which results from models without HI are assimilated. Additionally, the uncertainties could be even larger in some regions considering the spatial distribution of scaling factors derived from the HiGW-MAT model (in line with gridded scaling factors obtained from other studies e.g., Landerer and Swenson, 2012; Long et al., 2015a that used other LSMs). Such large uncertainties arising from forcing datasets suggest that the model results of TWS based on one particular forcing data need to be interpreted with enough caution, which is especially important when using the model results to evaluate the disagreements among different GRACE solutions and the performance of various filtering and other post-processing techniques applied to GRACE solutions.

2.6. Conclusions

This study quantifies the impacts of human activities (e.g., irrigation, reservoir operation, and groundwater extraction) on TWS variations over global regions by using multiple GRACE SH products and results from two different hydrological models. Two state-of-the-art models are used, namely the HiGW-MAT LSM and PCR-GLOBWB GHM, both simulate the natural as well as anthropogenic flow of water, also taking into account groundwater abstractions and associated changes in subsurface water storage. We find that despite noteworthy progress that has been made in incorporating human factors in global-scale LSMs and GHMs, significant limitations still remain in accurately simulating the spatial patters and temporal variations in TWS over all global regions. In particular, results indicate that while one model performs better in the highly managed river basins, it fails to reproduce the GRACE-observed signal in snow-dominated regions, and vice versa. Further, in some regions the uncertainties in TWS trends due to the uncertainties in forcing datasets underscore the need to consider forcing data uncertainties when evaluating the disagreements among different model results and GRACE. Our results from the partitioning of total TWS into natural and human-induced components suggest a continuing decline in TWS through 2002-2010 in the Euphrates, Ganges, Brahmaputra, Volga, and Indus river basins, which is largely human-induced. Overall, our results highlight the need to improve model parameterizations for the simulation of human water management and snow physics (e.g., glacier melts, permafrost thaw, and snow cover shrinkage) to reliably simulate the spatial and temporal variability in TWS over all global regions.

CHAPTER 3

3. Utilizing SMAP Soil Moisture Data to Improve Irrigation Parameterization in Land Surface Models

Based on:

Felfelani, F., Pokhrel, Y., Guan, K., and Lawrence, D. M. (2018). Utilizing SMAP Soil Moisture Data to Constrain Irrigation in the Community Land Model. Geophysical Research Letters 45(23): 12,892-12,902. https://doi.org/10.1029/2018GL080870

3.1. Introduction

Irrigation water use accounts for ~90% of consumptive water use globally (Scanlon, Faunt, et al., 2012) and ~40% of total freshwater withdrawals in the U.S. (Dieter et al., 2018). Over the past decade, there has been increasing interest in better simulating irrigation processes in global land surface models (LSMs), mainly because these models are capable of being coupled with atmospheric/climate models and can simulate the local to regional impacts of irrigation on both land and atmosphere. de Rosnay et al. (2003) developed one of the early schemes for examining irrigation impacts on surface water and energy balance within LSMs that are used to distribute mass and energy over and below the land surface to simulate the land hydrology within general circulation models (GCMs) and Earth system models (ESMs). Numerous studies subsequently used similar schemes to examine global and regional climate impacts of irrigation (e.g., Boucher et al., 2004; Sacks et al., 2009). These early irrigation schemes provided the basis to simulate irrigation within LSMs but were simplified in many aspects; for example, annual irrigation amount was prescribed, temporal variation in irrigation amount was ignored, and crop types and growth dynamics were not considered. Ozdogan et al. (2010) and Pokhrel et al. (2012) presented relatively advanced irrigation schemes for global LSMs by incorporating certain parameterizations not considered in previous studies (e.g., improved representation of irrigation amount, method, and timing based on crop-growth dynamics), and by coupling irrigation schemes with crop models. Numerous studies have since then used similar or modified schemes to examine the hydrologic and climate impacts of irrigation at regional to global scales (e.g., Harding and Snyder, 2012; Leng et al., 2013a; Pei et al., 2016; Pokhrel et al., 2017; Wada et al., 2014).

Advances have consequently been made in irrigation schemes used in LSMs through improved representation of the amount, method, and timing of irrigation. However, challenges and opportunities to better simulate soil moisture (SM) in irrigated areas and hence the irrigation water requirement still remain (Nazemi & Wheater, 2015a; Pokhrel et al., 2016; Wada et al., 2017). In most irrigation schemes in LSMs (e.g., Haddeland et al., 2006; Ozdogan et al., 2010; Pokhrel et al., 2012), the timing and amount of irrigation are determined based on SM deficit in the root zone. Irrigation is triggered when root-zone SM drops below a specified threshold. Irrigation water requirement is then calculated as the amount required to bring the root-zone SM to the target level. Different studies have used a range of values for threshold and target SM, which are the key variables in irrigation schemes (Haddeland et al., 2006; Harding and Snyder, 2012; Lawston et al., 2015, 2017a; Leng et al., 2013b, 2013a; Ozdogan et al., 2010; Pei et al., 2016; Pokhrel et al., 2012; Sorooshian et al., 2011). Such differences in the irrigation representation can lead to discrepancies in the estimates of irrigation water requirement and irrigation timing among models (Pokhrel et al., 2016), resulting in varying impacts on terrestrial water systems (Chaudhari et al., 2018; Felfelani et al., 2017) as well as surface energy balance and climate (Sacks et al., 2009). Further, the threshold and target SM parameterizations in most irrigation schemes employ spatially constant bulk coefficients and parameters, causing a small temporal and spatial variability of threshold and target SM and underrepresenting the heterogeneity in irrigation attributes (e.g., irrigation practices, crop-specific water requirements, and irrigation timing).

A promising approach to address some of these limitations in large-scale LSMs is the integration of spatially explicit data from satellite measurements. The recent SMAP satellite provides global surface SM with generally low errors across different climate regions (Kumar et al., 2018). Numerous studies have evaluated SMAP data with ground-based observations (Chan et al., 2016; M. Pan et al., 2016) and used SMAP data to improve hydrological and carbon flux simulations (Alvarez-Garreton et al., 2016; He et al., 2017; Kumar et al., 2015; Lievens et al., 2015, 2017). Recently, Lawston et al. (2017) demonstrated that SMAP data can be used to detect seasonal timing and spatial signature of irrigation. In another study (Brocca et al., 2018), SMAP data were incorporated into the soil water balance equation to quantify irrigation water requirement. These recent findings imply that SMAP data could potentially be used to better constrain and improve irrigation simulations in large-scale LSMs; however, to the authors' best knowledge, such potential has not yet been investigated.

We propose a novel approach for assimilating SMAP data to overcome the above limitations and enhance irrigation simulations by (1) presenting a parsimonious parameterization for extrapolating the 5cm SMAP SM to the entire root zone, (2) using a 1-D Kalman Filter (KF) for SMAP data assimilation into the irrigation scheme of the CLM4.5, and (3) accounting for bias correction of the SMAP data using an a priori scaling approach. Our hypothesis is that the assimilation of SMAP data to set the target SM can significantly improve the simulation of irrigation water requirement and SM, thus enabling advancements in the representation of irrigation in global LSMs.

3.2. Study Domain, Data, and Methods

3.2.1. Study Domain and Data

The model is set up for a region overlying the High Plains Aquifer (HPA) in central U.S., ranked first for groundwater withdrawal among all U.S. aquifers (Pokhrel et al., 2015) and a heavily-irrigated and data-rich region for ground-based SM observations (30°N-50°N, 116°W-92°W; Figure 3-1). The annual total freshwater withdrawals in HPA region are estimated at ~22-27 km^3 $year^{-1}$ during 2005-2015 (Dieter et al., 2018), of which >90% is used for irrigation.

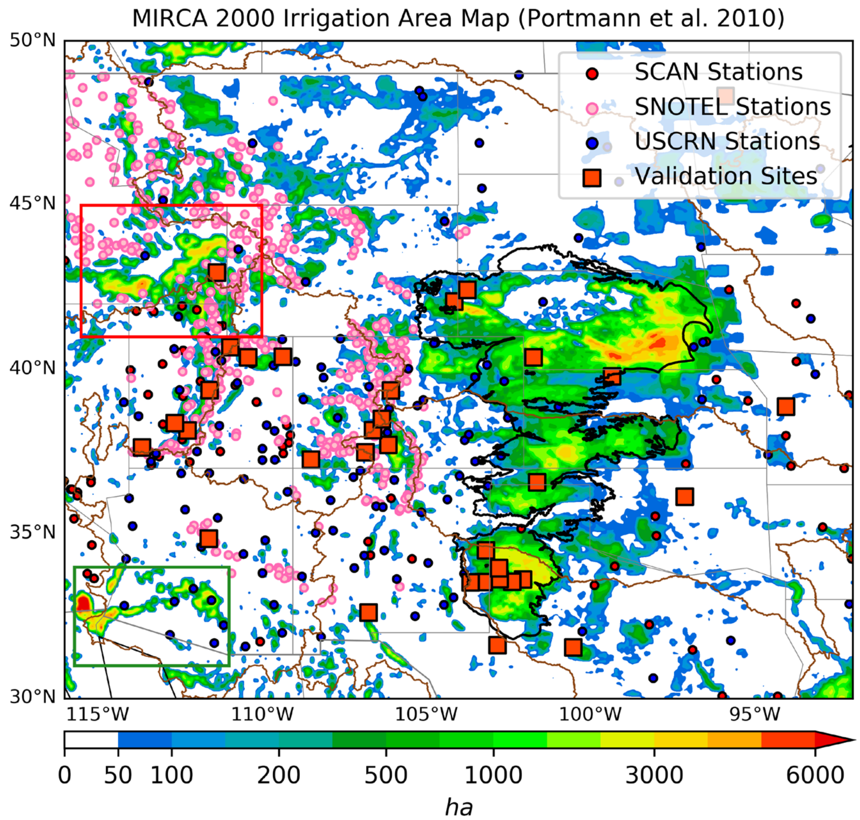

Figure 3-1. Irrigation area map over study region from Portmann et al. (2010). To fully enclose upstream areas of the rivers draining over the High Plains Aquifer (HPA), we include the

Figure 3-1 (cont'd) Missouri, Arkansas, and Colorado River basins as well as parts of the Snake River Plain (SRP) and Southwest Alluvial Basins in Arizona (ABA). The scatters show the location of ground observation stations. Stations where SM time series or vertical profiles are validated spotted with red squares. Red rectangle shows SRP region and green box delineates ABA region.

We use version 4 of the SMAP level-3 radiometer SM data for 2015-2017 period to generate the daily climatology, which is then re-gridded to 3 arc-minute model grids. The SMAP data record is short, which means that extreme events such as wet/drought cycles that might have occurred in the period could have an outsize effect on our results. However, this concern is less important than at first glance because of the rationale that irrigation maintains optimal SM levels for crop growth, preventing SM anomaly caused by wet/drought cycles. Nevertheless, since SMAP data might have been affected by other biases (Dong et al., 2018), we apply bias correction using an a priori scaling approach, in which the cumulative distribution function of SMAP data (CDF_{SMAP}) is matched with the CDF of ground observations (CDF_{grnd}) located within a sampling window of 0.5º radius and assumed as the true data (Kumar et al., 2012; Reichle & Koster, 2004). Solving the equation $CDF_{grnd}(x') = CDF_{SMAP}(x)$ for x', SMAP data (i.e., x) are scaled to the bias-corrected SM (i.e., x').

The ground-based data are taken from three monitoring networks, namely Soil Climate Analysis Network (SCAN), U.S. Climate Reference Network (USCRN), and SNOwpack TELemetry (SNOTEL), which are used for both bias correcting SMAP data and validating simulated SM (Bell et al., 2013; Bitar et al., 2012; Schaefer et al., 2007). To validate simulated irrigation water requirement, we use the USGS census data of irrigation withdrawals (Dieter et al., 2018; Maupin et al., 2014), available every 5 years since 1985.

3.2.2. Existing Irrigation Scheme in CLM4.5

The CLM (Lawrence et al., 2011; Oleson et al., 2013) is the land component of the Community Earth System Model (CESM). The CLM4.5 includes an irrigation scheme based on Ozdogan et al. (2010), which is used in conjunction with a prognostic crop module (Levis et al., 2012; Peng et al., 2018). Irrigated areas are prescribed based on the high-resolution global irrigated and rainfed crop areas from Portmann et al., (2010). The irrigation scheme uses the SM deficit approach, in which irrigation is activated when the crop leaf area index is greater than zero and water is limiting for photosynthesis depending on crop type, wilting factor, and root fraction. Irrigation water requirement is then estimated based on the difference between the prescribed target SM and the simulated SM in all soil layers within the root zone ($i = 1, n$), as:

$$SW_{def} = \sum_{i=1}^{n} max\ (SW_{tar,i} - SW_{sim,i}, 0) \qquad (3\text{-}1)$$

where, SW_{def} is the soil water deficit; $SW_{sim,i}$ and $SW_{tar,i}$ are the simulated and target soil water amount (all in kg m^{-2}), corresponding to the simulated and target SM, respectively, at i^{th} layer from the surface. If irrigation is required and $SW_{def} > 0$, irrigation water (SW_{def}) is withdrawn from runoff and applied directly to the surface at a constant rate during 6-10 am each day. Runoff is allowed to become negative when irrigation water requirement is larger than runoff (Leng et al., 2013b) so that irrigation water is not artificially suppressed. The target soil water is simply the weighted arithmetic mean of minimum soil water ($SW_{min,i}$)—that prevents crop water stress—and soil water at saturation ($SW_{sat,i}$):

$$SW_{tar,i} = \left(1 - F_{irrig}\right) \times SW_{min,i} + F_{irrig} \times SW_{sat,i} \qquad (3\text{-}2)$$

where, F_{irrig} is an empirical factor that is set globally at 0.7 to roughly replicate the global annual irrigation amount observed circa year 2000. Leng et al. (2015; 2013) suggest that the globally-calibrated F_{irrig} parameter may not be suitable for regional studies and that calibration at the scale of administrative units can result in improved regional irrigation simulations. Minimum SM (mm^3 mm^{-3}) corresponding to $SW_{min,i}$ is calculated based on the Clapp and Hornberger (1978) relation:

$$SM_{min,i} = \phi_{e,i} \times \left(\frac{\psi_{o,i}}{\psi_{sat,i}}\right)^{-\frac{1}{B_i}} \tag{3-3}$$

where, $\phi_{e,i}$ is the effective porosity, B_i is the Clapp and Hornberger parameter representing the soil type (i.e., organic matter, sand and clay fractions), and $\psi_{o,i}$ is the matric potential when stomata are fully open, set to -74000 mm, the average of matric potential at wilting point (-150000 mm) and field capacity (-3400 mm).

The existing irrigation scheme in CLM4.5 uses constant $\psi_{o,i}$ for all crops, and other effective terms in Equation 3-2 and Equation 3-3 such as $\phi_{e,i}$, $\psi_{sat,i}$, B_i, and $SW_{sat,i}$ only represent the soil type. Thus, other parameters that play crucial roles in irrigation estimation (e.g., crop type and irrigation practices) are ignored altogether due to the lack of global data. Further, as in other LSMs (e.g., Lawston et al., 2015; Pei et al., 2016), CLM4.5 irrigation scheme uses a constant bulk coefficient (here F_{irrig}; Equation 3-2) globally, which is a major limitation of the existing scheme as described above. Finally, the use of fixed irrigated areas representing circa 2000 is another structural limitation in CLM4.5 because irrigation location and extent can have significant interannual variability, especially during wet-dry transitions (Deines et al., 2017).

3.2.3. Improved Representation for Target SM in Irrigation Modeling

Our rationale is that, since SMAP can detect seasonal timing and spatial signature of irrigation (Lawston, Santanello Jr., & Kumar, 2017), SMAP SM retrievals can be used to constrain the target SM in irrigation parameterizations, enabling us to capture the effects of some of the missing irrigation attributes (e.g., irrigation water requirement for different crops) and practices (i.e., drip, sprinkler, and flood systems). In using SMAP data, we set the target SM of each irrigated grid cell on any particular day of the year as a function of daily climatology of SMAP data for the given grid cell and day of the year. The daily climatology of SMAP data is assumed to represent the daily average level of SM maintained by local farmers based on the crop type, atmospheric conditions, and irrigation practice during the SMAP period.

A realistic use of SMAP data for SM-based irrigation modeling requires vertical extrapolation of SM from 5cm to the entire root zone. Various filtering approaches have been suggested to relate the root-zone SM to surface SM (observed by satellite sensors), by applying recursive equations on time series of surface SM to update certain parameters (e.g., characteristic time length and gain factor) and then to estimate the root-zone SM (Albergel et al., 2008; Sabater et al., 2007). Here, for simplicity, we propose a parsimonious (i.e., requires minimal parameters) formulation based on the concept of Clapp and Hornberger (1978) to vertically extrapolate the SMAP SM as a function of the model soil type (represented in B_i) and the degree of saturation ($\theta^* = \frac{SM_{sim,i}}{\phi_{e,i}}$). The target SM for soil layers deeper than 5cm from the surface is then computed as:

$$SM_{tar,i} = SM_{SMAP,5cm} + SM_{SMAP,5cm} \times \left(1 - \left(1 - \frac{SM_{sim,i}}{\phi_{e,i}}\right)^{B_i}\right) \qquad (3\text{-}4)$$

where, $SM_{SMAP,5cm}$ is the SMAP SM and $SM_{tar,i}$ is the target SM in layer i, both in mm^3 mm^{-3}. Overall, the multiplying term $(1-(1-\theta^*)^{B_i})$ starts from 0 and approaches unity as the degree of saturation ranges from 0 to 1. Therefore, $SM_{tar,i}$ ranges from $SM_{SMAP,5cm}$ in the top two layers (where depth is less than 5 cm) to twice the $SM_{SMAP,5cm}$ close to the water table (where $\theta^* \approx 1$). The vertical profile of extrapolated SMAP SM thus derived is presented in Figure 3-2, which is comparable with the temporally-averaged vertical SM profile discussed in previous studies (e.g., Zeng and Decker, 2009).

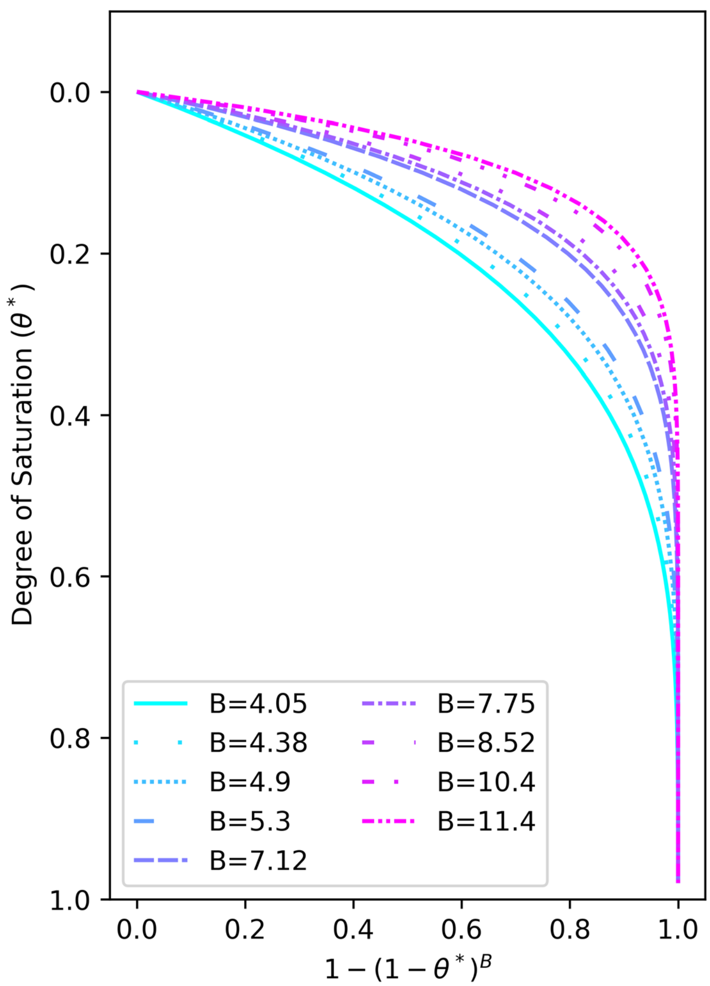

Figure 3-2. The variation of the multiplying term in Equation 3-3 (i.e., the vertical extrapolation of SMAP data) as a function of degree of saturation for different soil types.

Figure 3-2 (cont'd) The extrapolation of the SMAP top-5-cm SM data to deeper depths uses the degree of saturation and Clapp and Hornberger coefficient (i.e., parameter B in Equation 3-3). The parameter B represents different soil types (e.g., 4.05 for sand, 5.3 for silt loam, 8.52 for clay loam, and 11.4 for clay; also see Table 2 Clapp and Hornberger, 1978). Comparison of clay soils (i.e., larger B) to sandy soil types (i.e., smaller B) suggests a relatively drastic reduction of SM in sandy loams as the degree of saturation decreases toward the ground surface, implying that in clay loams that have strong capillarity, water table can be felt more near the surface compared to the sandy loams (Fan et al., 2007).

We test the original CLM4.5 irrigation scheme and two new representations for target SM using SMAP data assimilation by: (1) directly integrating raw SMAP data, and (2) assimilating SMAP data using KF with and without bias correction. In the direct integration approach, the target SM at each timestep is set by evaluating Equation 3-4, given the daily climatology of SMAP SM for the day of the year and the grid cell considered. If there is no SMAP observations for the day of the year, the scheme relies on the CLM4.5 estimation of irrigation water (Section 3.2.2). In the second approach, original and bias-corrected SMAP data are assimilated into the irrigation scheme using 1-D KF to set the target SM based on the SMAP data for the day of the year and the grid cell considered as well as adjacent spatial and temporal grid cells. That is, some degree of ergodicity is assumed in the assimilation framework following previous studies (e.g., Reichle and Koster, 2004). We note that, SMAP data are assimilated into CLM to modify the target SM representation in irrigation parameterization, and not to directly adjust SM, meaning that SM simulation is not constrained by SMAP data and hence SMAP can be used for an independent validation of simulated SM.

3.2.4. SMAP Data Assimilation using 1-D KF

In the SMAP data assimilation using 1-D KF, the state variable is updated through iterations based on a weighting scheme as:

$$X_k = X_{k_p} + K\left[Y_k - X_{k_p}\right] \tag{3-5}$$

where, X_k is the updated state of X, X_{k_p} is the model prediction of state X at iteration k, Y_k is the measurement of the state at iteration k, and K is the Kalman gain which determines the contribution of observation to the updated state variable based on the error terms of model estimation and observation. Here, the state variable (X_k) at each grid cell is the target SM that enters the KF loop with an initial value equal to the target SM from the original CLM4.5 calculated from Equation 3-2 in the main paper. Because of short SMAP data record, we assume some degree of ergodicity in the assimilation framework following previous studies (e.g., Reichle and Koster, 2004). That is, Y_k is the vector of SMAP observations neighboring the point of simulation in time and space. The vector Y_k includes the daily-averaged SMAP observation for the day of the year and the grid cell being considered, one-month temporal succession of SMAP data (from 15 days before through 15 days after) for the grid cell being considered, and SMAP observations for the neighboring cells within the range of 1.5° around the grid cell being considered. The Kalman gain is evaluated as:

$$K = \frac{P_{k_p}}{P_{k_p} + R} \tag{3-6}$$

where, R is the error variance of observations, which in multi-dimensional state vector X (i.e., in multi-dimensional KF) is presented as error covariance matrix. Here, the error variance represents the uncertainties in SMAP data. We set the SMAP error variance as a constant value for the entire study domain following He et al. (2017). Further, P_{k_p} is the error variance of the model estimate and is updated at the end of each iteration as:

$$P_{k+1_p} = (1 - K)P_{k_p} \tag{3-7}$$

In the SMAP_KF and SMAP_KF_BC simulations that use KF data assimilation, a white noise of ± 0.015 mm^3 mm^{-3} is added randomly to SMAP data following He et al. (2017). The uncertainty in SMAP data is set to 0.09 mm^3 mm^{-3} across the study area (see Table 3-1), which is based on our regional assessment of SMAP data validated by all available in-situ observations from SCAN and USCRN networks.

Table 3-1. The RMSE of the SMAP data using ground observations. The RMSE of SMAP data using SNOTEL stations, located in the western half of the study domain where irrigation is mostly underestimated in SMAP-based simulations (i.e., SMAP_raw, SMAP_KF, and SMAP_KF_BC) shows larger error compared to the other ground networks.

DOMIAN	**GROUND OBSERVATION NETWORKS**		
	SCAN (# of Stations)	**USCRN (# of Stations)**	**SNOTEL (# of Stations)**
Entire Study Domain	0.096 (85)	0.099 (127)	* (573)
Western Half (116°W-105°W)	0.095 (51)	0.069 (81)	0.137 (570)

** Almost all SNOTEL stations are in the western half of the study domain*

3.2.5. Experimental Design

We conduct five sets of offline simulations (i.e., CLM decoupled from CESM and forced by meteorological data) using CLM4.5 with: (1) no crop and irrigation schemes (NOirrig simulation); (2) the default irrigation scheme (control simulation; CTRL), (3) the improved representation for target SM by directly integrating raw SMAP data (SMAP_raw); (4) the improved representation for target SM enhanced by 1-D KF (SMAP_KF); and (5) the improved representation for target SM enhanced by using a priori bias reduced SMAP data and 1-D KF (SMAP_KF_BC). The crop model is activated for all simulations except for NOirrig. The model is set up at high resolution of 3 arc-minute (0.05º) to capture fine-scale details of irrigation processes and reduce scale mismatch with field observations. The model is first spun up for 100 years; simulations are then conducted for 1985-2016 period using the North America Land Data Assimilation System phase II (NLDAS2) forcing data (Xia et al., 2012).

3.3. Results and Discussion

Figure 3-3 shows the spatial variability of top-5cm SM from SMAP and CTRL, along with differences between the SM from SMAP and NOirrig, and SMAP_KF and CTRL, all averaged for June-August (JJA) 2015-2016. It is evident from Figure 3-3a,b that broad wet/dry patterns of SM are reasonably reproduced in CTRL. However, a significant wet bias (up to ~0.18 mm^3 mm^{-3}) compared to SMAP observations can be discerned especially in regions over HPA, SRP and western portions of the domain (Figure 3-3a,b). This SM overestimation in CTRL is due in part to the overestimation of irrigation water (discussed in Figure 3-4). However, multiple other factors such as evapotranspiration and soil resistance in CLM (Lawrence et al., 2011; Sakaguchi & Zeng, 2009; Swenson & Lawrence, 2014), biases in precipitation, and uncertainties in runoff parameterizations could have also contributed to a certain extent. To isolate the potential SM bias caused by these factors, surface SM from NOirrig is deducted from SMAP data (Figure 3-3c); a large wet bias (up to ~0.15 mm^3 mm^{-3}) is found even in the absence of irrigation. Further, the large wet bias in surface SM seen in CTRL is reduced by up to 15% and 40% over HPA and SRP, respectively, in SMAP_KF (Figure 3-3d). This bias reduction results from the lower target SM in the improved irrigation representation in SMAP_KF as dictated by SMAP data; consequently, irrigation water requirement is essentially reduced in SMAP_KF. We note that the three-month average SMAP SM is generally drier than in NOirrig (Figure 3-3c); regardless, irrigation is triggered when daily SMAP SM becomes wetter than that in NOirrig even when the monthly/seasonal SMAP SM is drier. This is likely caused by a short surface SM memory during spring-summer time and in dry regions (Rahman et al., 2015; Wu & Dickinson, 2004).

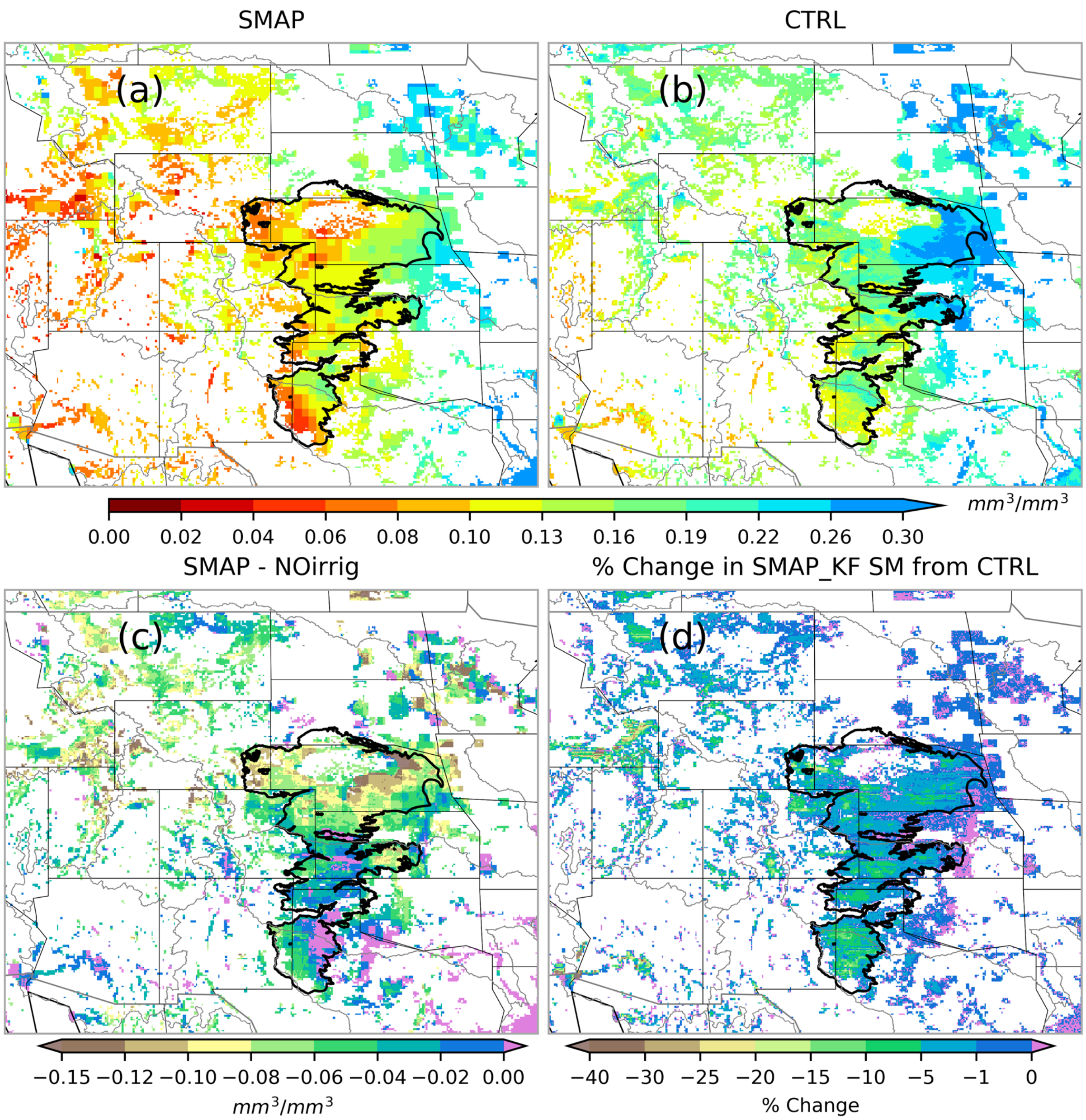

Figure 3-3. Spatial distribution of top-5cm SM (averaged for JJA of 2015-2016) from SMAP satellite observations (a), CTRL (b), the difference between NOirrig simulation and SMAP observations (c), and the change (percentage) in surface SM from SMAP_KF relative to CTRL (d).

Figure 3-4 presents the county-level comparison of simulated annual total irrigation water requirement with USGS data for census years during 2005-2015; the data for years other than 2015 are used as out-of-sample test data to evaluate irrigation simulations for non-SMAP period. Results for earlier years during 1985-2005 are shown in Figure 3-5. We note that CLM4.5 simulates irrigation water requirement without considering field losses (e.g., conveyance and application losses) but USGS data represent total withdrawals. Thus, for consistency, we convert USGS withdrawals to equivalent water requirements by multiplying withdrawals by traditional irrigation efficiency obtained from Jägermeyr et al. (2015) (Figure 3-6c).

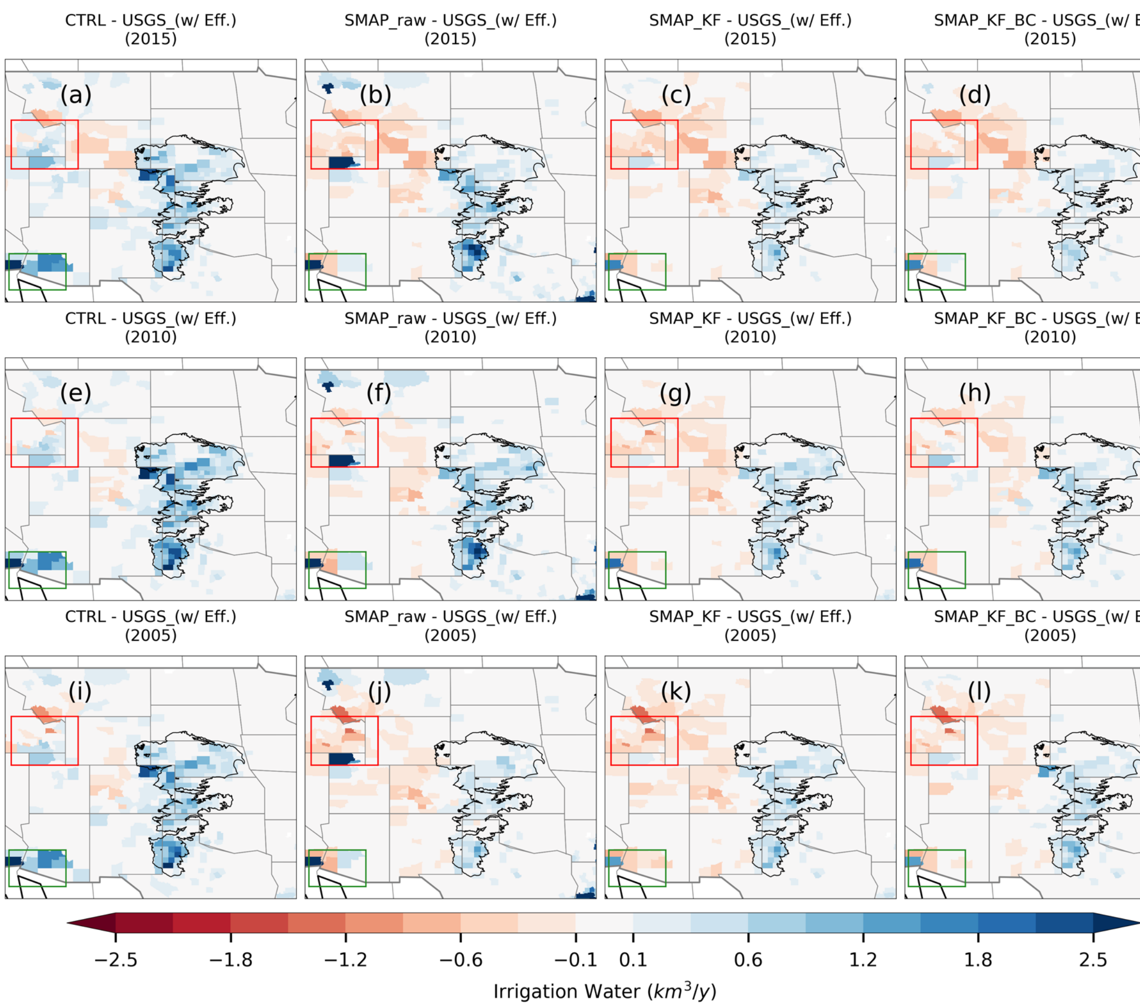

Figure 3-4. County-level difference between annual total irrigation water requirement from different simulation settings and USGS data during 2005-2015. USGS withdrawals are converted to equivalent water requirements, and 3-arc-minute model results are aggregated for each county. The dark black outline indicates HPA and the red and green rectangles show SRP and ABA regions, respectively.

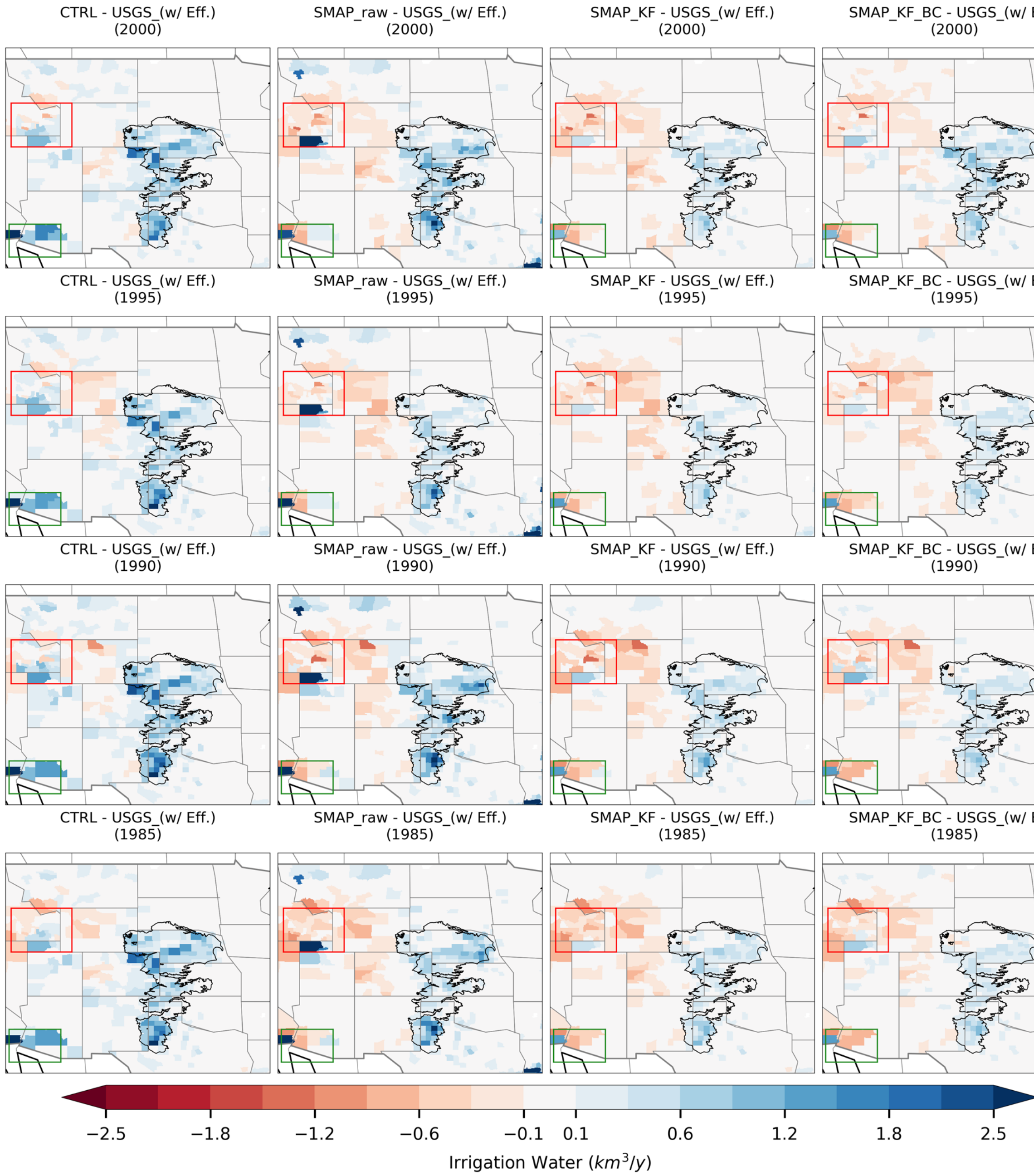

Figure 3-5. Same as Figure 3-4 but for the census years during 1985-2005.

As it is evident in Figure 3-4, significant improvements in the simulated irrigation water requirement are achieved in other simulations compared to CTRL. The CTRL overestimates irrigation water requirement for regions over HPA, Southwest Alluvial Basins in Arizona (ABA), the Snake River Plain (SRP) (green and red rectangles in Figure 3-4), Montana, New Mexico, and eastern Colorado for all years (Figure 3-4a,e,i). Conversely, CTRL underestimates irrigation in western Colorado, Wyoming, and southwest of Montana. These comparisons clearly demonstrate the deficiency in the default CLM4.5 irrigation scheme in accurately capturing the amount of irrigation water applied, especially over highly-irrigated areas (e.g., HPA and ABA; Figure 3-6a). We make the following key observations.

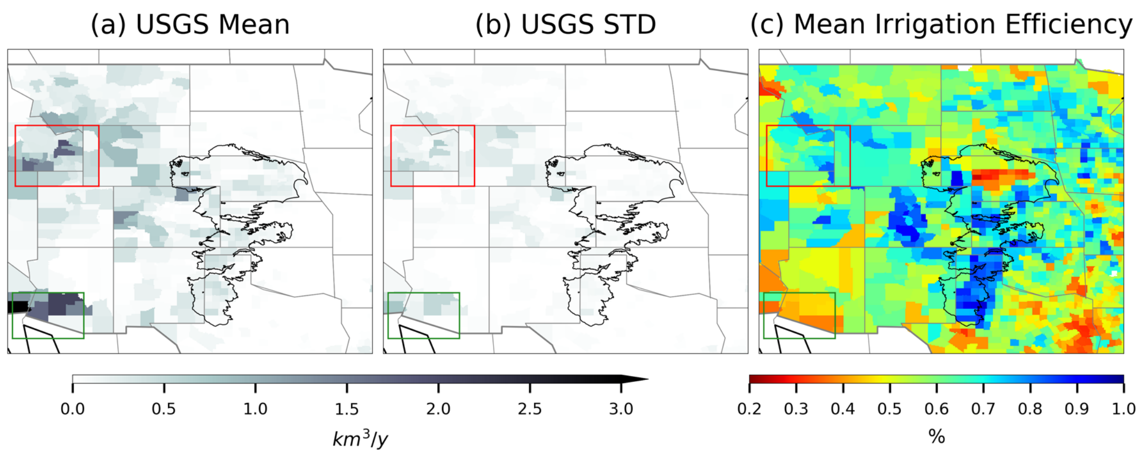

Figure 3-6. Mean (a) and standard deviation (b) of USGS irrigation water withdrawals for census years during 1985-2015. Red rectangle shows SRP region and green box delineates ABA region. The mean irrigation efficiency is also shown for counties (c) based on the data from Jägermeyr et al. (2015).

First, notable improvements are found in SMAP_raw (Figure 3-4b,f,j) compared to CTRL (Figure 3-4a,e,i), most noticeably over HPA. We find that SMAP detects a likely accurate SM in these highly-irrigated areas over HPA, thus improving the target SM and hence the irrigation water requirement compared to that in CTRL which uses a static (i.e., temporally-invariant; Figure 3-7) soil-type-based irrigation trigger threshold (Section 3.2.2). In some counties in the west of the domain, irrigation is underestimated because of relatively low SM in SMAP data over large SMAP grids (36 km) that are sparsely irrigated (Figure 3-1); that is, a decreased target SM is set in the model. The assessment of SMAP data quality against ground networks indicates that the SMAP error estimate is higher in the western half of the domain, covered mainly by SNOTEL stations (Table 3-1). This implies that the potentially lower SMAP data quality in the western half of the domain could have contributed to the underestimation of irrigation. On the contrary, there are areas of overestimated irrigation water requirement in northwestern Utah, western Montana, and western ABA, which coincide with high SM in SMAP data (Figure 3-3a).

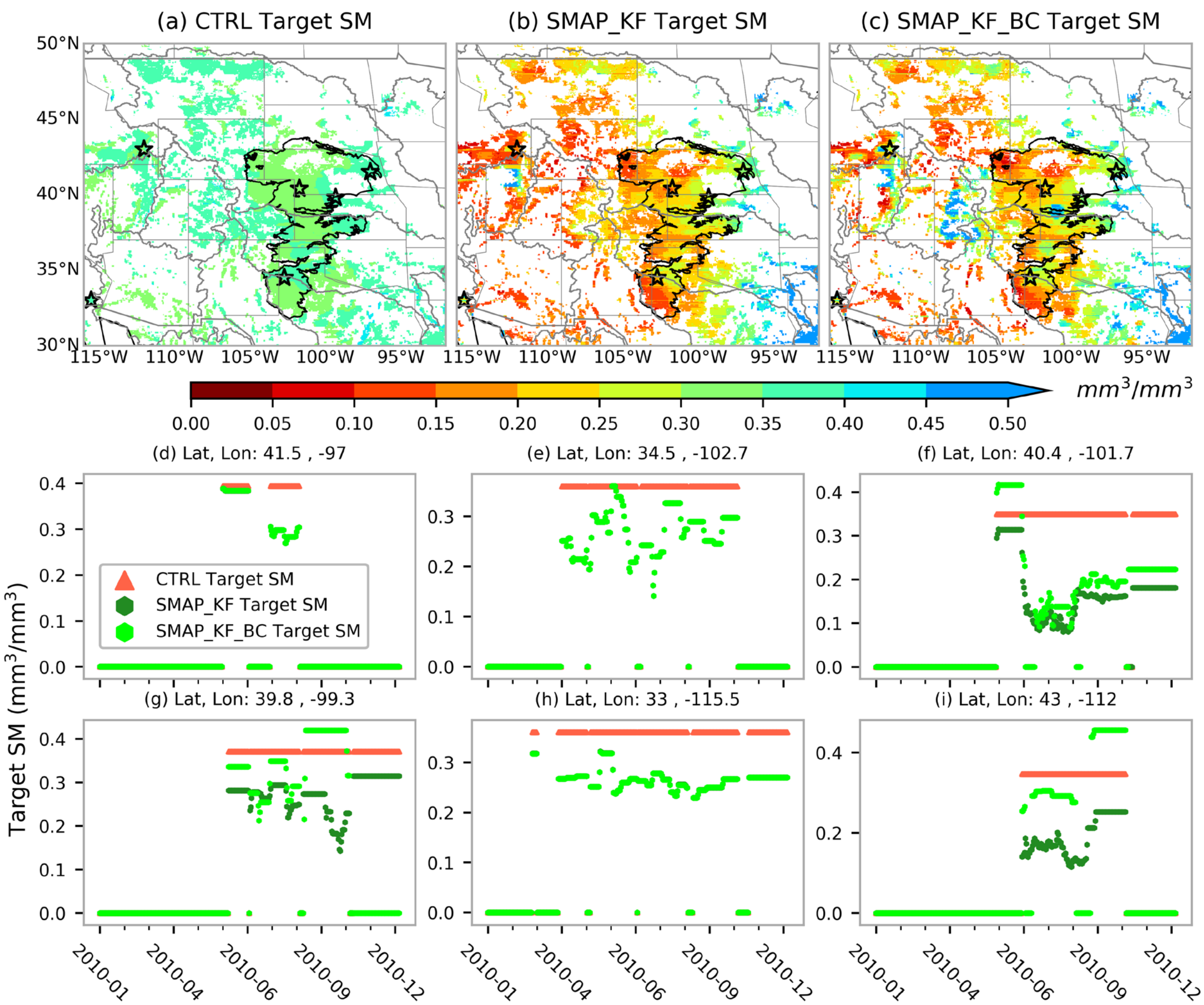

Figure 3-7. Spatial variability of target SM averaged in soil layers and for JJA of 2010 from CTRL (a), SMAP_KF (b), and SMAP_KF_BC (c) simulations. Temporal variability of target SM for sample grid cells (which are marked by stars in spatial maps a-c) is shown for the entire year 2010 (d-i). The white area in northern HPA shows that irrigation is not triggered during JJA. The target SM in the CLM4.5 irrigation scheme (CTRL) does not vary in

Figure 3-7 (cont'd) time and its spatial variability, prescribed as a function of soil type, is generally small. Bias correction locally alters the SMAP-based target SM in areas such as Colorado and Utah (c compared to b); however, most of the other areas are affected by very slight change in SMAP target SM, mainly due to similarity of CDFs of SMAP and ground data or absence of concentrated ground data in the neighboring cells.

Second, the positive bias in irrigation water requirement over HPA is further reduced for most of the years when the 1-D KF is applied (Figure 3-4c,g,k, Figure 3-5, Table 3-2, and Table 3-3). For example, the bias in total irrigation water requirement in HPA reduces by up to 60% from CTRL to SMAP_KF when compared with USGS data for years 2005, 2010, and 2015. Moreover, application of the filter also enables a significant improvement in the highly overestimated irrigation water requirement in regions of ABA, Utah and Montana in SMAP_raw (Figure 3-4b,f,j). These improvements are achieved through dampening of the potential noise in SMAP data by considering the underestimated signals from the temporally and spatially neighboring grid cells (See Section 3.2.3 and Section 3.2.4). However, KF does not reduce the underestimation of irrigation water requirement for some counties in SRP and ABA because the neighboring SMAP observations used in KF are also dry, meaning that the surrounding regions are also under-irrigated (Figure 3-4c,g,k compared to Figure 3-4b,f,j).

Finally, improvements are found in results from the application of bias correction of SMAP data using ground observations (Figure 3-4d,h,l) compared to those obtained from the application of KF alone (Figure 3-4c,g,k), especially over HPA and for years 2015, 2010, 1990, and 1985 (Table 3-2 and Table 3-3). However, these improvements are relatively small and results from SMAP_KF_BC resemble SMAP_KF results, due primarily to similarity in target SM between the two simulations (Figure 3-7). Nevertheless, results from bias correction confirm that the bias in simulated irrigation water requirement is not primarily due to the use of SMAP data for the 2015-2016 period for all simulation years.

Comparisons for other census years (Figure 3-5) show similar performance as for 2005-2015 discussed above, which is primarily because of (1) the target SM that is constant for all years despite the year-round variability in SMAP simulations, and (2) small temporal variability of USGS data throughout 1985-2015 (Figure 3-6b). In general, Figure 3-3c and Figure 3-4 suggest that CLM4.5 tends to overestimate irrigation and the improvements in irrigation simulation are achieved likely due to the reduced wet bias resulting from the constrained target SM through assimilation of SMAP data. Utilizing higher quality SMAP products with longer record could further improve irrigation estimation.

A summary of statistical measures obtained from the state-level comparison of simulated irrigation water requirement with USGS data for all census years is provided in Table 3-2 and Table 3-3 for the three states that cover the majority of HPA (i.e., Nebraska, Kansas, and Texas). These statistics corroborate our findings that promising improvements are achieved in all modified model settings compared to CTRL. For example, the root-mean-square error (against USGS data) of simulated irrigation water is reduced on average by 50% for above states in SMAP_KF compared with CTRL.

Table 3-2. Statistical measures (i.e., RMSE, MSD, and Nash-Sutcliffe efficiency coefficient) of simulated irrigation water requirement validated against the USGS data in states of Nebraska, Kansas, and Texas (i.e., the part of Texas that is inside the study domain) for the census years during 1985-2015. For the sake of consistency, irrigation efficiency is multiplied to USGS data to convert it to irrigation water requirement. The best simulations are bolded. A hypothesis test (T-test) on samples from CTRL and other simulations suggests that the average irrigation water requirement simulated in SMAP_raw, SMAP_KF, and SMAP_KF_BC experiments are significantly different (marked by *) from that in the CTRL.

State	Simulation	2015			2010		
		RMSE	MSD	Nash–Sutcliffe	RMSE	MSD	Nash–Sutcliffe
Nebraska	CTRL	0.35	0.25	-37.49	0.50	0.38	-53.42
	SMAP_raw	0.19*	0.14*	-10.08*	0.39*	0.29*	-31.15*
	SMAP_KF	0.13*	0.09*	-4.03*	0.25*	0.19*	-12.40*
	SMAP_KF_BC	0.14*	0.10*	-5.44*	0.13*	0.09*	-2.42*
Kansas	CTRL	0.29	0.14	-46.58	0.36	0.18	-51.95
	SMAP_raw	0.30	0.15	-51.58	0.27*	0.14*	-29.79*
	SMAP_KF	0.15*	0.07*	-12.09*	0.19*	0.09*	-13.72*
	SMAP_KF_BC	0.12*	0.06*	-7.16*	0.18*	0.09*	-13.14*
Texas	CTRL	0.39	0.14	-56.00	0.50	0.19	-69.56
	SMAP_raw	0.53*	0.2*	-103.11*	0.52	0.19	-76.16
	SMAP_KF	0.18*	0.06*	-10.51*	0.24*	0.09*	-15.06*
	SMAP_KF_BC	0.14*	0.05*	-6.81*	0.21*	0.08*	-11.87*

State	Simulation	2005			2000		
		RMSE	MSD	Nash–Sutcliffe	RMSE	MSD	Nash–Sutcliffe
Nebraska	CTRL	0.39	0.28	-24.12	0.44	0.33	-28.78
	SMAP_raw	0.16*	0.10*	-3.59*	0.45	0.30	-30.11
	SMAP_KF	0.20*	0.15*	-6.09*	0.20*	0.15*	-4.98*
	SMAP_KF_BC	0.17*	0.12*	-3.75*	0.26*	0.20*	-9.67*
Kansas	CTRL	0.30	0.15	-47.30	0.29	0.14	-22.93
	SMAP_raw	0.12*	0.07*	-7.38*	0.33*	0.17*	-30.47*
	SMAP_KF	0.17*	0.08*	-14.43*	0.16*	0.08*	-6.38*
	SMAP_KF_BC	0.19*	0.09*	-18.15*	0.24*	0.12*	-14.90*
Texas	CTRL	0.44	0.17	-30.01	0.35	0.13	-16.86
	SMAP_raw	0.18*	0.06*	-3.88*	0.38	0.15	-20.10
	SMAP_KF	0.20*	0.08*	-5.62*	0.16*	0.06*	-2.64*
	SMAP_KF_BC	0.23*	0.09*	-7.69*	0.20*	0.07*	-4.70*

** Indicates that the average irrigation water requirement differs significantly from the CTRL simulation (from the T-test on two related samples)*

Table 3-3. The same as Table 3-2 but for years 1985-1995.

State	Simulation	1995 RMSE	1995 MSD	1995 Nash–Sutcliffe	1990 RMSE	1990 MSD	1990 Nash–Sutcliffe	1985 RMSE	1985 MSD	1985 Nash–Sutcliffe
Nebraska	CTRL	0.335	0.221	-20.306	0.451	0.333	-30.676	0.480	0.359	-25.307
	SMAP_raw	0.155*	0.109*	-3.572*	0.581	0.397	-51.457	0.556	0.414	-34.283
	SMAP_KF	0.103*	0.062*	-1.017*	0.219*	0.165*	-6.434*	0.252*	0.188*	-6.229*
	SMAP_KF_BC	0.193*	0.144*	-6.055*	0.183*	0.129*	-4.232*	0.190*	0.129*	-3.133*
Kansas	CTRL	0.240	0.118	-17.586	0.318	0.163	-21.446	0.246	0.121	-10.921
	SMAP_raw	0.184*	0.091*	-9.898*	0.327	0.175	-22.700	0.193	0.105	-6.302
	SMAP_KF	0.114*	0.052*	-3.164*	0.180*	0.091*	-6.189*	0.120*	0.054*	-1.846*
	SMAP_KF_BC	0.140*	0.069*	-5.290*	0.130*	0.064*	-2.762*	0.127*	0.060*	-2.154*
Texas	CTRL	0.400	0.153	-22.002	0.474	0.178	-47.458	0.428	0.159	-38.623
	SMAP_raw	0.339	0.147	-15.465	0.473	0.173	-47.243	0.395	0.156	-32.820
	SMAP_KF	0.164*	0.066*	-2.839*	0.229*	0.085*	-10.359*	0.195*	0.074*	-7.218*
	SMAP_KF_BC	0.151*	0.055*	-2.277*	0.178*	0.067*	-5.842*	0.181*	0.069*	-6.068*

** Indicates that the average irrigation water requirement differs significantly from the CTRL simulation (from the T-test on two related samples)*

Figure 3-8 depicts the comparison of simulated SM using different settings with ground observations from SCAN and USCRN networks (red squares in Figure 3-1) for JJA of 2005-2006, a period chosen as a non-SMAP period. Top panels (Figure 3-8a-d) show time series of top-5m SM at four of these stations located over HPA. For clarity of view, only CTRL, SMAP_raw, and SMAP_KF_BC are shown; results from SMAP_KF are highly similar to that from SMAP_KF_BC due to the similitude of target SM in most of the areas across HPA (Figure 3-7).

Overall, CTRL fails to capture the episodes of low SM and often simulates false peaks, likely due to false irrigation timing during the growing season. The overall temporal dynamics is improved in SMAP_raw and SMAP_KF_BC, especially in terms of better capturing the episodes of low SM. Occasionally, SMAP_raw outperforms, even the SMAP_KF_BC in reproducing low SM (e.g., in year 2006); however, it fails to capture the overall temporal variability. For example, while observations show a descending trend in SM which is closely followed by SMAP_KF_BC, SMAP_raw exhibits false peaks (e.g., SCAN_2105 and SCAN_2106 during 2005 June-July, SCAN_2107 during 2005 June-July, and SCAN_2111 in 2006 June).

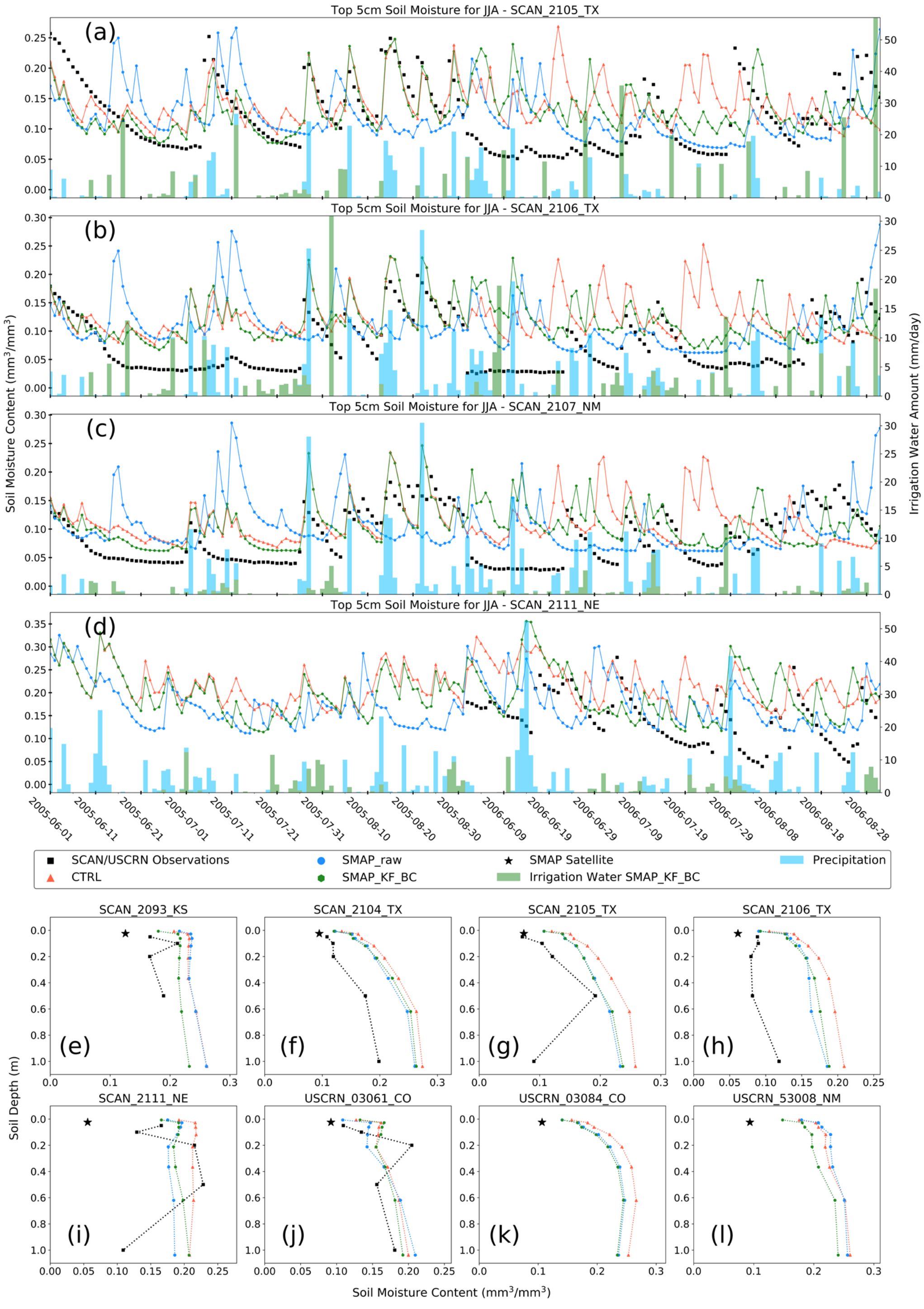

Figure 3-8. Temporal variability of top-5cm SM from CTRL, SMAP_raw, and SMAP_KF_BC simulations and SCAN observations for JJA of 2005-2006 at stations not located in irrigated areas (a-d). Vertical profiles of averaged SM over JJA during 2015-2016 from SMAP, ground observations, and CTRL, SMAP_raw, and SMAP_KF_BC simulations (e-l).

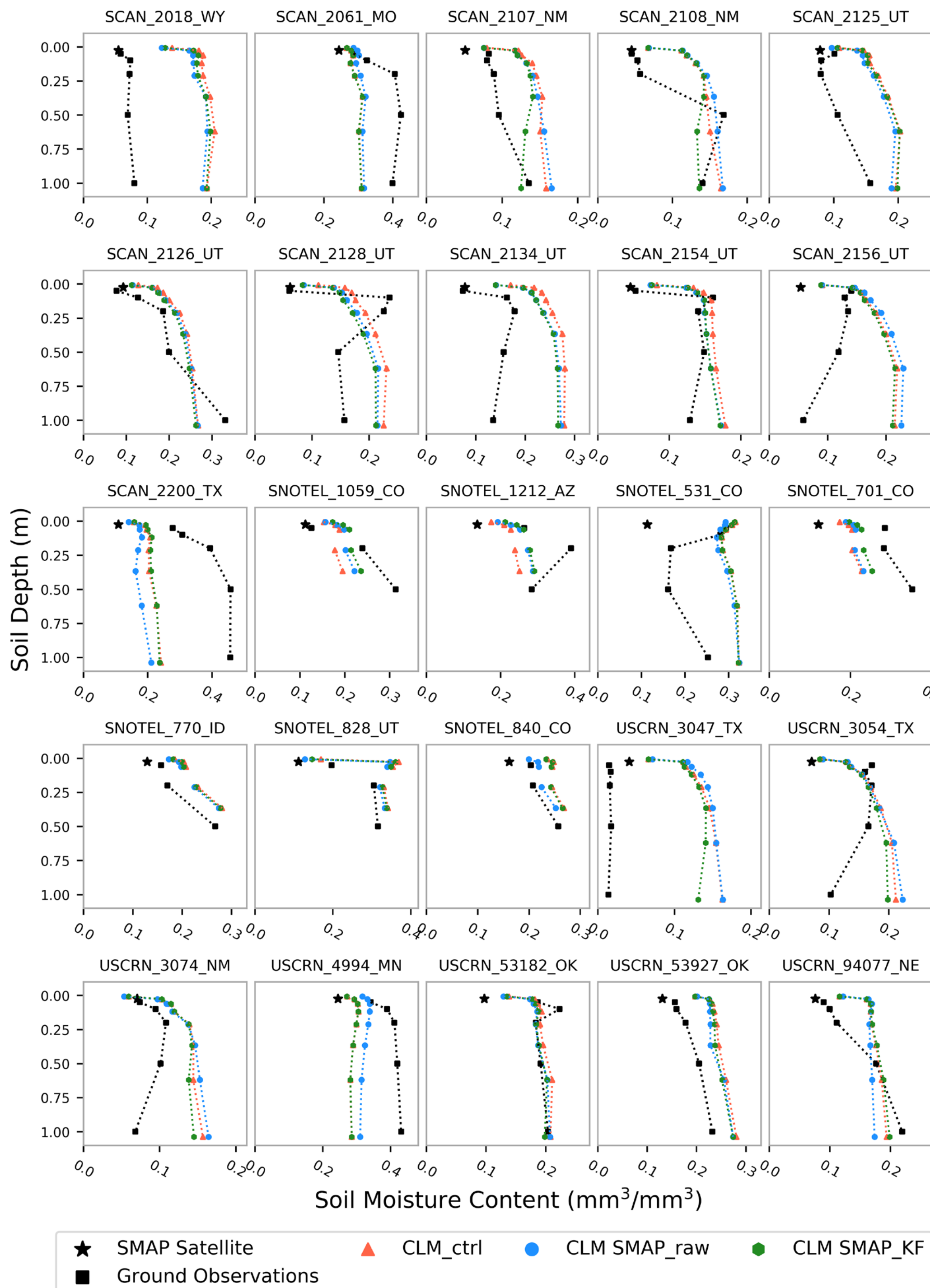

Figure 3-9. Same as vertical profiles of Figure 3-8 in the main paper but for 25 more stations. Vertical SM simulations are all averaged over JJA of years in 2005-2016 when ground observations (from SCAN, USCRN, and SNOTEL networks) are available. The top-5cm SM from SMAP is shown as a single star averaged over JJA of SMAP period.

Interestingly, SMAP_KF_BC realistically simulates the periods of low SM (e.g., SCAN_2105, SCAN_2106, and SCAN_2107 during 2006 June-July, and SCAN_2111 during 2006 July-August) as in SMAP_raw, while also capturing the observed SM dynamics (e.g., SCAN_2105, SCAN_2106, and SCAN_2107 during 2005 June-August, and SCAN_2111 in 2006 August) which is more accurately simulated in CTRL than in SMAP_raw. This demonstrates the promising performance of KF that predicts the target SM considering the uncertainties associated with SMAP and the model estimation of target SM (see Section 3.2.4). Additionally, the bar plot in Figure 3-8 shows daily precipitation stacked above irrigation water requirement from SMAP_KF_BC, in which the coincidence of most of observed dry SM events with irrigation application suggests that irrigation is triggered expectedly during relatively dry periods.

The bottom two rows in Figure 3-8 (e-l) show vertical profiles of SM in the top meter averaged over JJA of 2015-2016 from different simulations compared against SMAP and ground observations for eight stations over HPA (additional points are shown in Figure 3-9). In general, a shift in the SM profile toward the observed profile and SMAP data can be observed in the improved irrigation schemes, suggesting an improvement also in SM simulations due to SMAP data assimilation. Note that SMAP data are used only to improve irrigation representation by revising the threshold-based irrigation application, and not to directly alter SM in the model. Therefore, a perfect match between the simulated and observed SM is not expected. Further, since most of the ground stations are located in non-irrigated areas, wetter SM profile in the model is expected. The comparison of SMAP data and ground observations further suggests a fair degree of dry bias in SMAP data across the domain (Figure 3-8 and Figure 3-9), more pronounced over the western states; the underestimation of irrigation water in SMAP_raw, SMAP_KF and SMAP_KF_BC (Figure 3-4) discussed above is caused by this dry bias in SMAP. While these comparisons demonstrate that SMAP data assimilation in the irrigation scheme also improves SM simulations, the results should be interpreted with caution because this comparison is done between grid-based results and point observations from sparse networks. Despite certain caveats (Chan et al., 2016), such a comparison is common (Pan et al., 2016; Zhang et al., 2017) owing to the lack of dense observation networks and the difficulty in quantifying and comparing SM across observations and models (Dirmeyer et al., 2016, 2017).

3.4. Conclusions

This study presents a new approach to assimilate SM from SMAP satellite into global LSMs to improve irrigation representation. Results suggest that the simulation of irrigation can be improved by directly integrating SMAP data to constrain the target SM. However, we find that further improvements in simulation of irrigation can be achieved if the 1-D KF assimilation framework is applied. Use of bias corrected SMAP further improves results in some regions, but the improvements are relatively small compared to those achieved from the KF application. We conclude that, despite certain limitations, the use of SMAP data with 1-D KF better represents the target SM, thus providing robust improvements in simulation of irrigation water requirement and SM, and generally reducing wet bias in irrigation water requirement in the control simulation (e.g., by up to 60% over HPA). These results demonstrate the potential of the new parameterizations for constraining target SM using SMAP data and KF which can be incorporated into any LSM, and applied and validated globally, even for the regions where ground-based data are not available for bias correction. Future research directions include: (1) the use of higher-quality SMAP data from level-4 products with a longer record, (2) incorporation of other available information from SMAP (e.g., surface flag and land cover class) in the analysis, (3) refinement in model spatial resolution (e.g., 1 arc-minute) for better comparison of results with point measurements, and (4) consideration of field-scale details and uncertainties (e.g., in irrigation extent and practices) in irrigation representation with increased spatial resolution.

CHAPTER 4

4. Implementing a Prognostic Groundwater Model with Lateral Groundwater Flow, Conjunctive Water Use for Irrigation, and Pumping

In Preparation:
Felfelani, F., Pokhrel, Y. et al., Implementing a Prognostic Groundwater Scheme in the Community Land Model version 5 to Improve Simulation of Groundwater Depletion in Overexploited Aquifers.

4.1. Introduction

Groundwater accounts for ~40% of global irrigation and household water use and ~30% of global industrial water use (Döll et al., 2012). The strong resilience of groundwater to climate variability (Cuthbert et al., 2019) makes it a reliable source of freshwater in many (semi-)arid areas, causing an alarmingly rapid increase in groundwater use as a response to climate change and growing food demand worldwide (Wada et al., 2014). Hydrologically, groundwater acts as a buffer that directly modulates soil moisture (i.e., affected by the root water extraction and soil matric potential), and converges to streams and surface water bodies as baseflow through a relatively slow two-way water exchange between surface water and groundwater (Fan et al., 2007, 2019; de Graaf et al., 2015, 2017; Y. Zeng et al., 2018). Groundwater links with other hydrological variables such as the evapotranspiration and precipitation in critical zones where water table is shallower than 10 *m* from the surface (Condon & Maxwell, 2019). Human-induced groundwater depletion reported across the globe has gravely endangered the groundwater-supplied hydrologic systems such as rivers, lakes, and wetlands (de Graaf et al., 2019), calling on compendious studies to quantify the human-induced changes in groundwater systems toward taking immediate actions to limit water cycle perturbations.

Given that groundwater plays an important role in hydrology-human-climate interactions, several advanced groundwater models have been developed to accurately resolve complex processes of groundwater across local to regional scales. For example, the U.S. Geological Survey Regional MODFLOW model simulates the three-dimensional steady-state and transient groundwater flow based on a rectangular structured finite-difference grid (Panday et al., 2013) and recently developed for unstructured grids (Feinstein et al., 2016). The Interactive Groundwater (IGW) model is an object-oriented hierarchical patch dynamics paradigm based on nested grids that decomposes the groundwater system into levels vertically and patches horizontally to simulate groundwater flow and solute transport across multiple scales (S.-G. Li et al., 2006; S.-G. Li & Liu, 2006). These two models (i.e., MODFLOW and IGW) only simulated the sub-surface hydrology and need to be forced by recharge and surface water levels or be coupled with a surface model, e.g., a land surface model (LSM) or a global hydrological model (GHM) (de Graaf et al., 2015). ParFlow (Maxwell & Condon, 2016; Maxwell & Miller, 2005) is a rather comprehensive coupled surface water-groundwater model which fully solves the three-dimensional Richards equation (Richards, 1931) to account for variably saturated soil with very high resolution (e.g., 1 km), however high computation costs make decadal simulations over large domains (i.e., continental to global) infeasible.

In general, as the spatial extend of the models increases (i.e., from local, to regional and global), the complexity of the groundwater parameterizations degrades by a large degree to offset the limited global data availability and high computational costs (Koirala et al., 2019). In particular, groundwater is still rather poorly represented in large-scale LSMs that are designed for coupling with Earth system models (ESMs), hindering our ability to realistically simulate hydrological and climatic processes connected with groundwater and to accurately assess regional to global freshwater resources (Pokhrel et al., 2016). As an early attempt to represent groundwater in large-scale models, underground runoff was implicitly parameterized in the NASA's large-scale ground hydrology model (Abramopoulos et al., 1988) by using Darcy's law. Since then, several studies incorporated groundwater flow representation with varying levels of rigor and complexity in large-scale LSMs to explicitly simulate the aquifer storage and water table dynamics. The Variable Infiltration Capacity (VIC) (Liang et al., 2003), LEAF-Hydro (Fan et al., 2007), CLM (Lawrence et al., 2011; Leng, Huang, Tang, Gao, et al., 2013; Y. Zeng et al., 2018), the upgraded version of the MATSIRO (i.e., HiGW-MAT; Pokhrel et al., 2015), and Noah-Multiparameterization (Noah-MP; Nie et al., 2018; Niu et al., 2011) are among LSMs that have been equipped with groundwater schemes.

These LSMs have certain limitations in their groundwater schemes. First, the majority of the hydrological models (e.g., CLM, HiGW-MAT, Noah-MP) resolve only one-dimensional (i.e., vertical) soil moisture-groundwater movement and do not account for lateral groundwater flow because of (a) the insignificant effect of topography-driven lateral groundwater flow on water table in global simulations with grid sizes of 0.5^{o} / 1^{o} (Krakauer et al., 2014; Pokhrel et al., 2015), (b) the absence of groundwater pumping mechanism, and (c) the lack of global-scale hydrological datasets of permeability and depth to bedrock (Z. Xie et al., 2018). Second, the anthropogenic impacts on groundwater (i.e., through pumping) are missing in many (e.g., LEAF-Hydro, CLM) and simplistically quantified/parameterized in few models. To better replicate the real irrigation practices where groundwater storage supplies irrigation in conjunction with surface water, groundwater needs to be linked with irrigation through a pumping mechanism in the models. The pumping scheme is usually based on the simple water balance for groundwater storage. That is, the groundwater storage and water table are adjusted based on the total withdrawals (i.e., total demand), the gravity drainage from the soil column and the groundwater discharge to the river (Pokhrel et al., 2015). The impact of withdrawals from the other cells is ignored in this approach. Note that some of the GHMs (e.g., PCR-GLOBWB; Wada et al. 2017; de Graaf et al. 2015) include a relatively comprehensive setup for human activities including groundwater pumping, however, these models have been developed as stand-alone models for offline simulation (i.e., cannot be coupled with ESMs) of water resource availability and use (see the limitations in Chapter 2, Section 2.1).

To address these limitations and toward developing a comprehensive irrigation-surface water-groundwater system in global LSMs, a prognostic groundwater model is developed and coupled with the irrigation scheme which explicitly simulates groundwater pumping and also accounts for lateral groundwater flow based on two approaches: (1) the conventional Darcy's law for natural topography-driven lateral flow and (2) the steady-state well equation. The lateral groundwater flow based on the steady-state well equation (i.e., the steady-state solution to the groundwater equation with pumping as the boundary condition) is implemented—for the first time in large-scale hydrological models to the authors' best knowledge—to account for pumping-induced lateral flow. The goal of this study is to present an advanced representation of groundwater in LSMs by implementing a comprehensive prognostic groundwater model in CLM5. The new groundwater model accounts for lateral groundwater flow, groundwater pumping and realistic irrigation source from groundwater in conjunction with surface water. The specific objectives are to: (1) investigate the effects of groundwater withdrawal on the water table change across the heavily exploited U.S. aquifers; (2) quantify the impacts of pumping on the sub-surface lateral flow patterns; (3) evaluate the improvements achieved in simulations of groundwater and terrestrial water storage (TWS) with the new prognostic groundwater scheme implemented in the CLM5; and (4) test different sub-surface configuration and lower boundary condition of soil column.

4.2. Data and Methods

4.2.1. Data

We use the county-level USGS census data of irrigation water withdrawals, available for every five years since 1985 (Dieter et al., 2018; Maupin et al., 2014), to quantify the groundwater and surface water contribution to total irrigation water withdrawals which is used as input to CLM to account for conjunctive use of groundwater and surface water for irrigation. Figure 4-1 shows the county-level, groundwater-based irrigation percentage across the conterminous U.S. (CONUS) averaged for 1985-2015, which ranges from zero in most of the counties in Colorado Plateaus, to around 40% in the Central Valley Aquifer (CVA) and the Snake River Plain (SRP), to more than 90% in most of the counties in the High Plains Aquifer (HPA) and Mississippi Alluvial Plain. The county-level USGS data are further used to validate the simulated irrigation water requirement and irrigation water withdrawals supplied by groundwater.

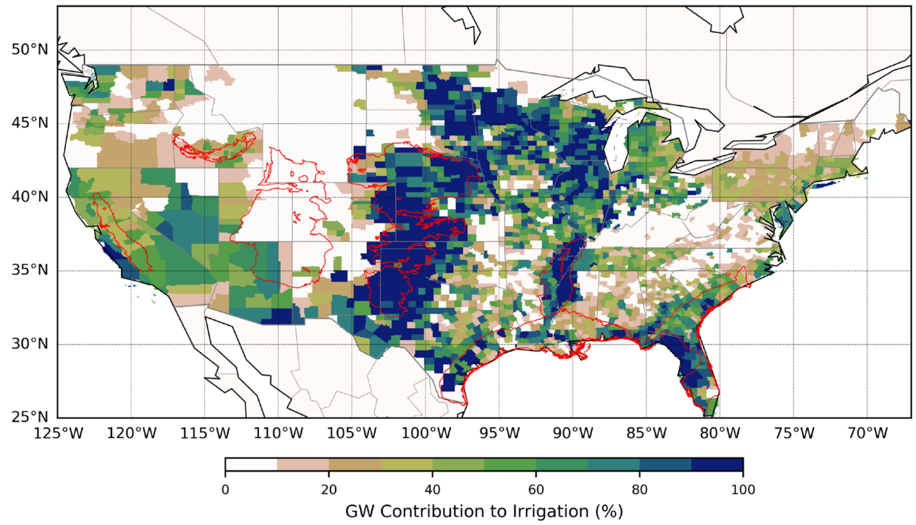

Figure 4-1. Groundwater contribution percentage to the total irrigation water withdrawal based on the USGS water use data averaged for 1985-2015. The major U.S. aquifers (i.e., HPA, CVA, Mississippi Alluvial Plain, Colorado Plateaus, Snake River Plain, Surficial, and Coastal Lowlands) are outlined with red color.

The equilibrium water table depth, aggregated to 0.25° resolution, is obtained from Fan et al. (2013) to initialize the water table condition from the equilibrium state in the CLM, which substantially reduced the spin-up period (Y. Zeng et al., 2018). The GRACE RL05 mass concentration (mascon) solutions of TWS, expressed in equivalent water height, from CSR (Save et al., 2016) and JPL (Watkins et al., 2015) processing centers are used to validate the simulated TWS anomalies and trends from CLM5. The mascon solutions have been shown to be less affected by the leakage error, less dependent on using the scaling factors, and require less post-processing (e.g., de-striping filtering is not required for mascon products) than the spherical harmonic solutions (Long, Longuevergne, et al., 2015; Scanlon et al., 2016; Watkins et al., 2015). Finally, the USGS river discharge data are also used to validate the seasonal streamflow at selected major gauging stations across the CONUS.

4.2.2. The Community Land Model version 5

We implement the new groundwater parameterizations (i.e., the lateral groundwater flow, pumping scheme, and conjunctive water use for irrigation) within the codebase of the newly released CLM5. The CLM5, the land model component of CESM2, incorporates the updates and improvements in underlying physical processes and parametrizations in hydrology, biogeochemical and surface energy sections, built upon the previous version CLM4.5 (Lawrence et al., 2019). The key changes in the hydrology section of CLM5 are: (1) introduction of a revised soil structure with variable soil depth and increased vertical resolution, improved solution to the Richard's equation with allowing for sub-steps within the CLM standard timestep, (2) replacing the head-based lower boundary condition of the soil column with a zero flux boundary condition, (3) improving the target soil moisture level in the irrigation scheme to remove the irrigation water bias, and (4) including the Model for Scale Adaptative River Transport (MOSART, H. Li et al. 2013) which simulates the streamflow, channel velocity and water depth based on the kinematic wave method. One of the new features of the CLM5 codebase is to allow selecting from multiple parameterizations available for the key processes which enables the researchers and model developers to choose the parameterizations which best address their research objectives.

4.2.3. Impact of Pumping

Most of LSMs lack groundwater pumping and those equipped with a pumping scheme have been reported to suffer from systematic biases in groundwater related fluxes and states. For instance, the rate of groundwater storage loss caused by pumping is overestimated in Noah-Multiparameterization (Noah-MP) and HiGW-MAT, attributed to the uncertainties in model parameters, scarce groundwater data, and limitations in model processes (Nie et al., 2018; Pokhrel et al., 2015).

In this study, groundwater pumping is parameterized to satisfy the groundwater-supplied irrigation reported in the U.S. Geological Survey (USGS) census data of irrigation withdrawals. The water balance of a grid cell with pumping is then computed as (Pokhrel et al., 2015):

$$\frac{dS_g}{dt} = \Delta x \Delta y R - GW_{pt} - Q_r \tag{4-1}$$

where, dS_g is the groundwater storage change, R is the net recharge, $\Delta x \Delta y$ is the grid cell area, Q_r is the groundwater discharge to the river, and GW_{pt} is the groundwater pumpage rate. Starting from the soil layer right below the water table, water is removed from the soil layers in sequential order until GW_{pt} is satisfied. Should there be a GW_{pt} residual not satisfied by amount of water in the soil layers, the underlying aquifer layer contributes. The water table depth is then lowered as:

$$z'_{wt} = z_{wt} + \frac{dGW_{pt}}{S_y} \tag{4-2}$$

where, z'_{wt} and z_{wt} are the updated and old water table depth, respectively, dGW_{pt} is the partial of groundwater total pumpage subtracted from a soil layer, and S_y is the specific yield of the aquifer diagnosed in CLM5 based on the soil properties and water table location. Finally, the liquid water storage of the soil layers and the aquifer layer are also updated based on the water extracted for pumping.

4.2.4. Lateral Groundwater Flow from Darcy's Law

The contribution of lateral groundwater flow to the total grid cell water balance depends on multiple factors such as climate, topography, aquifer properties, and pumping; however, reported to be significant in high resolution simulations (Krakauer et al., 2014). Therefore, the lateral groundwater flow has been implemented in the large-scale hydrological models with high resolution (e.g., with grid sizes of 5 km and smaller) in a handful of literature (Z. Xie et al., 2018; Y. Zeng et al., 2016, 2018), which are mostly based on the scheme presented by Fan et al. (2007). In this approach, lateral groundwater flow is also included in the groundwater mass balance for a grid cell (Fan et al., 2007) and the Equation 4-1 is generalized as:

$$\frac{dS_g}{dt} = \Delta x \Delta y R + \sum_{1}^{8} Q_n - Q_r \tag{4-3}$$

where, S_g is the groundwater storage in the column, R is the net recharge (i.e., the flux between the unsaturated soil and the groundwater), $\sum_1^8 Q_n$ is the net lateral flow between the center cell and the neighbors which driven by topography, pumping, etc., and $Q_r$is the groundwater discharge to the river which can be dropped in the steady state condition and for a non-river cell. The lateral flow between each two cells can be computed based on Darcy's law:

$$Q_n = wT\left(\frac{h_n - h}{l}\right) \tag{4-4}$$

where, T is the transmissivity, $l = \Delta x\sqrt{2}$ and $w = \Delta x\sqrt{0.5\tan\left(\pi/8\right)}$ is the width of an imaginary octagon (Figure 4-2) replaced the square grid cell to provide an equal chance for all 8 sides/neighbors to flow to/from the central cell. Figure 4-2 shows the schematic diagram of between-grid-cells lateral groundwater flow in the absence (Figure 4-2a; Fan et al., 2007) and the immediate vicinity of pumping wells (Figure 4-2b).

The prognostic aquifer transmissivity is also calculated based on the water table depth and hydraulic conductivity for different cases (Fan et al., 2007) as follows: (1) if water table depth is less than the soil column depth in the model, $T = T_1 + T_2$, where T_1 is the transmissivity of soil column up to the water table and T_2 is the transmissivity below the soil column depth.

$$T_1 = \begin{cases} \sum_{i=iwt+1}^{n} (K_i + \Delta z_i) + K_{iwt} \times (Z_{h,iwt} - Z_{wt}) & for\ layer\ i < n \\ K_n \times (Z_{h,n} - Z_{wt}) & for\ layer\ n \end{cases} \quad (4\text{-}5)$$

$$T_2 = \int_0^{\infty} K(z')dz' = \int_0^{\infty} K_n\, exp\left(-\frac{z'}{f}\right) dz' = K_n \times f \quad (4\text{-}6)$$

where, *iwt* is the soil layer index of the groundwater table level, K_i is the hydraulic conductivity of layer *i*, Δz_i is the soil thickness of layer *i*, $Z_{h,iwt}$ is the bottom interface depth of layer *i*, Z_{wt} is the groundwater table depth, *n* is the soil layer index of the deepest layer. The aquifer transmissivity for the depth lower than the model soil column (T_2) is estimated using the hydraulic conductivity of the lowest layer and applying an exponential decay with depth i.e., $K = K_n \exp\left(-\frac{z'}{f}\right)$. Finally, *f* is the e-folding length representing the complexity of sediment-bedrock profile (Y. Zeng et al., 2016) and is calculated following the hyperbolic equation presented in Fan et al. (2007).

$$f = \frac{a}{1+b\beta}\ for\ \beta \le 0.16,\ and\ f = 5m\ for\ \beta > 0.16 \quad (4\text{-}7)$$

where, *a* and *b* are parameters set to 120 m and 150 m, respectively, and β is the terrain slope; (2) if water table depth is below the soil column, the transmissivity is calculated using Equation 4-6 but for the lower bound equals to the distance from the water table depth and the bottom interface depth of layer *n* (i.e., $Z_{h,n}$).

$$T = \int_{Z_{wt}-Z_{h,n}}^{\infty} K(z')dz' = \int_{Z_{wt}-Z_{h,n}}^{\infty} K_n\, exp\left(-\frac{z'}{f}\right) dz' = K_n f exp\left(\frac{Z_{h,n} - Z_{wt}}{f}\right) \quad (4\text{-}8)$$

Note that hydraulic conductivity in the above equations is the lateral hydraulic conductivity that is determined based on the vertical hydraulic conductivity, resolved in the vertical one-dimensional soil movement, and percent of clay in the soil layer as the representative of anisotropy factor (i.e., $C_{clay} = \frac{K_{lat}}{K_{ver}}$) (Fan et al., 2007; Y. Zeng et al., 2016).

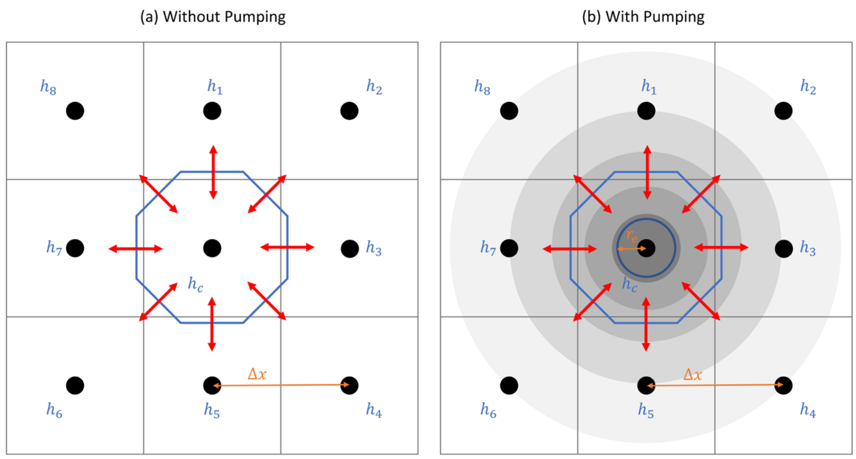

Figure 4-2. The schematic of a grid cell and the 8 neighboring cells in the absence (a) and the immediate vicinity of pumping wells. Note that the entire groundwater-supplied irrigation water requirement of a grid cell is assumed to be withdrawn from a single well (with the radius of r_e) in the center of the cell.

4.2.5. Lateral Groundwater Flow from the Steady-state Well Equation

The 2-D form of the groundwater equation with the assumption of lateral isotropy can be written in both the Cartesian coordinate system (Equation 4-9) and the radial coordinate system (Equation 4-10).

$$S_y \frac{\partial h}{\partial t} = \frac{\partial}{\partial x}\left(T \frac{\partial h}{\partial x}\right) + \frac{\partial}{\partial y}\left(T \frac{\partial h}{\partial y}\right) + \varepsilon \tag{4-9}$$

$$S_y \frac{\partial h}{\partial t} = \frac{1}{r}\frac{\partial}{\partial r} Tr \frac{\partial h}{\partial r} + \varepsilon \tag{4-10}$$

where, S_y is the specific yield of the aquifer, h is the hydraulic head, T is the transmissivity, and ε is the sink/source term. The analytical solution of the radial partial differential equation (Equation 4-10) for the steady state condition and with considering the pumping in the boundary condition at well radius (i.e., $r = r_0$, $Q = K\frac{\partial h}{\partial r} \times 2\pi r_0 h$, where Q is the pumping rate$\left[\frac{\mathrm{L}^3}{\mathrm{T}}\right]$) is

$$\left(\frac{1}{2r}\left(\frac{Q}{\pi} + \varepsilon r_0^2\right) - \frac{\varepsilon r}{2}\right) dr = T dh \tag{4-11}$$

Assuming that the head change due to pumping is negligible compared to the aquifer thickness and evaluating the above integral, we reach the solution as Equation 4-12 which can be simplified as Equation 4-13 (known also as the well equation) should there be a known head (i.e., $r = R, h = H$).

$$\left(\frac{Q}{2\pi} + \frac{\varepsilon r_0^2}{2}\right) ln\, r - \frac{\varepsilon r^2}{4} = Th + C \tag{4-12}$$

$$\left(\frac{Q}{2\pi T} + \frac{\varepsilon r_0^2}{2T}\right) ln\frac{R}{r} - \frac{\varepsilon(R^2 - r^2)}{4T} = H - h \tag{4-13}$$

Solving Equation 4-13 for Q, applying it between the effective well block radius $r = r_e$ (Anderson et al., 2015) and the center of a neighbor cell (i.e., $r = a = \Delta x$ or $\Delta x\sqrt{2}$), together with considering 8 neighboring grid cells for a given cell (Figure 4-2), we can assume the total pumped water in the center cell is supplied by the lateral groundwater flows from the 8 neighboring cells following (Anderson et al., 2015) which yields

$$Q_{lat} = \frac{Q}{8} = \frac{\pi T\left(z_{wt@r_e} - z_{wt@a}\right)}{4ln\left(\frac{a}{r_e}\right)} + \frac{\varepsilon\pi(a^2 - r_e^2)}{16ln\left(\frac{a}{r_e}\right)} - \frac{\pi\varepsilon r_0^2}{8} \tag{4-14}$$

where, $z_{wt@r_e}$ and $z_{wt@a}$ are the water table depth at $r = r_e$ and $r = a$. Adapting the approach introduced by Anderson et al. (2015) for the 8-neighbor case, the effective well block radius is calculated as $r_e = 0.178\Delta x$ (Figure 4-2b). In case the recharge is explicitly resolved and directly added to groundwater storage, the recharge terms in Equation 4-14 need to be ignored.

4.2.6. Experimental Settings

We conduct three sets of CLM5 off-line simulations (see Table 4-1) forced by the North America Land Data Assimilation System phase II (NLDAS2) meteorological data. Table 4-1 illustrates the groundwater and sub-surface configurations for all simulations. In the control simulation (hereafter CTRL), the aquifer beneath the soil column is activated and the drainage (q_{drai}) from the lowest soil layer is controlled by a head-based lower boundary condition (i.e., $q_{drai} = q_i + \frac{\partial q_i}{\partial \theta_{liq,i}} \partial \theta_{liq,i}$, where q_i is the water flux across the lowest interface and $\theta_{liq,i}$ is the liquid volumetric soil moisture). This groundwater parameterization was initially introduced in CLM4.5 but is now implemented in CLM5 and available to choose via namelist control. The water table depth is not restricted in this groundwater setting and can vary from 0 to 80 m.

Table 4-1. The configuration of groundwater, sub-surface runoff generation, and pumping.

Simulation	Lower BC	Aquifer Layer	Sub-surface Runoff	Pumping	Soil Configuration	Lateral Flow
CTRL	Head-based	Active	Exponential	No	20 Layers, 8.5m	No
DarcyLat_NoPump	Head-based	Active	Exponential	No	20 Layers, 8.5m	Darcy
DarcyWellLat_Pump	Head-based	Active	Exponential	Yes	20 Layers, 8.5m	Darcy and Well Eq.

In CLM5, there is also a new sub-surface hydrology scheme in which the bulk aquifer layer below the model soil column is removed and the head-based lower-boundary condition is replaced by a zero-flux boundary condition at the base of the soil column. This scheme is suggested to improve the simulated TWS seasonal and interannual variability (Swenson & Lawrence, 2015). However, the major drawback of this new CLM5 groundwater parameterization (i.e., removing the aquifer layer and imposing a zero-flux boundary condition) is that the water table is restricted to vary only within the soil column depth (e.g., 8.5 m) which is an unrealistic restriction, particularly over arid and semi-arid regions where water table can be deeper than 8.5m. Therefore, given that the primary objectives of this study are to improve the simulation of water table dynamics and better capture the impact of extensive groundwater pumping in the CONUS domain, we select the active aquifer layer and the head-based drainage for our simulations.

The sub-surface runoff in CTRL decays exponentially according to water table depth, i.e., $q_{sub} = \Theta_{ice} q_{drai,max} \exp(-f_{drai} z_{\mathrm{wt}})$; where, Θ_{ice} is an ice impedance factor, $q_{drai,max}$ is the maximum sub-surface runoff when $z_{wt} = 0$ and is set to $q_{drai,max} = 10\sin(\beta)$ to best compare with observations in global simulations, β is the mean grid cell topographic slope in radians, and f_{drai} is the decay factor (Niu et al., 2005).

The next experiment (hereafter DarcyLat_NoPump) is setup to implement the lateral groundwater flow based on Darcy's Law (Fan et al., 2007) into the CLM5 considering the same sub-surface configuration as CTRL (i.e., the same lower boundary condition, the same sub-surface runoff parameterization, and the activated aquifer layer). The last experiment (hereafter DarcyWellLat_Pump) is designed to implement groundwater pumping as well as the lateral groundwater flow based on combination of Darcy's Law and wells hydraulics. That is in calculating the between-cell lateral groundwater flow, in case one or both of the grid cells are pumping cells (i.e., a grid cell with a non-zero groundwater-supplied irrigation demand) Equation 4-14 applies, and if both are natural cells (i.e., without pumping) Equation 4-4 applies. This simulation, likewise, uses the same soil configuration and lower boundary condition as CTRL.

The parallel computing architecture in CLM5 needs to be examined and modified to enable communications between processors. Figure 4-3 depicts the CLM static strip partitioning of 473,439 active (i.e., only land) grid cells through which the grid-level tasks are assigned to 320 processors. The strip partitioning scheme in the original CLM is well suited (i.e., compared to the block partitioning scheme) to 1-D processes where there is no inter-task communication. However, incorporation of the lateral groundwater flow requires processors to pass information (transmissivity, water table depth, pumping rate, etc.) between the neighboring cells. CLM is written in modern object-oriented Fortran which allows class-based behavior by defining the methods and derived types containing the data through separate instances (Akin, 2003; Clerman & Spector, 2011). Therefore, for the sake of efficiency and to benefit from the object-oriented features, the grid cell indices associated with the 8 neighbors of each cell are identified and saved (to be called later) as the instances of a public derived type only once and in the beginning of the simulation.

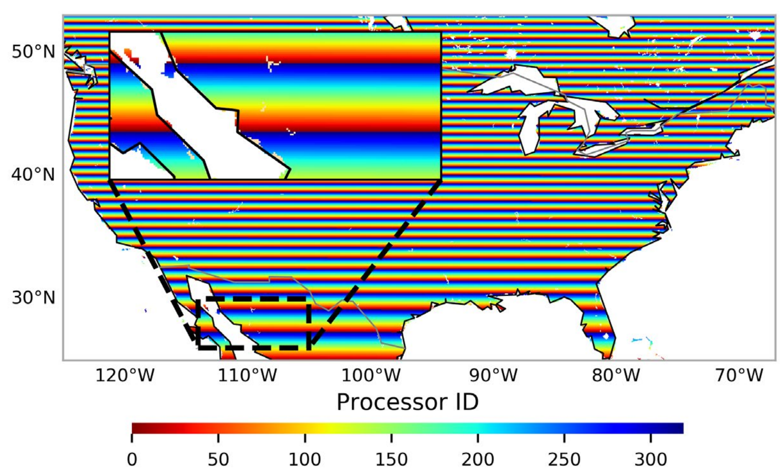

Figure 4-3. A schematic of the static strip partitioning of the grid cells across the CONUS. A total of 320 processors is used in this experiment to simulate 473,439 active grid cells in the domain.

For the model spin-up, the water table depth in the CTRL and DarcyLat_NoPump simulation is initialized from the equilibrium water table depth from Fan et al. (2013), both spun up for 120 years cyclically using the available atmospheric forcing data, and then the actual CTRL and DarcyLat_NoPump simulations are conducted for 1998-2016. The DarcyWellLat_Pump simulation is started from the DarcyLat_NoPump (i.e., spun up for 120 years), with an extra spin up of 10 years with activated pumping to reach the new equilibrium state over the highly exploited aquifers, and then the actual simulation is conducted for 1998-2016.

4.3. Results and Discussion

4.3.1. Spatial Variability of Groundwater Table Depth

Figure 4-4 shows the comparison of the average groundwater table depth from the CLM simulations at 3 arc-min resolution for 1998-2016 (Figure 4-4b-d) with equilibrium water table depth (i.e., climatologic mean that represents the long-term balance between the climate-driven recharge and the topography-driven lateral flow) at 0.25° resolution from a fused product (i.e., the LEAF-Hydro model simulation constrained with observations) by Fan et al. (2013) (Figure 4-4a). In general, water table depth is controlled by the balance between the vertical (e.g., recharge from the soil column to the aquifer and capillary flux) and lateral (i.e., the base flow and lateral groundwater flow) water fluxes (Fan et al., 2007; Swenson & Lawrence, 2015).

In the CTRL simulation where the lateral groundwater flow is absent, the spatial portrait of groundwater table depth mostly reflects climate patterns. That is, across the eastern U.S. with abundant precipitation, which partly ends up as recharge to the aquifer, the water table resides within shallow depths (i.e., maximum 10-14 m from the land surface). Conversely, over the southwestern U.S. (mostly arid and semi-arid climate), water table depth is much deeper (i.e., up to 80 m) owing to less recharge and also the steep and rugged topography (i.e., the slope term in the sub-surface runoff parameterization). The comparision of CTRL with the equilibrium water table depth from Fan et al. (2007) highlights the differences in the magnitudes and spatial patterns, for example across the Appalachians mountains in the southeast as well as the northwest where CTRL simulates much shallower water table. These discrepancies could be attributed primarily to the differences in the parameterizations of the key processes (e.g., elevation representation, sub-surface runoff generation, boundary conditions) in the groundwater schemes of the two models (CLM5.0 and LEAF-Hydro) (Y. Zeng et al., 2018).

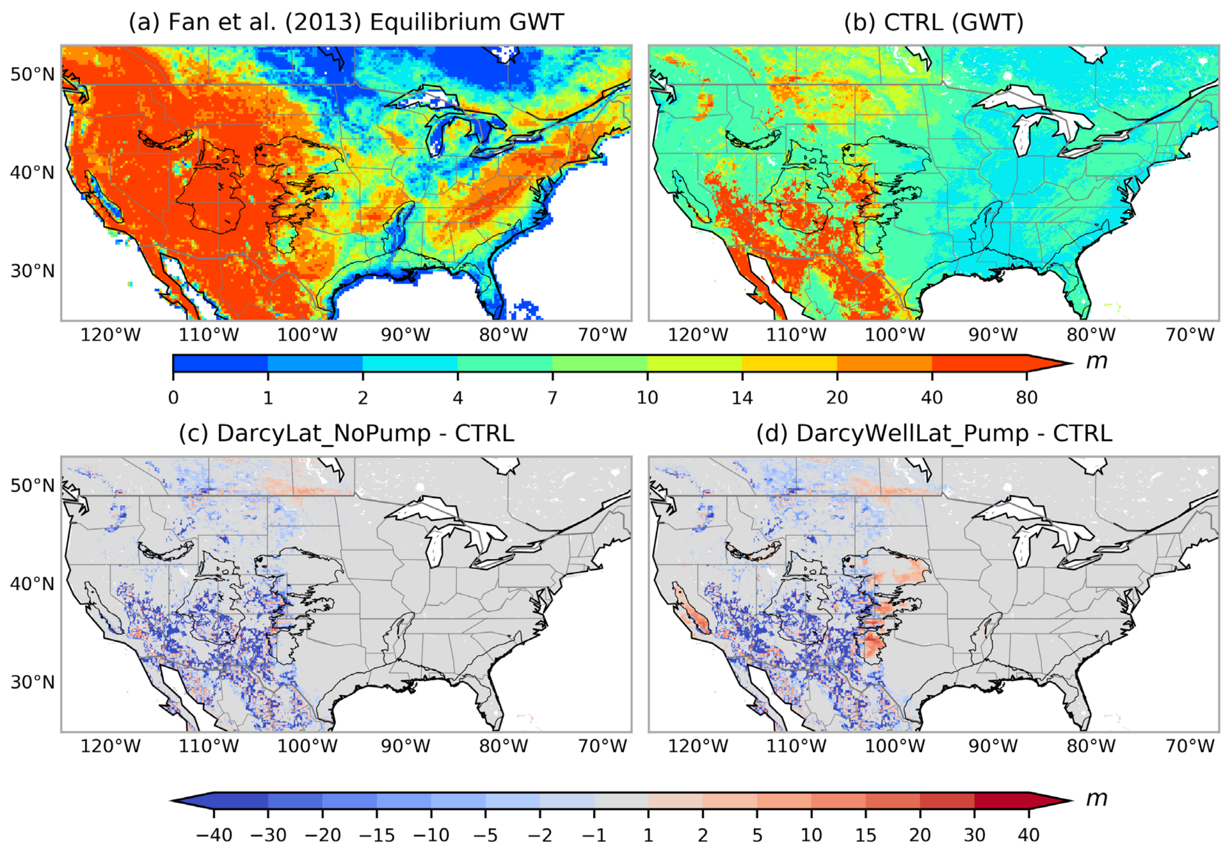

Figure 4-4. Equilibrium water table depth (m) from Fan et al. (2013) (a) and CLM simulations (b-d) for 1998-2016. Long-term average groundwater table depth from CLM CTRL simulation (b), and the differences between DarcyLat_NoPump and DarcyWellLat_Pump against CTRL (c, d) are shown. The major U.S. aquifers (i.e., HPA, CVA, Mississippi Alluvial Plain,

Figure 4-4 (cont'd) Colorado Plateaus, Snake River Plain, Surficial, and Coastal Lowlands) are outlined with black color.

Next, after adding the lateral flow based on Darcy's law, shown as the difference between DarcyLat_NoPump and CTRL (Figure 4-4c), the average water table depth across the eastern U.S. remains within the range of -1 m to +1 m difference from the CTRL simulation due a small water table gradient between the grid cells, whereas the large water table gradients across the west and southwest drive large lateral flows between the intermountain hills and valleys. Note that positive (negative) values mean deeper (shallower) water level compared to CTRL. Finally, the results shown as the difference between DarcyWellLat_Pump and CTRL simulations (Figure 4-4d) demonstrate that groundwater pumping imposes large depletion over the managed aquifer systems. For example, a water table decline of up to ~20-25 m can be seen over the southern and central parts of HPA region, which are intensively irrigated using groundwater. Further, water table drawdown of up to ~17 m and 10 m stands out over the southern part of CVA (i.e., the San Joaquin River basin) and SRP, respectively.

4.3.2. Groundwater Level Change in HPA and CVA

HPA and CVA are the most heavily exploited aquifers in the U.S., ranked first and second in terms of the groundwater withdrawals and are extensively monitored by the USGS (Scanlon, Faunt, et al., 2012). HPA overlays ~450,000 km^2 over the central U.S., mostly made of alluvial deposits and generally classified as unconfined, containing ~30% of the total U.S. irrigated acreage, producing ~10% of the total U.S. crop value, and supplying more than 95% of the total irrigation demand in the region (Dennehy et al., 2002; Konikow, 2013; Maupin et al., 2014; Smidt et al., 2016). The USGS continuously monitors and reports the changes in groundwater level across HPA before the irrigation season starts every year using over 3,000 wells (McGuire, 2011).

Figure 4-5 compares the spatial patterns of accumulated water level change from CLM simulations (a-c) and USGS report (d) provided at 500 m resolution (McGuire, 2017). The USGS report (Figure 4-5d) illustrates water level changes from predevelopment (~1950) to 2015, which ranges from ~25 m increase over a small region in Nebraska (i.e., along the Platte River) to ~70 m depletion in Texas. While the largest irrigated fields are developed in the northeast of HPA (Figure 3-1), the USGS map shows little to no depletion in that region. Contrarily, there are patches of water level increase in the north-center part of Nebraska due to increased recharge in recent times (Scanlon, Faunt, et al., 2012). However, towards the south of HPA, the reported depletion reaches to ~20 m at the border of Nebraska and Colorado, ~50 m in the southwest of Kansas and north border of Texas, and exceeds 50 m in the southern HPA. In general, the north-to-south water level gradient can be explained mainly by the annual recharge which has eventuated in unsustainable groundwater withdrawals in the central and southern HPA.

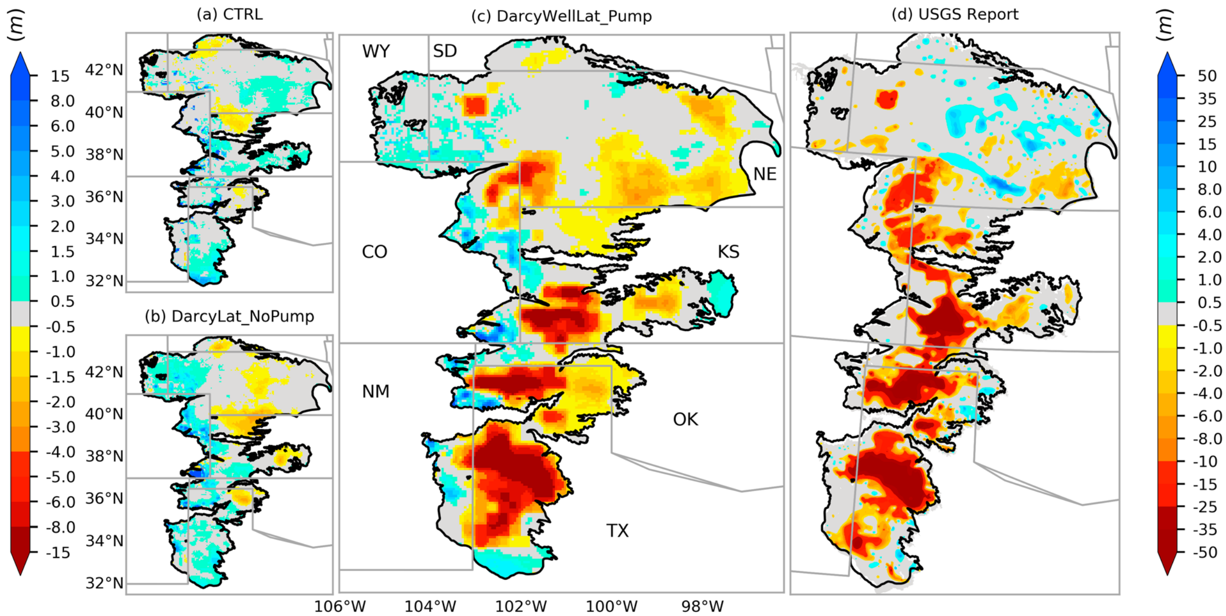

Figure 4-5. Groundwater level change across HPA accumulated for 2000-2015 from CLM5 simulations (a-c) compared with the USGS reported water level change for predevelopment (~1950) to 2015 (d). Note that the three CLM simulations (a-c) share the left color bar.

As seen in Figure 4-5a-b, the simulated water level changes from CTRL and DarcyLat_NoPump present relatively similar spatial variability for 2000-2015 period, suggesting that changes in these simulations are mostly climate-driven. These two simulations fall short in capturing the reported depletion hotspots across HPA by a large margin. A minor depletion of 0.5-1.5 m is discernible at the border of Nebraska and Kansas and the northeast corner of Texas, both inconsistent with the critical regions reported by the USGS map. Further, the increasing water level on the west side of HPA is ascribed to large recharge on the west border of HPA which is then spread over by lateral groundwater flow, controlled by the water level gradient and the transmissivity in DarcyLat_NoPump and DarcyWellLat_Pump simulations (Figure 4-5b-c).

Implementation of groundwater pumping (i.e., removing the groundwater-supplied portion of irrigation water from aquifer storage) and the lateral flow based on the well equation results in a significantly improved simulation of the accumulated water level change (Figure 4-5) in which most of the hotspots of groundwater depletion in the central and southern regions are well captured. The groundwater drawdown in DarcyWellLat_Pump reaches ~6 m at the border of Colorado and Nebraska, ~11 m over the southwestern Kansas, and ~15 m in Texas for 2000-2015 period. The major difference between the USGS map and DarcyWellLat_Pump arises in Nebraska. While most of the regions with small water level change (i.e., -0.5 to 0.5 m) in central and northern Nebraska and even the small region of large depletion in northwest of Nebraska are promisingly generated, ~0.5-3 m drawdown is simulated across the northeast and south-center of Nebraska that does not exist with the comparable spatial extent in the USGS map. The over-depletion in Nebraska can be associated with overestimation of irrigation water owing to the uncertainties in input data (e.g., irrigation fraction map and crop types which impact the estimation of irrigation water requirement), and underestimation of recharge, especially irrigation return flows.

CVA with an area of ~52,000 km^2 includes the Sacramento Valley in north, the San Joaquin Valley in the center and the Tulare Basin in the south of CVA. Unlike in HPA, surface water accounts for a large fraction (~50%) of irrigation water over this arid to semi-arid region (Bertoldi, 1989). Over 90% of croplands and pasturelands are irrigated in CVA (Scanlon, Faunt, et al., 2012). Geologically, the aquifer thickness varies from ~460 m in the Sacramento Valley to ~880 m in the San Joaquin Valley and is unconfined in the shallow parts and semiconfined or confined in the deep parts to the south (Bertoldi, 1989; Konikow, 2013).

Figure 4-6 compares the water level changes from the CLM5 simulations (a-c) accumulated for 2000-2015 with the USGS estimated changes (d) from the predevelopment (~1860) to 1961 across CVA (Bertoldi et al., 1991; Williamson et al., 1989). Note that the simulation period in this study falls entirely after the period in USGS report (i.e., ~1860-1961), however, since the intensive groundwater pumping across CVA developed more than a century ago and has been maintained until now, we expect to see a relatively similar spatial patterns of groundwater drawdown over time. Further, this type of comparison also has done by previous studies (e.g., de Graaf et al., 2019) due to the limited data availability.

According to the USGS model, the maximum depletion (i.e., 12 to 120 m) had occurred in the Tulare Basin in the southern CVA with the utmost depletion on the west (Scanlon, Longuevergne, et al., 2012). The water level declines in the Sacramento and San Joaquin Valleys are less severe, ranging from 0 to 24 m, and yet small regions of water level rise of ~3 m are estimated, e.g., in the Delta on the west. In the absence of groundwater extraction and lateral groundwater flow, the CTRL only reflects the vertical climate-driven water level changes (Figure 4-6a). The CTRL shows declines of less than 2 m in the valleys, mainly due to prolonged drought and reduced recharge, and rises in the range of 0-2 m in the surrounding areas with higher elevation and more precipitation.

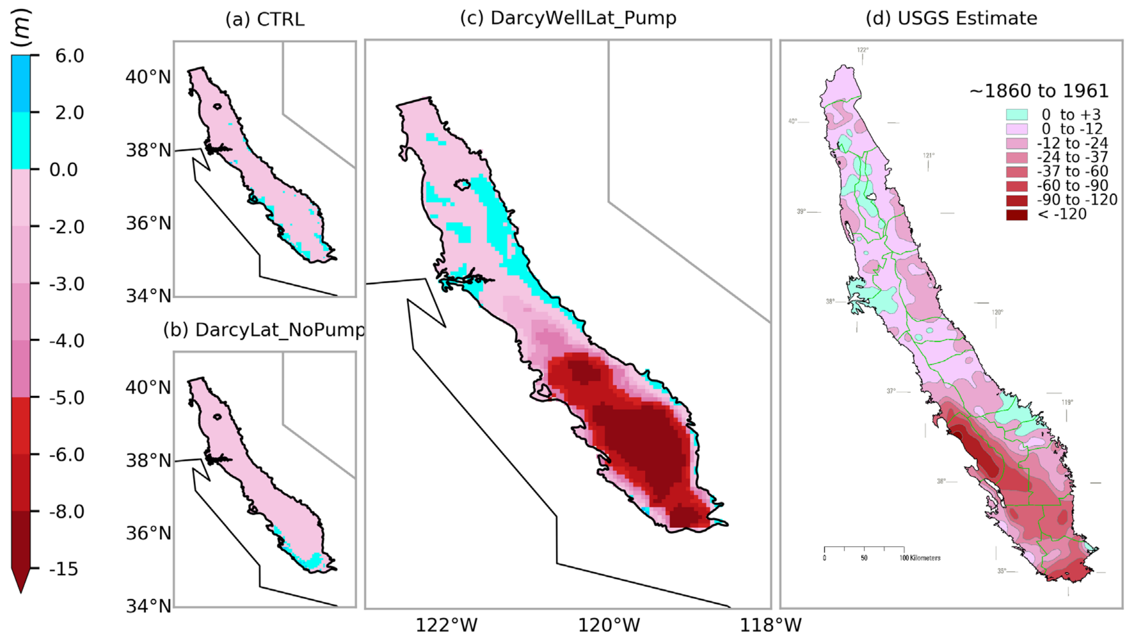

Figure 4-6. Groundwater level change across CVA accumulated for 2000-2015 from CLM5 simulations (a-c) compared with the USGS estimated water level change for predevelopment (~1860) to 1961 (Faunt, 2009; Williamson et al., 1989) (d). Note that the three CLM simulations (a-c) share the left color bar.

Similar to HPA case, the DarcyLat_NoPump simulation compares favorably with the CTRL with a relatively small (0-2 m) groundwater decline in most of CVA and 0-2 m increase on the south edge; however, the lateral flow extends the central depletion to the west borders of the aquifer and reverses the rises in CTRL to declines in DarcyLat_NoPump. The results from the DarcyWellLat_Pump (Figure 4-6c) suggest an overall improvement in simulating the groundwater level changes in the highly managed CVA. The growing intensity of simulated water level drop towards the southern San Joaquin Valley and central Tulare Basin matches with the well observations and the findings from other studies (de Graaf et al., 2019; Scanlon, Longuevergne, et al., 2012; Williamson et al., 1989). The greatest depletion (i.e., ~12 m) is simulated in the center of the Tulare Basin, a bit shifted compared to the maximum depletion location estimated by the USGS model (Figure 4-6d). Finally, a ~0-1.5 m water level declines as well as ~0-0.7 m rises are simulated in the northern part of the aquifer (i.e., the Sacramento Valley and the Delta) which show good consistency with the observations.

Figure 4-7 depicts the comparison of the simulated groundwater level change for HPA (a) and CVA (b) with the annual/biennial USGS observations for HPA (McGuire, 2014, 2017) and the monthly well analysis for CVA (Faunt, 2009; Pokhrel et al., 2015; Scanlon, Longuevergne, et al., 2012). Consistent with the spatial maps across HPA (Figure 4-5), the CTRL and DarcyLat_NoPump results show a relatively stable temporal patterns with increases and decreases but fluctuating close to the zero line, as opposed to the USGS cumulative water level changes which show a continuous fall-off from 2001 to 2015, reaching to more than 2 m of depletion by 2015 (Figure 4-7a). Among CLM simulations, the DarcyWellLat_Pump shows the best agreement with the USGS data by starting to decline from 2009 and reaching 1 m of drawdown by the end of 2015. This simulation levels off at 2012 and maintains the water level until the end of 2015, mainly due to increased amount of recharge in this period that also causes the CTRL and DarcyLat_NoPump simulations to rise up to 0.5 m.

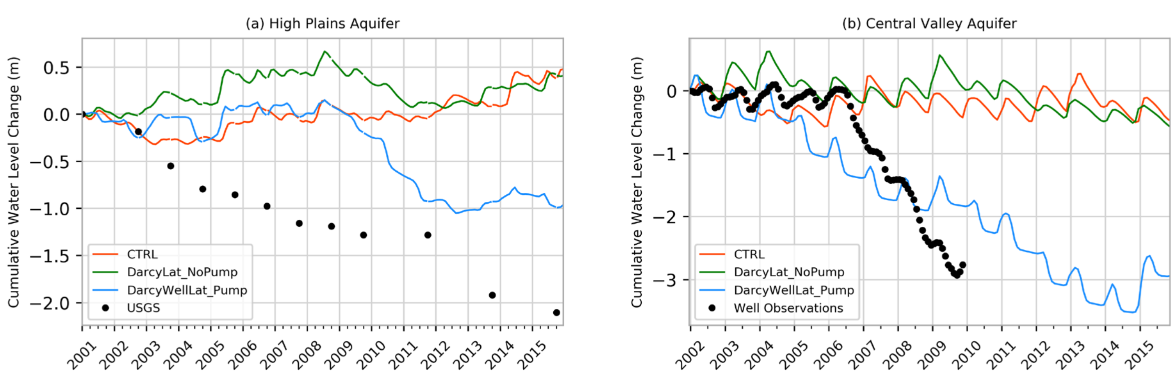

Figure 4-7. The cumulative time series of water level change from CLM5 simulations compared with the observations from the USGS reports across HPA and the well analysis in CVA.

Similarly in CVA (Figure 4-7b), the CTRL and DarcyLat_NoPump vary close to the zero line and do not show any depletion during the simulation period, while the monthly well analysis data start a sharp decline by 2007 and fells down ~3 m by the end of 2009. The DarcyWellLat_Pump simulation presents a much-improved groundwater dynamics, starts the decline two years earlier in 2005 with a gentler slope (i.e., compared to the well analysis) that reaches ~ 2 m depletion by the end of 2009, 1 m above the well observations.

To better investigate how large-scale pumping impacts the groundwater movement and flow regime, we calculate the lateral groundwater flow fields with and without pumping. For this purpose, the lateral fluxes from all eight neighboring cells are projected onto the coordinate axes, aggregated on the four edges of grid cells, and then averaged for both vertical and horizontal directions to get the north-south and east-west components at the center of the cell. These components are then used to show the mean lateral groundwater flow fields for 2000-2016 across CVA and HPA (Figure 4-8). While the lateral fluxes in the DarcyLat_NoPump simulation (Figure 4-8a,c) are controlled by the recharge (e.g., on the west border of HPA) and topography (e.g., southwest of CVA), extracting irrigation water from groundwater causes water table gradient which imposes large lateral influxes (i.e., up to 3.5 mm $month^{-1}$) towards the cones of depression in the two aquifers (Figure 4-8b,d). For example, the most depleted regions in central and southern HPA (Figure 4-5c) and southern CVA (Figure 4-6c) receive relatively large lateral flows, modulated by the estimated transmissivity, from the surrounding areas.

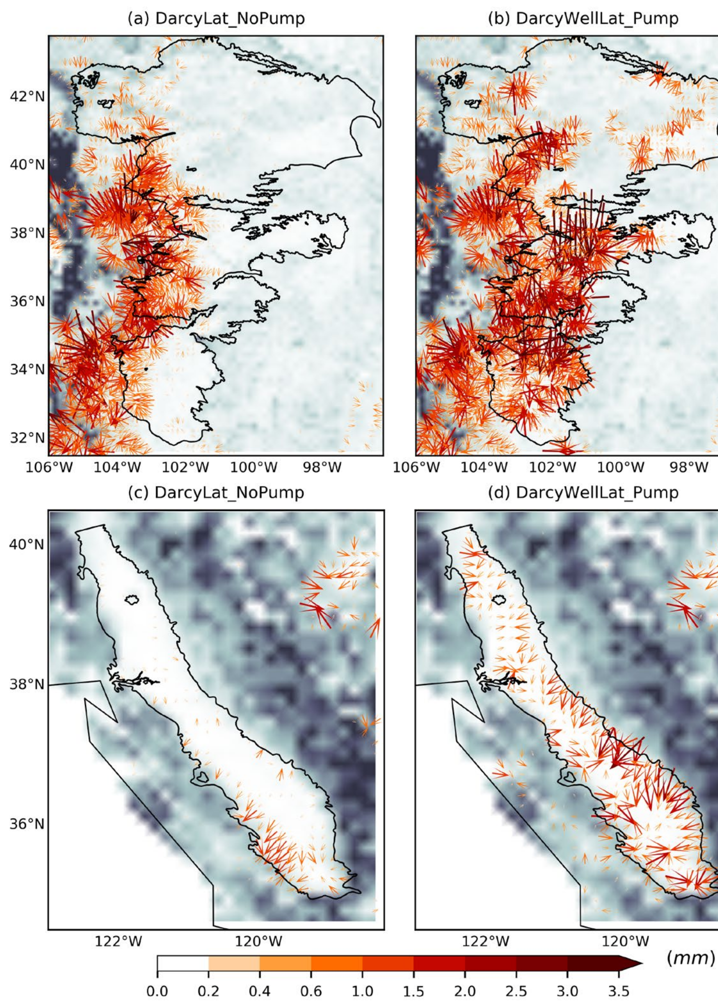

Figure 4-8. Mean lateral groundwater flow fields over HPA and CVA regions for 2000-2016. Background shows the shaded mean grid cell topographic slope where darker colors represent larger slopes.

4.3.3. Irrigation-induced Spatial Variations in TWS

Figure 4-9 shows the spatial variability of the TWS trends from the GRACE JPL mascon solution (a) and the CLM5 simulations (c-d) across the CONUS for 2002-2013. A coastline resolution improvement is applied to the GRACE solution used in this study, by multiplying GRACE data by a set of scaling factors to downscale the original GRACE resolution (i.e., ~3° ×3°) to 0.5° ×0.5° by redistributing the mass within each mascon in such a way that total mass in the block is conserved (Nie et al., 2018; Wiese et al., 2016). In general, GRACE data depict large negative TWS trends (i.e., ~1 to 4 cm year^{-1}) over CVA, southern HPA, the Coastal Lowlands Aquifer, and the Surficial Aquifer (Figure 4-9a). These areas mostly overlap with the irrigation hot spots, suggesting that irrigation plays a major role in modulating TWS in these regions. There are also large negative trends over non-irrigated areas detected by GRACE during 2002-2013, e.g., across the western Great Lakes region and small decreases in TWS over the eastern U.S. which are mainly driven naturally. Conversely, the GRACE captures large positive trends in TWS changes across the higher latitudes (i.e., above 40° N), specifically in the northern HPA region which is in line with the USGS groundwater depletion map that has shown groundwater rises in these highly irrigated regions (Figure 4-5d).

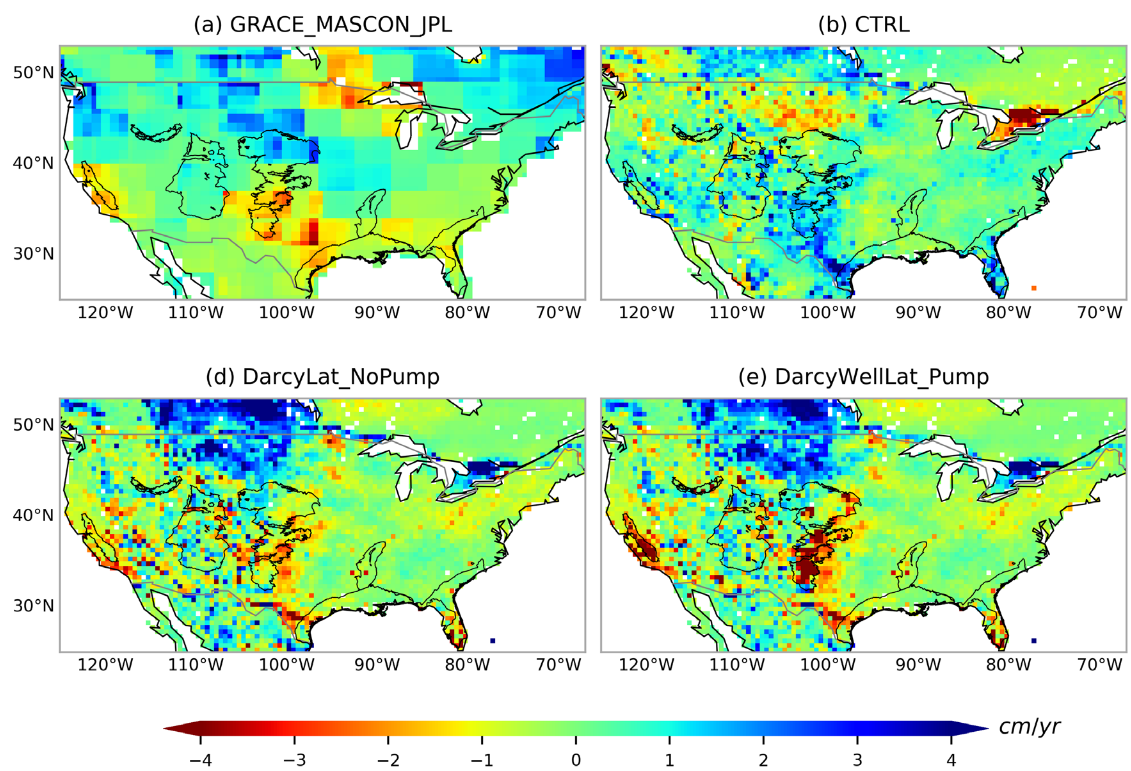

Figure 4-9. Spatial map of TWS trends (in cm year^{-1}) from GRACE JPL mascon solution and CLM5 simulations for 2002-2013. Scaling factors are multiplied by the GRACE mascon

Figure 4-9 (cont'd) solution. Trend maps from the CLM simulations are regridded to the $0.5° \times 0.5°$ grid to be consistent with the GRACE.

As discussed before in Section 4.2.6, the aquifer model with the head-based lower boundary condition in CLM is reported to generate unrealistic TWS response during the transitions between dry and wet years (Swenson & Lawrence, 2015). This poor response is also shown in the CTRL simulated trends (Figure 4-9b) where biases and false trends are clearly discerned, mostly across groundwater supplied irrigated regions, in comparison with GRACE. For example, the TWS trends simulated over the northern CVA, southern HPA, western Coastal Lowlands Aquifer, the Surficial Aquifer, and north-center of U.S. (e.g., North and South Dakota and Montana states) show completely opposite direction compared to the GRACE. In the DarcyLat_NoPump simulation (Figure 4-9c), the lateral flow mechanism substantially improves the trend values of most of these regions. Specifically, the increasing trend signals over central and southern HPA and west part of Coastal Lowlands Aquifer are changed to negative trends with the magnitudes and extends analogous to of the GRACE. Further, the large increasing TWS changes in the north-center of the U.S. is better captured in the DarcyLat_NoPump compared to the CTRL. Lastly, the DarcyWellLat_Pump resembles the DarcyLat_NoPump in most of the regions and to a large degree, except for areas with large groundwater-supplied irrigation where the DarcyWellLat_Pump shows large overestimation of TWS depletion rate due to groundwater pumping.

Table 4-2. Irrigation water withdrawals (total as well as broke down into groundwater and surface water sources) across HPA from the CLM5 simulations and USGS reports. The irrigation water requirement is also presented for all the simulations. Results for CTRL and DarcyLat_NoPump are presented only for years 2000 and 2005.

Year	USGS		Simulations				
	Irrigation Withdrawal	GW Source	Name	IWR*	Total Withdrawal	GW§ Source	SW¥ Source
2015	19.7	17.5	CTRL	-	-	-	-
			DarcyLat_NoPump	-	-	-	-
			DarcyWellLat_Pump	23.88	23.36	22.19	1.17
2010	19.8	16.8	CTRL	-	-	-	-
			DarcyLat_NoPump	-	-	-	-
			DarcyWellLat_Pump	32.54	31.67	29.75	1.92
2005	24.6	22.3	CTRL	21.56	10.09	0	10.09
			DarcyLat_NoPump	21.56	10.08	0	10.08
			DarcyWellLat_Pump	18.83	18.39	17.18	1.21
2000	26.5	23.6	CTRL	31.83	10.08	0	10.08
			DarcyLat_NoPump	31.83	10.07	0	10.07
			DarcyWellLat_Pump	29.30	28.47	26.79	1.68

* IWR: Irrigation water requirement

§ GW: Groundwater

¥ SW: Surface water

To explain the main driver behind the overestimation of the declining TWS by DarcyWellLat_Pump (i.e., relative to GRACE and other simulations), Table 4-2 compares the irrigation water requirement and withdrawals from groundwater and surface water sources in different simulations with the county-level data of irrigation water withdrawals from the USGS (Dieter et al., 2018; Maupin et al., 2014). The USGS census data records show that the irrigation water withdrawals in HPA ranges from 26.5 to 19.7 km^3 $year^{-1}$ during 2000-2015, of which more than 88% on average has been extracted from the groundwater (Table 4-2). In CLM5, the irrigation water requirement is applied to the soil column as add-on to the precipitation in the beginning of the time step and later (i.e., toward the end of the time step) is withdrawn from the surface water (i.e., water in the main channel in the MOSART river routing scheme) as the only source of irrigation by default. In the conditions where water in the river channel is not sufficient, the remaining irrigation water requirement is supplied by an imaginary source (e.g., ocean model). For example, while the total irrigation water requirement is estimated as 31.83 km^3 $year^{-1}$ in 2000 in both CTRL and DarcyLat_NoPump, only 32% of it is withdrawn from the surface water (Table 4-2). Whereas, in the DarcyWellLat_Pump simulation in the same year, 28.47 out of 29.30 km^3 $year^{-1}$ is extracted from both the groundwater (%94) and surface water (6%). Similar proportions exist in other years (Table 4-2). Therefore, it can be concluded that the net irrigation impact on TWS is positive in CLM5 default setting which is an unrealistic representation of irrigation and partly explains the increasing TWS changes over irrigated regions in Figure 4-9b. Overall, it still remains as an issue in hydrological modeling that where conjunctive use of groundwater and surface water for irrigation is implemented, substantial improvements are achieved in the simulation of groundwater dynamics and depletion but at the expense of overestimation of TWS trend compared to the GRACE observations. This overestimation is not only exclusive to the CLM and is reported in other studies that used other models (e.g., the HiGW-MAT, Noah-MP) to account for groundwater withdrawals for irrigation (Nie et al., 2018; Pokhrel et al., 2015).

4.3.4. River Discharge Simulation by MOSART

One of the major updates included in CLM5 is the inclusion of the MOSART river model which utilizes the kinematic wave method to simulate the channel velocity, water depth, and surface water dynamics (Lawrence et al., 2019). Here, we assess the impact of pumping on the river discharge simulated by the MOSART. It is expected that the differences in the simulation of groundwater table depth from CTRL, DarcyLat_NoPump, and DarcyWellLat_Pump would directly affect sub-surface runoff (see Section 4.2.6) used for surface water routing in MOSART, which is coupled with the CLM5, and that the impact of pumping is reflected in streamflow simulations. To evaluate these expectations, a validation of river discharge simulated by the MOSART is presented at the major USGS gauging stations across the U.S. (Figure 4-10). The statistical metrics (i.e., Nash-Sutcliffe efficiency coefficient and RMSE) are also presented for the seasonal river discharge.

Overall, a promisingly good agreement is found between the simulated river discharge and the USGS observations, specifically in the less managed basins as the current MOSART scheme in the CLM5 does not simulate reservoir inundation and operation. However, the differences between the three CLM simulations seem to be small, particularly in terms of the seasonal cycle. The main reason for such similarity is that the sub-surface runoff parameters (i.e., $q_{drai,max}$ and f_{drai}) are not specifically calibrated for these basins and therefore the parameterization is less sensitive to the groundwater table depth that is the main distinction between these three simulations.

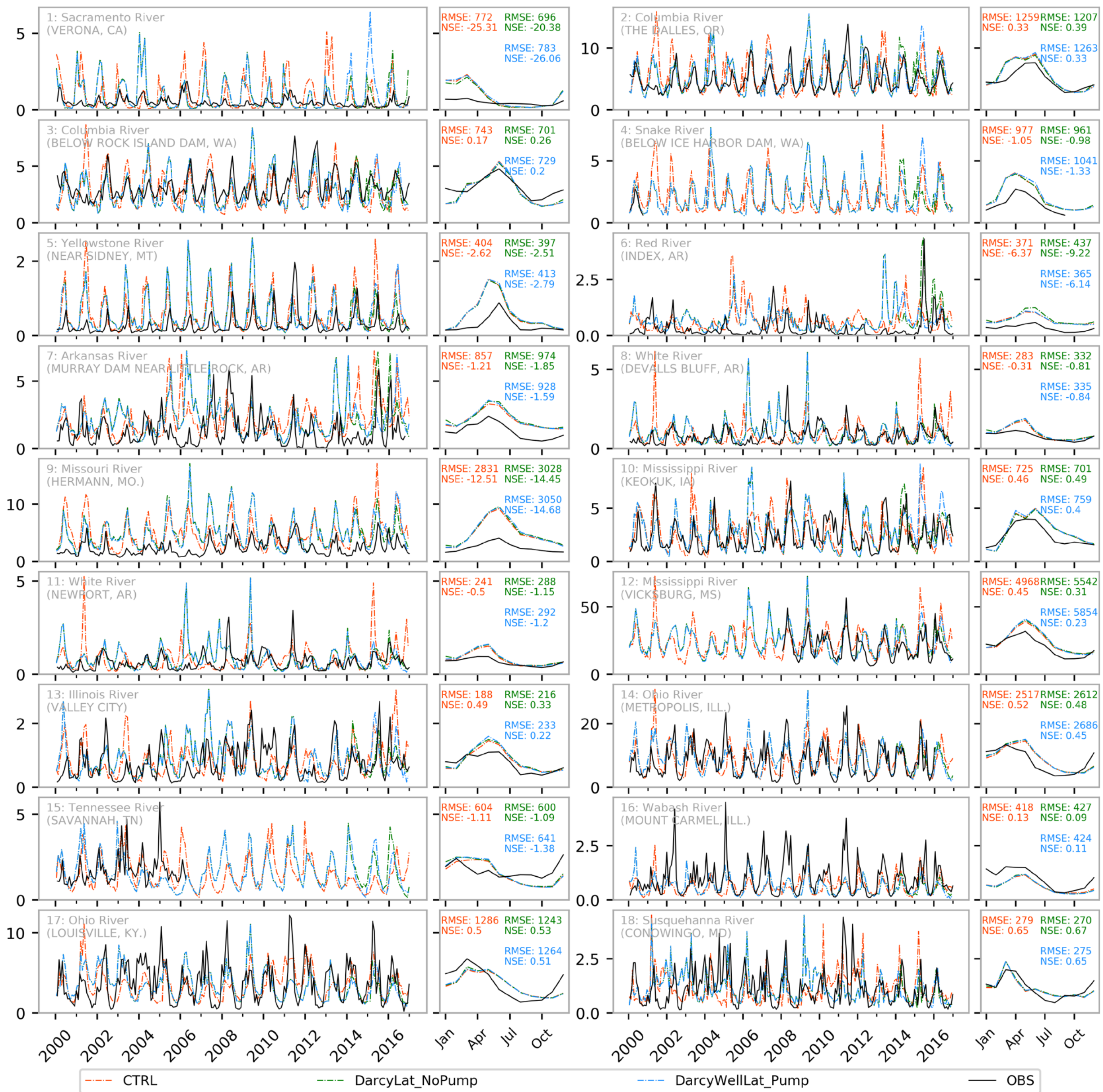

Figure 4-10. Comparison of simulated river discharge from the MOSART scheme and the USGS streamflow data at the major gauging stations across the U.S. Note that the unit is 10^3 m^3 s^{-1}.

In general, marginal improvements in simulation of seasonal cycle are found (e.g., Columbia River, Sacramento River, Yellowstone River, Mississippi River, Ohio River, and Susquehanna River) in the DarcyLat_NoPump simulation, however, the CTRL performs slightly better in some of the other basins/tributaries (e.g., Illinois River, White River). The entire time series also show a mixture of good and poor (e.g., false peaks and overestimation/underestimation) agreements with the USGS data in all simulations, making it difficult to rank them. It is expected that by calibrating the sub-surface runoff parameters and increasing the sensitivity to the water table (e.g., by reducing the decay factor f_{drai}), we see the direct impact of pumping on the river discharge and can better validate different simulations with the gauge data.

4.4. Conclusions

A prognostic groundwater model is implemented into the latest version of the CLM (CLM5) to enhance the simulation of groundwater dynamics and assess the impacts of extensive pumping on groundwater storage as well as the TWS changes with the focus on U.S. major aquifers. Three sets of CLM5 simulations are conducted at 5 km grids and over the CONUS to (1) evaluate the existing groundwater model of CLM5, (2) account for lateral groundwater flow based on Darcy's law, and (3) present the conjunctive use of groundwater and surface water for irrigation and introduce—for the first time—the parameterizations for an explicit representation of the steady-state well equation for the pumping grid cells. The results show that the new groundwater model (i.e., equipped with pumping from the aquifer storage and parameterized to account of the lateral flow based on Darcy's law and the well equation) significantly improves the simulation of groundwater level change and promisingly captures most of the hotspots of groundwater depletion across the overexploited HPA and CVA aquifers in U.S. Further, while the default CLM5 shows large biases and false TWS trends particularly over the highly irrigated regions (e.g., the central and southern HPA), the simulation with the lateral groundwater flow presents more accurate spatial patterns of TWS trends compared to the GRACE data. We find that unrealistic representation of irrigation source, i.e., the surface water as the only source in the default CLM5, leads to a failure in withdrawing irrigation water requirement from the river channels (i.e., due to the limited water availability during the irrigation season) and the majority of irrigation water demand is met by an imaginary source. Therefore, using the pumping scheme to replace the imaginary source of irrigation with groundwater eventuates in overestimation of declining TWS trend across the highly irrigated regions. There are several areas for future works to address the overestimation issue with the TWS trends. First, it is recommended to leverage the geological information of the new datasets of global aquifer properties such as the global permeability and depth to bedrock datasets to be utilized in the representation of lateral groundwater flow and pumping (e.g., in estimation of transmissivity). Second, testing different boundary conditions and soil configurations to improve the representation of groundwater are critically important and mentioned in the literature as well. Third, it is also essential to assess the uncertainties in the GRACE products in estimation of the TWS trends over the largely depleted regions.

CHAPTER 5

5. Global Terrestrial Water Storage Change under Climate Change and Implications on Global Mean Sea Level

In Preparation:

Pokhrel, Y., Felfelani, F. , Satoh, Y., Boulange, J., Burek, P., Gädeke, A., Gerten, D., Gosling, S., Grillakis, M., Gudmundsson, L., Hanasaki, N., Koutroulis, A., Liu, J., Papadimitriou, L., Schewe, J., Müller Schmied, H., Stacke, T., Eliza Telteu, C., Thiery, W., Veldkamp, T., Zhao, F., and Wada, Y., Global Terrestrial Water Storage and Drought Severity under Climate Change.

Felfelani, F., Pokhrel, Y., et al., Terrestrial Water Storage Contribution to Sea Level Rise under Climate Change.

5.1. Introduction

Recent advances in hydrological modeling in terms of the physics, parameterizations and structure in concert with the emerging indispensable satellite remote sensing data (e.g., data from GRACE and SMAP) have enabled an improved representation of terrestrial water storage (TWS) in models (Döll et al., 2014; Felfelani et al., 2018; Hanasaki et al., 2018; Pokhrel et al., 2015). TWS (i.e., the vertically integrated measure of water stored in aquifers, soil layers, wetlands, lakes and reservoirs, rivers, ice and snow, and canopies) is a critical component of the global water and energy budget and plays key roles in determining water resource availability (Rodell et al., 2018) and modulating water flux interactions between different Earth system components (Tapley et al., 2019).

Large number of studies have been used GRACE TWS data and model simulations for a wide range of applications, including the assessment of water resources and impacts of human activities (Döll et al., 2014; Felfelani et al., 2017; Pokhrel et al., 2017), quantifying groundwater losses (Döll et al., 2014; Famiglietti et al., 2011; Pokhrel et al., 2015; Rodell et al., 2009; Scanlon, Faunt, et al., 2012), drought monitoring (Chaudhari et al., 2019; Houborg et al., 2012; M. Zhao et al., 2017), assessing flood potential (Reager et al., 2014), and quantifying the global mean sea level (GMSL) changes (Reager et al., 2016; Wada et al., 2012). These studies have found inherent linkages between the TWS and critical hydrologic phenomena (e.g., drought, flood and GMSL change) and thus, have advanced our understanding of the big picture of global hydrologic systems (Famiglietti et al., 2015) under the influence of natural hydro-climatic variability and human land-water management activities. However, as presented in Chapter 2, the emphasis has been on historical variabilities in TWS. Crucially, there is a body of literature on the impacts of climate change on river discharge, evapotranspiration, and groundwater recharge (Oki & Kanae, 2006; Schewe et al., 2014), but no study has to date presented a comprehensive analysis of the potential impacts of future climate change on global TWS change and variabilities.

Recently, the Inter-Sectoral Impact Model Intercomparison Project, phase 2b (ISIMIP2b; https://www.isimip.org/) (Frieler et al., 2017; Warszawski et al., 2014) provided a framework for multi-model ensemble comparisons by bringing together 14 global impact models (out of which simulations of 7 global models are currently available) that are capable of simulating human activities (irrigation, water extraction, dams and reservoir operation, etc.) for the water sector. These multi-model and multi-GCM (general circulation model) simulations now provide TWS estimates for the historical and future periods, providing an opportunity to assess the TWS variability over the entire 21st century and thus examining the potential impact on drought severity and GMSL change.

Thus, we present a first global assessment of climate change impacts on TWS. We use multi-model hydrological simulations (27 ensemble members; Table 5-1) from the selected seven terrestrial hydrology models driven by atmospheric forcing from four global climate models (GCMs). We then examine the impacts of future climate-induced TWS change and variability on GMSL changes.

5.2. Methods

5.2.1. Models, Simulation Settings, Forcing Data

The seven terrestrial hydrology models used in this study include five global hydrological models (GHMs): CWatM (Burek et al., 2019), H08 (Hanasaki et al., 2008a, 2008b, 2018), MPI-HM (Stacke & Hagemann, 2012), PCR-GLOBWB (van Beek et al., 2011; Wada et al., 2010, 2014), and WaterGAP2 (Müller Schmied et al., 2016); one global land surface model (LSM): CLM4.5 (Oleson et al., 2013); and one dynamic global vegetation model (DGVM): LPJmL (Bondeau et al., 2007). All models simulate the key natural terrestrial hydrological processes (e.g., soil hydrology, vegetation, rivers) and the major human impacts on water resources. Meteorological data are derived from climate simulations by four of the global climate models (GCMs; a subset of models participating in the Coupled Model Intercomparison Project Phase 5; CMIP5) included in the Fifth Assessment Report (AR5) of the Intergovernmental Panel on Climate Change (IPCC), i.e., GFDL-ESM2M, HadGEM2-ES, IPSL-CM5A-LR, and MIROC5. The forcing data include the climate variables (precipitation, air temperature, short-wave and long-wave downwards solar radiation, wind speed, specific humidity, and surface pressure), are bias corrected (Lange, 2019), and downscaled to the same spatial resolution as that of the terrestrial hydrology models (i.e., 0.5°×0.5°). A comprehensive description of bias adjustment and downscaling can be found in the previous literature (Hempel et al., 2013; Lange, 2018, 2019).

For each GCM, four radiative forcing/climate scenarios are considered for varying periods: the pre-industrial control (PIC; pre-industrial climate; 1861-2099), historical climate (HIST; that includes effects of human emissions including greenhouse gases and aerosols; 1861-2005) (K. E. Taylor et al., 2011), strong mitigation climate scenario (Representative Concentration Pathway, RCP2.6; 2006-2099) which represents low greenhouse gas emission (i.e., CO_2 equivalent concentration of ~420 ppm by 2100), and no-mitigation climate scenario (RCP6.0; 2006-2099) which represents medium-high greenhouse gas emission (i.e., CO_2 equivalent concentration of ~740 ppm by 2100) (Table 5-1) (Miao et al., 2014). Simulations are conducted under the standard protocol of the Group-2 simulation scenario design of the ISIMIP2b. The two RCPs are the only RCPs for which TWS results were available from ISIMIP2b simulations. The hydrology models are run for each GCM-radiative forcing combination by considering time-varying human influences and socio-economic conditions for the PIC and HIST runs but fixed at the present day (i.e., 2005) levels for future projections (2006-2099; RCP2.6 and RCP6.0). There is only one exception (CLM4.5) that utilizes the fixed (i.e., at year 2005) socio-economic conditions for all PIC, HIST, and RCPs, which is allowed by the ISIMIP2b protocol. Human influences and socio-economic drivers considered are population, national gross domestic product (GDP), land use and land cover change (LULCC), irrigated areas, fertilizer use, and reservoir operation including water withdrawal, depending on the model schemes. The HYDE3-MIRCA data (Goldewijk et al., 2011; Portmann et al., 2010; Ramankutty et al., 2008) are used to prescribe LULCC and irrigated areas and the GRanD database (Lehner et al., 2011) is employed for dams and reservoirs implementation. Irrigation (and other water use sector) schemes vary among models but all models simulate global irrigation requirements within plausible limits of reported datasets based on country statistics (see reference to each model for more details). The reservoir operation schemes also vary among models; H08 and WaterGAP2 are based on the reservoir model in Hanasaki et al. (2006), LPLmL is based on Biemans et al. (2011), and CWatM and PCR-GLOBWB are based on a combination of Haddeland et al. (2006) and Adams et al. (2007). Note that reservoirs are not represented in MPI-HM and CLM4.5. Soil column depth and layer configuration and groundwater representation vary among models (see reference to each model).

Table 5-1. Summary of multi-model ensemble simulations. Note that the simulations from the MPI-HM model (forced by HADGEM2-ES GCM) are not available.

Radiative Forcing	**Preindustrial Control (PIC)**			**Historical (HIST)**		**RCP2.6**	**RCP6.0**
Period	**1861-2005**		**2006-2099**	**1861-2005**		**2006-2099**	
Socio-economic / **Terrestrial Hydrology Models**	**histsoc**	**2005soc**	**2005soc**	**histsoc**	**2005soc**	**2005soc**	**2005soc**
CLM4.5		GE, HE ICL, M5	GE, HE ICL, M5		GE, HE ICL, M5	GE, HE ICL, M5	GE, HE ICL, M5
CWatM	GE, HE ICL, M5		GE, HE ICL, M5	GE, HE ICL, M5		GE, HE ICL, M5	GE, HE ICL, M5
H08	GE, HE ICL, M5		GE, HE ICL, M5	GE, HE ICL, M5		GE, HE ICL, M5	GE, HE ICL, M5
LPJ-mL	GE, HE ICL, M5		GE, HE ICL, M5	GE, HE ICL, M5		GE, HE ICL, M5	GE, HE ICL, M5
MPI-HM	GE ICL, M5			GE ICL, M5		GE ICL, M5	GE ICL, M5
PCR-GLOBWB	GE, HE ICL, M5		GE, HE ICL, M5	GE, HE ICL, M5		GE, HE ICL, M5	GE, HE ICL, M5
WaterGAP2	GE, HE ICL, M5		GE, HE ICL, M5	GE, HE ICL, M5		GE, HE ICL, M5	GE, HE ICL, M5

GE: CFDL-ESM2M
HE: HADGEM2-ES
ICL: IPSL-CM5A-LR
M5: MIROC5

histsoc: time-varying, historical socio-economic scenarios
2005soc: socio-economic scenarios fixed at 2005 level

5.2.2. Multi-model Weighted Mean

Following the previous studies (Eyring et al., 2019; Sanderson et al., 2017), multi-model mean is calculated by weighting the ensemble members based on their skill (i.e., RMSE of the area-weighted seasonal cycle of TWS relative to GRACE data) and independence (i.e., a measure of how a model result differs from others, represented as the pairwise Euclidean distances between model results as well as model results and GRACE data) scores. The independence weight of member $i, w_u(i)$, is computed as the inverse of the summation of pairwise similarity score, $S(\delta_{i,j})$, which ranges between 1 (for identical members) and 0 (for the most distinct members):

$$w_u(i) = \frac{1}{1 + \sum_{j \neq 1}^{27} S(\delta_{i,j})} \tag{5-1}$$

The pairwise similarity score is calculated as a function of the Euclidean distance between the members ($\delta_{i,j}$), represented by the RMSE of the continent-level average TWS seasonal cycle from two members, and a parameter called the radius of similarity (D_u):

$$S(\delta_{i,j}) = exp\left(-\frac{\delta_{i,j}}{D_u}\right)^2 \tag{5-2}$$

where, $\delta_{i,j}$ is normalized by the mean of pairwise inter-model distances. The parameter D_u is the distance below which models are marked as similar and is resolved for each continent as a fraction of the distance between the best performing member (i.e., the model with the smallest RMSE) and GRACE through an iterative process (Sanderson et al., 2017). Figure 5-1 illustrates the continent-based pairwise inter-model distances ($\delta_{i,j}$ in Equation 5-2) for 27 ensemble simulations as well as GRACE data. Lower values (blue colors) of $\delta_{i,j}$ between two members (i and j) indicate high similarity between the seasonal cycle of TWS from members i and j, whereas larger values (red colors) which show low similarity.

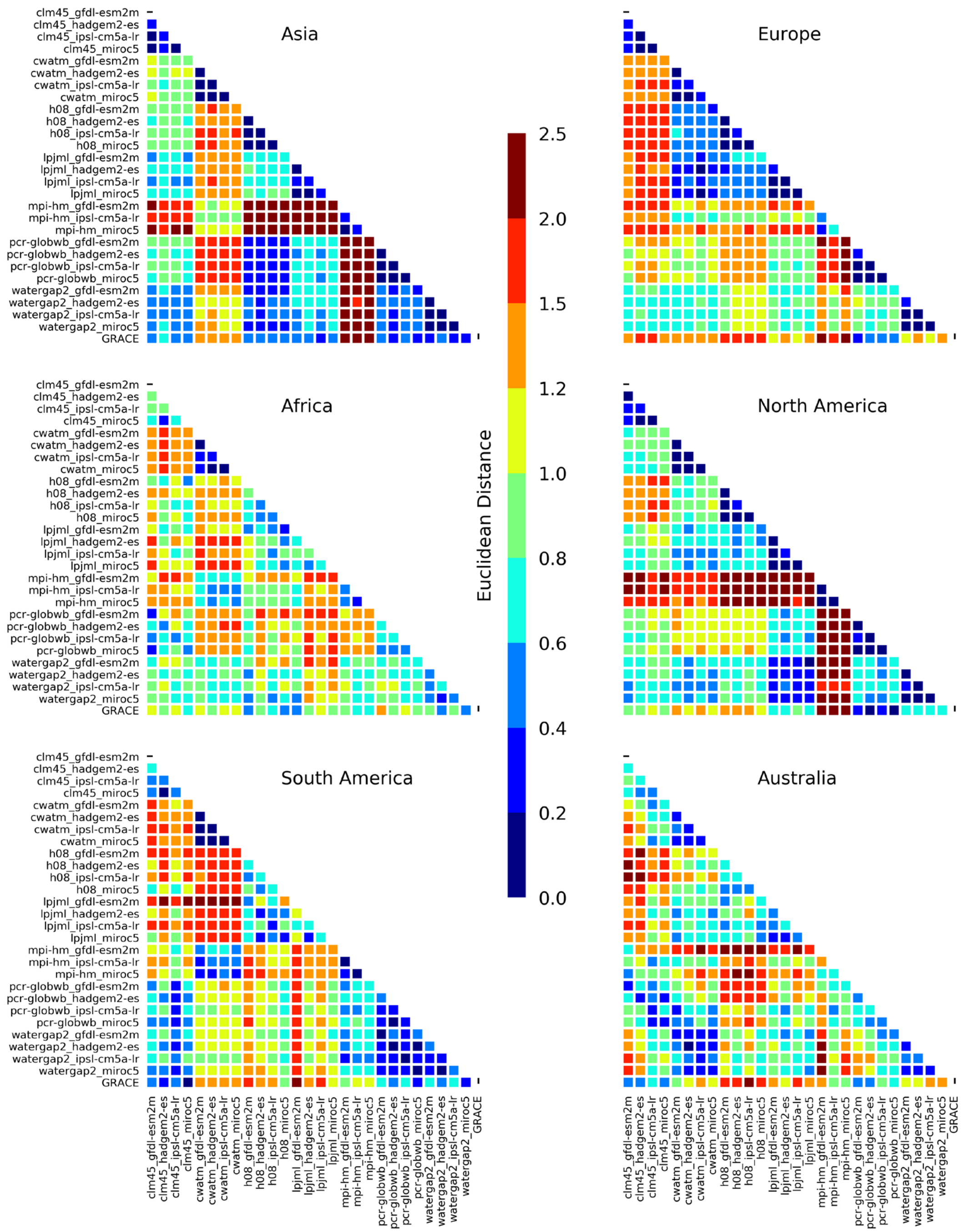

Figure 5-1. Continent-based pairwise inter-model distance matrix for all ensemble simulations and GRACE observations. Each row or column represents a single ensemble member or GRACE observations, and each cell represents a pairwise distance of that member compared to others. Distances are evaluated based on the root mean squared error (RMSE) of TWS seasonal cycle (calculated for 2002-2016 period by combining the results from HIST simulations with RCP2.6) spatially averaged over each domain (the continents).

The skill weighting of member $i, w_q(i)$, is calculated based on the stretched exponential function of the distance from GRACE ($\delta_{i,GRACE}$; the normalized RMSE of member i's TWS seasonal cycle against GRACE for 2002-2016) and the radius of model quality (D_q):

$$w_q(i) = exp\left(-\left(\frac{\delta_{i,GRACE}}{D_q}\right)^2\right) \quad (5\text{-}3)$$

where, smaller distances from the GRACE seasonal cycle result in larger skill score/weight. The parameter D_q is also defined as a fraction of the distance between the best performing member and GRACE. This parameter controls the strength of the skill weighting. That is, when D_q approaches zero, most of the simulations get significantly down-weighted and only the best performing model is assigned a high skill score. Conversely, as D_q approaches infinity, all ensemble members are allotted a high (i.e., close to 1) skill score alike and therefore, the multi-model weighted mean approaches the non-skilled weighted mean. Finally, the continent-based D_q values are estimated following a perfect model test and through an iterative procedure (Sanderson et al., 2017). The continent-based weights ($w_o(i)$) for the 27 ensemble members (Figure 5-2) are then calculated as the normalized product of the skill and independence weights so that their sum is unity (Eyring et al., 2019; Sanderson et al., 2017), i.e., $(\sum_{i=1}^{27} w_o(i) = 1)$. Results from the continent-based weights (Figure 5-2) show that there are relatively small differences between the weights assigned to a given terrestrial hydrology model forced by different GCMs.

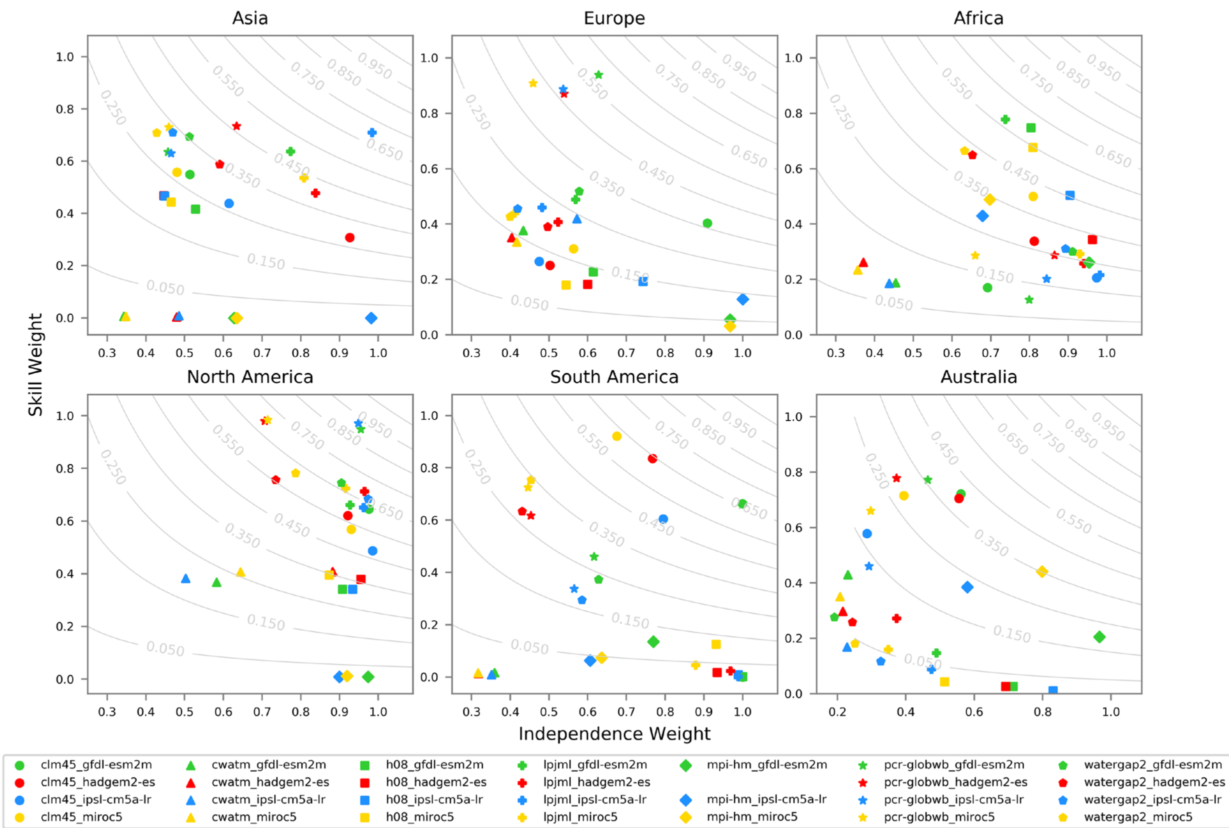

Figure 5-2. Continent-based model skill and independence weights (see Methods for details) for 27 ensemble members. CWatM and MPI-HM are given relatively lower overall weights compared to the other models.

5.2.3. Simulated TWS, GRACE data, Model Evaluation, and TWS Variability under Climate Change

To drive the monthly-scale simulated TWS, the surface and subsurface water storages, which include snow, canopy, river, reservoir (if simulated), lake (if simulated), wetland (if simulated), soil, and groundwater storages are vertically integrated in this study (Hirschi et al., 2006; Pokhrel et al., 2013). For all analyses presented, anomalies of TWS are used, not the absolute values. We use the GRACE TWS, the mean of mascon products from the CSR (Center for Space Research at University of Texas at Austin) (http://www2.csr.utexas.edu/grace/) and NASA's JPL (Jet Propulsion Laboratory) (https://podaac.jpl.nasa.gov/GRACE) processing centers (Scanlon et al., 2016), to evaluate the simulated TWS for the 2002-2016 period. For model results, since the evaluation period is not covered completely by HIST simulations, we combine the results from HIST simulations (2002-2005) with results from RCP2.6 (2006-2016). Note that the results from the RCP6.0 is highly analogous to RCP2.6 in the starting years. For the validation purpose, the seasonal mean of TWS anomalies (shown in Figure 5-4) is derived by first calculating the climatological mean seasonal cycle of TWS for the evaluation period and then taking the mean for each season. For consistency, the same reference period (2002-2016) is used in calculating the seasonal anomalies for both GRACE data and model simulations. Changes in TWS for the mid (2030-2059) and late (2070-2099) 21st century (for the two RCPs) are calculated by taking the difference of mean TWS for those periods to the mean TWS for the historical baseline period of 1976-2005, which is the last 30-year period of the historical simulations; simulations from year 2006 are conducted under future climate scenarios. For some of the analyses, sub-continental regions (Figure 5-3) defined by the IPCC Special Report On Extremes (SREX) are used to derive the mean seasonal cycle of TWS.

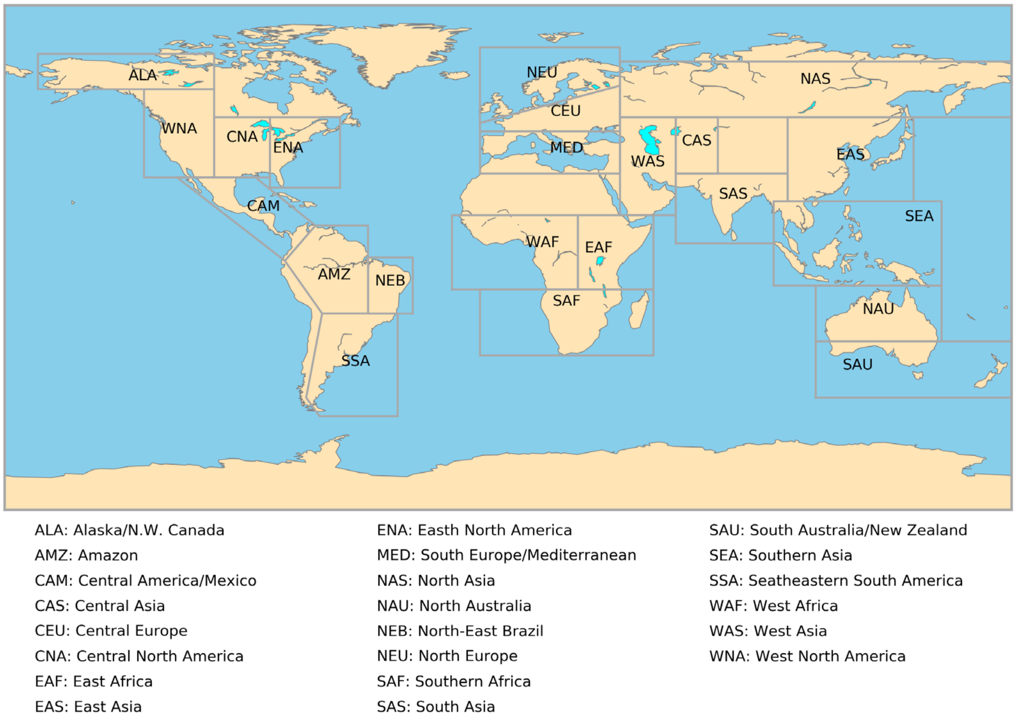

Figure 5-3. Geographic location and description of the selected sub-continental regions defined by the IPCC Special Report on Extremes (SREX).

5.3. Results and Discussion

5.3.1. Validation of Seasonal TWS

Figure 5-4 and Figure 5-5 show the validation of spatial seasonal TWS anomalies and monthly TWS seasonal cycles, respectively, against GRACE data—presented as the mean of mascon products from the two processing centers. Model results for the 2002-2005 period are taken from the historical simulations (see Table 5-1), and for 2006-2016 from RCP2.6 runs (with 2005soc socio-economic conditions). Anomalies are calculated by using the mean for 2002-2016 period for both model results and GRACE data. The results from RCP6.0 (not shown) are almost identical to that shown here. The broad global spatial patterns and seasonal variations in TWS are accurately captured by the weighted mean of multi-model ensemble, although some differences are evident in the magnitude of seasonal amplitude (e.g., across the Amazon basin that model tend to underestimate the amplitudes in DJF and MAM) (Figure 5-4). There are also differences stand out especially along major river channels that are explicitly considered in the models but not resolved in GRACE data. Further, the seasonal variations in the simulated TWS averaged over the major global river basins and presented as ensemble median, unweighted ensemble mean, and weighted ensemble mean are also in good agreement with GRACE data in most of the basins (Figure 5-5). It is evident that small differences exist between the ensemble median, unweighted ensemble mean, and weighted ensemble mean lines for 2002-2016, owing to the similarity of model results in the early years of 21st century.

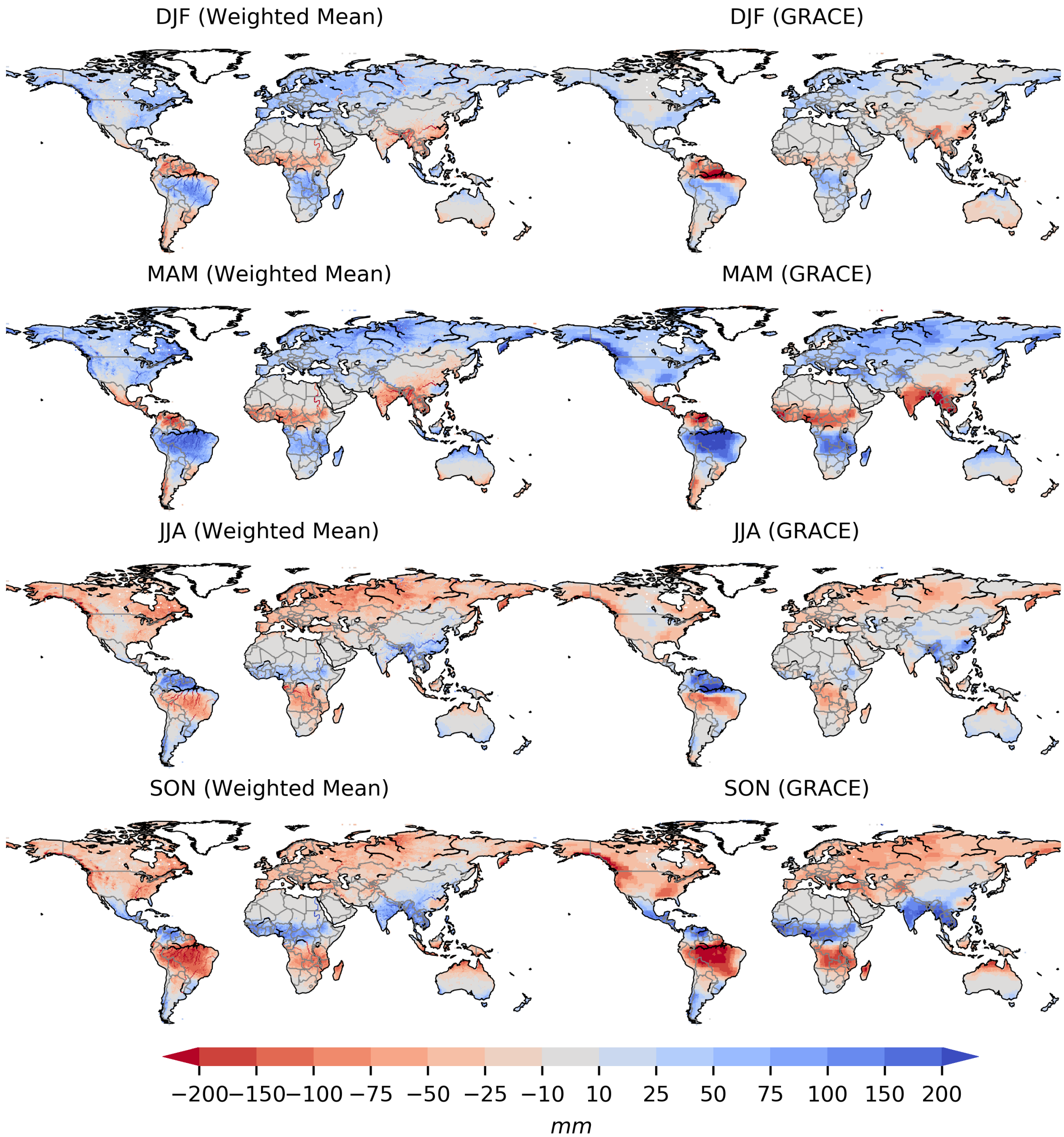

Figure 5-4. Spatial patterns of seasonal TWS anomalies from models and GRACE satellites. Shown here are the seasonal averages (December-February (DJF), March-May (MAM), June-August (JJA), and September-November (SON)) of the simulated (weighted ensemble mean) and GRACE-based monthly TWS deviation from the mean for the GRACE period (2002-2016).

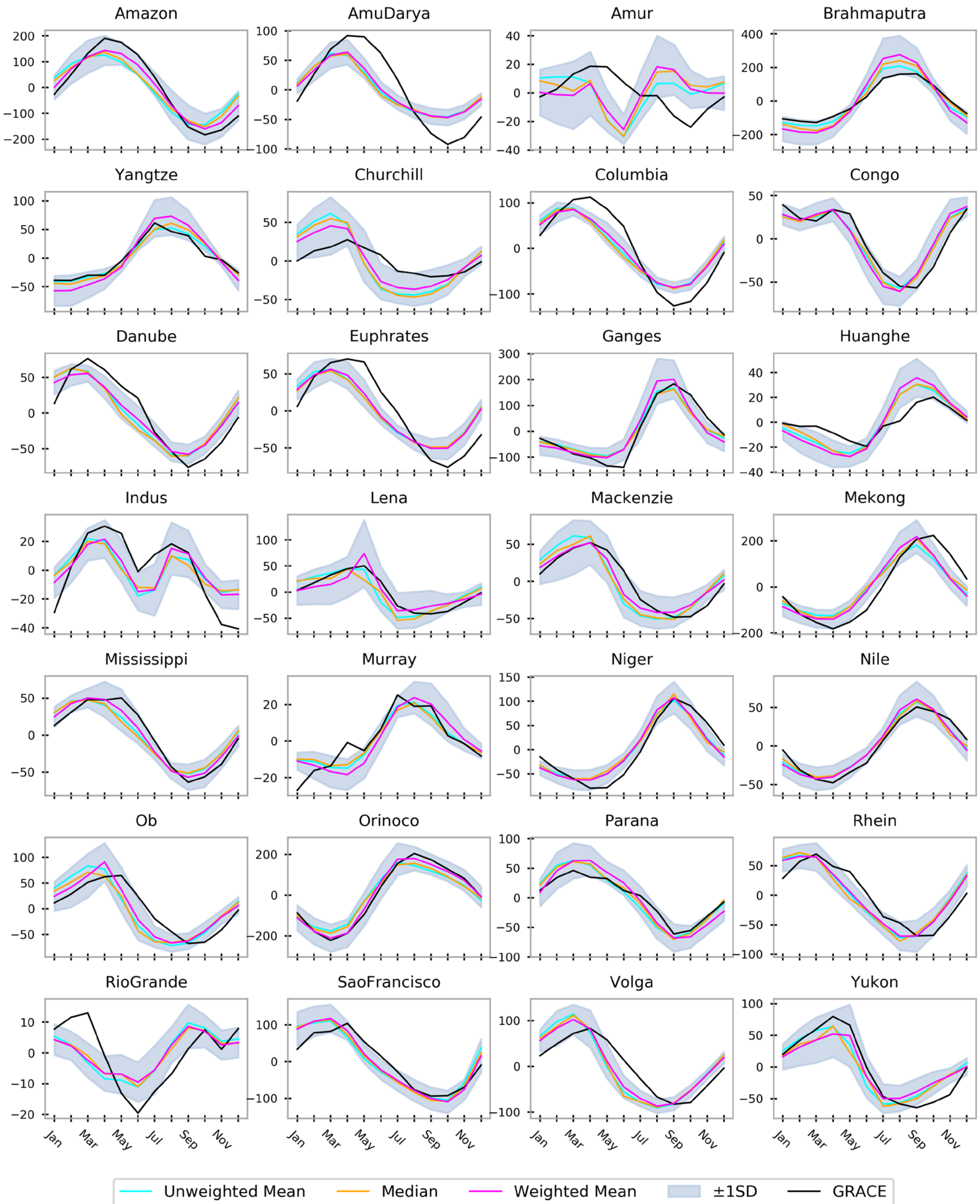

Figure 5-5. Monthly seasonal cycle (2002-2016) of TWS for the major global river basins. GRACE data are the mean of two mascon products (CSR and JPL; see Methods for more details). The light blue, pink, and orange lines show the unweighted mean, weighted mean, and median, respectively, of multi-model ensemble simulations. Gray shading indicates inter-model range expressed as one standard deviation (SD) from the weighted mean.

5.3.2. Impacts of Projected Climate Change on TWS

Figure 5-6 portrays the future changes in global TWS in mid- (2030-2059) and late-21st century (2070-2099) relative to the historical period (1976-2005) under the impacts of projected climate change based on RCP2.6 and RCP6.0 scenarios. To better identify the main drivers of TWS changes, similar spatial maps are shown for projected precipitation (Figure 5-7) and temperature (Figure 5-8) for the same periods and from the same climate scenarios and GCMs of CMIP5. TWS is projected to decline by the mid- and late-21st century in the majority of the southern hemisphere (e.g., the Amazon basin, parts of central Africa, and Australia), the conterminous U.S. (CONUS), most of Europe, and the Mediterranean, but is projected to increase in eastern Africa, south Asia, and a large portion of northern high latitudes, especially northern Asia (Figure 5-6). Consistent with the changes in precipitation (Figure 5-7), results indicate a strong north-south contrast in TWS change, readily discernible in the latitudinal mean (Figure 5-6). While the aforementioned changes are evident by the mid-21st century (under both RCPs; Figure 5-6a,c), the signals become even stronger by the late-century, and especially under RCP6.0 (Figure 5-6d). There are also exceptions, e.g., parts of Midwest and eastern CONUS where TWS under RCP2.6 is projected to decline by the mid-century but then increases or shows no significant change during the late-century, primarily due to the projected increase in precipitation (Figure 5-7) but decrease in temperature (Figure 5-8) under RCP2.6 and from mid- to late-century. For RCP6.0 and across most global regions, the projected changes (positive or negative) seen in the mid-century become more pronounced in the late-century. Next, the comparison of the RCPs for both periods reveals that the differences between the two RCPs are less obvious; an exception is in Australia where results indicate a smaller decline in TWS under RCP6.0 than under RCP2.6

(Figure 5-6), which again is consistent with the patterns of changes in precipitation where RCP2.6 projects a drier climate for Australia than RCP6.0 for both mid- and late-century (Figure 5-7).

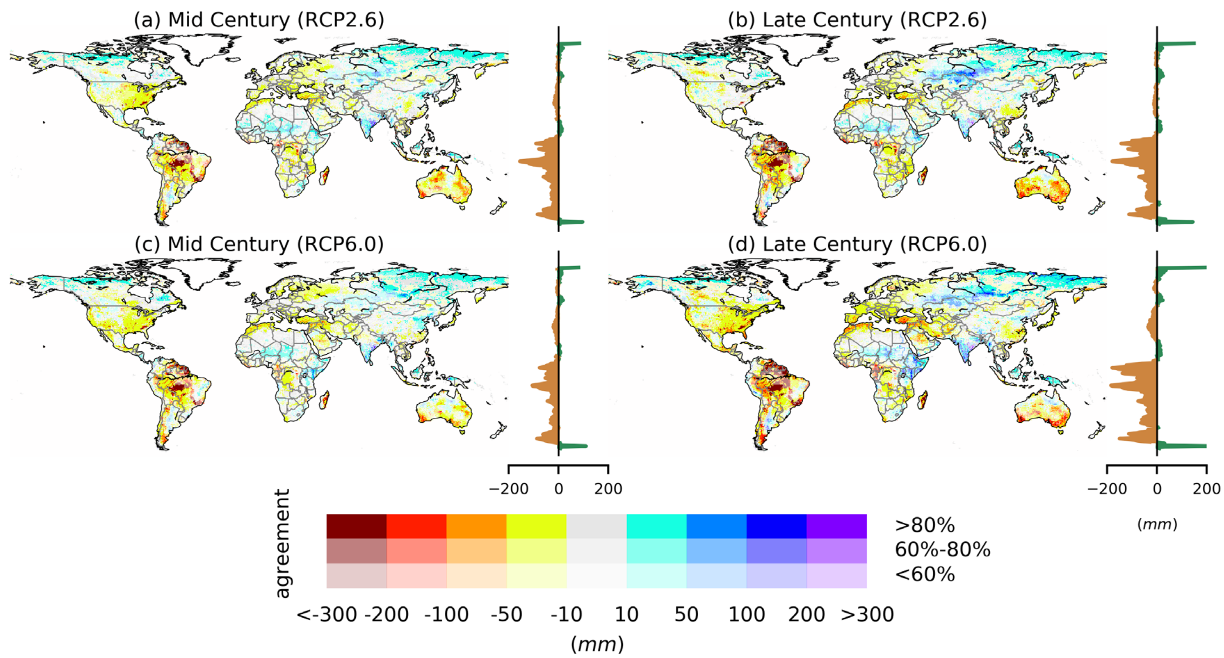

Figure 5-6. Impact of climate change on TWS. Shown are the changes (multi-model weighted mean) in TWS averaged for the mid (2031-2059; a and c) and late (2070-2099; b and d) 21st century under RCP2.6 (a and b) and RCP6.0 (c and d) relative to the average for the historical baseline period (1976-2005). Color hues show the magnitude of change and saturation indicates the agreement, among ensemble members, on the sign of change. The graph on the right of each panel shows the latitudinal mean.

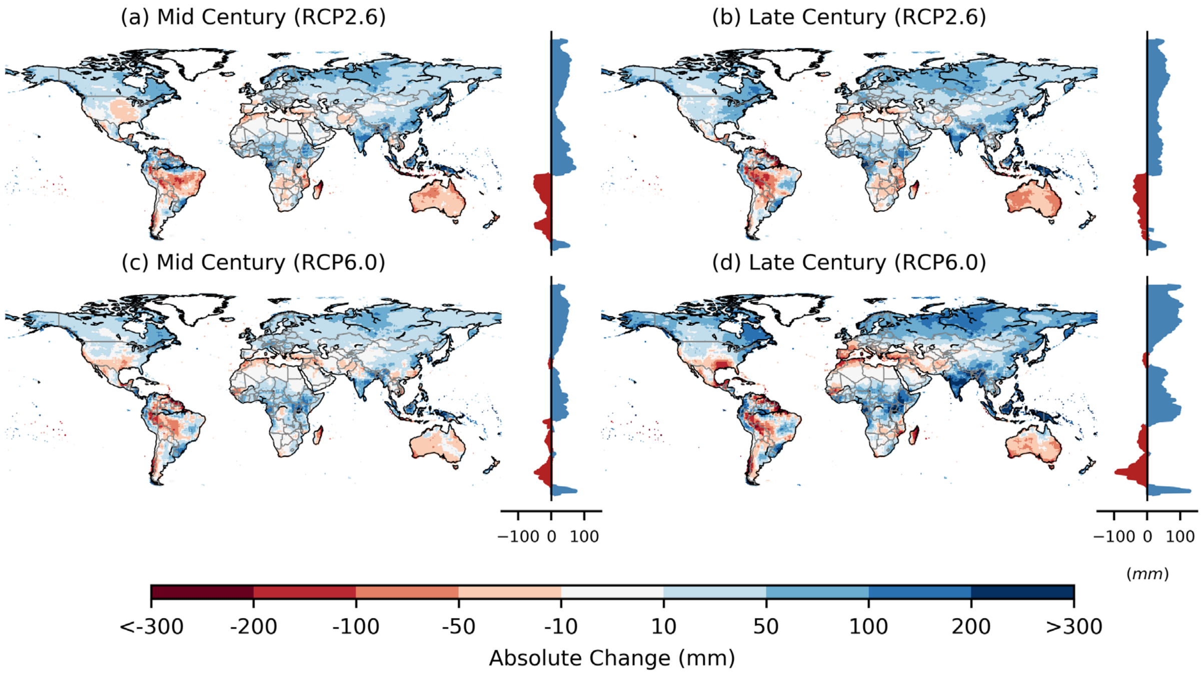

Figure 5-7. Spatial patterns of change in precipitation by the mid (2030-2059) and late (2070-2099) 21st century under RCP2.6 and 6.0. Shown are the absolute differences in the annual mean between the two future periods and historical baseline period of 1976-2005, calculated as the mean of the results from four Global Climate Models (GCMs) used to drive the hydrological models: HadGEM2-ES, GFDL-ESM2M, IPSL-CM5A-LR, and MIROC5. Note that Greenland is masked out. The graph on the right of each panel shows the latitudinal mean.

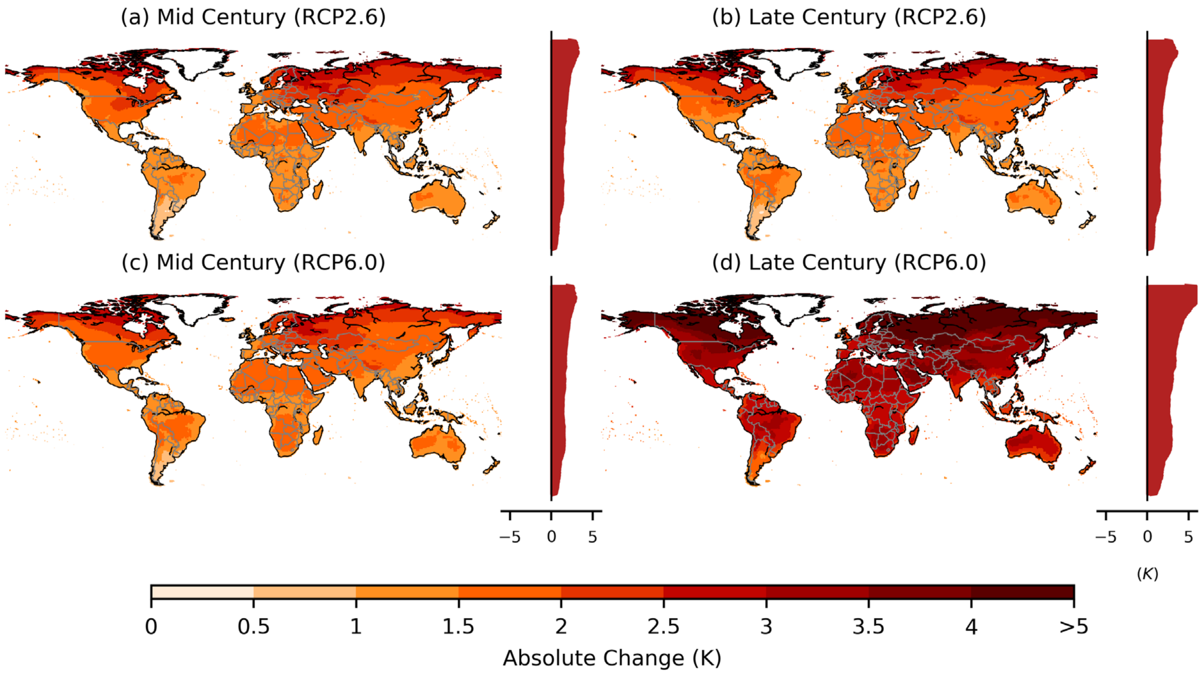

Figure 5-8. Same as in Supplementary Figure 5-7 but for annual mean temperature (in Kelvin).

Overall, color saturation in Figure 5-6 shows that a strong agreement exists across ensemble members in the sign of change for most regions, indicating high confidence in the model projections. For example, the TWS decline in most of the Amazon basin, Australia, and the CONUS as well as the TWS increase in northern Asia are agreed among more than 80% of the ensemble members. The confidence in model projections is further reinforced by a strong agreement between the simulated TWS seasonal cycle and GRACE data for the historical period discussed above (Figure 5-4 and Figure 5-5).

Figure 5-9 shows the weighted mean of TWS seasonal cycles for the SREX regions based on the TWS anomalies, generated by combining the results from HIST simulations with the corresponding RCP. Anomalies are calculated considering the reference period set to 1861-2099 to avoid potential exaggerations in the estimates of TWS variabilities (Sippel et al., 2015).

Projected changes in TWS seasonal cycle vary across regions (Figure 5-9). Regions (Figure 5-3) including the Amazon, Mediterranean, North Australia (NAU), Northeast Brazil (NEB), South Australia (SAU), Southeastern South America (SSA), and West Africa (WAF) are projected to experience a substantial downward shift in the seasonal cycle caused by declining TWS, whereas East Africa (EAF), North Asia (NAS), and South Asia (SAS) will experience an upward shift in the seasonal cycle, reflecting a large increase in TWS compared to the baseline period. Many of the regions with increasing TWS overlap with regions with marked increase in precipitation (Figure 5-7). Further, our findings here corroborate discoveries of previous studies; two examples are: the strong drying in the Mediterranean which is consistent with the historically-observed north (wet)-south (dry) contrast in pan-European river flows (Gudmundsson et al., 2017) and the TWS deficit in the Amazon basin which is in line with the reported substantial decline in water table depth and sub-surface water storage under future climate (Pokhrel et al., 2014).

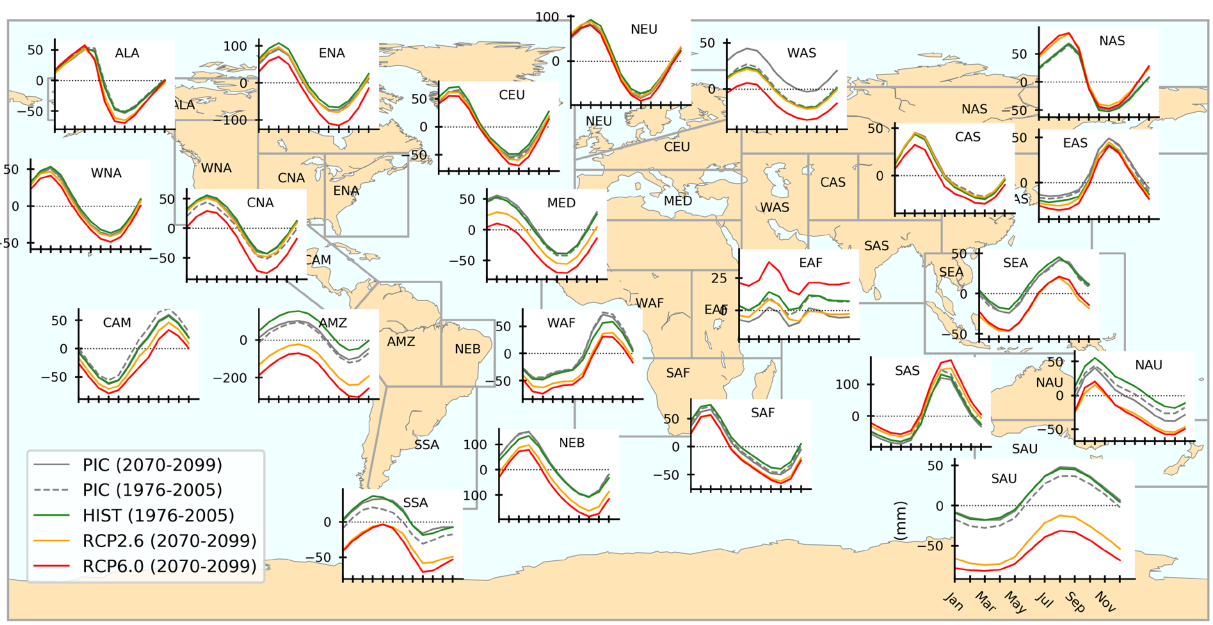

Figure 5-9. Seasonal TWS variations for sub-continental regions defined by the IPCC Special Report On Extremes (SREX). Ensemble weighted mean seasonal cycle is estimated

Figure 5-9 (cont'd) from the time series of TWS for the respective periods (see legends). X-axis labels are shown in the plot for SAU. A description of the SREX regions is provided in Figure 5-3.

The comparison of the HIST and RCPs simulations with the PIC simulation suggests that the projected changes in TWS for the past and late-21st century (Figure 5-9) are driven primarily by changes in climate forcing, as opposed to changes in land-water management and/or socio-economic drivers. Since the PIC simulations use identical socio-economic scenarios as the HIST and RCP simulations for the respective periods (Table 5-1), the comparison reveals that TWS would have remained generally stable in most regions under a preindustrial climate.

5.3.3. Implications of Projected Changes in TWS on Sea Level

The IPCC reported the rate of GMSL rise to be ~1.7$\pm$0.2 mm year^{-1} during 1901-2010, however, largely increased to ~3.2$\pm$0.4 mm year^{-1} toward the end of the period (i.e., 1993-2010). The emergence of GRACE era with monthly observations of Earth's gravity field has enabled us to better estimate the total GMSL changes as well as the components' contributions. The total GMSL budget (i.e., ~2.74 to 3.2 mm year^{-1}) is then broken down into the major components, i.e., the thermal/steric expansion of oceans (~1.38 mm year^{-1}), ablation of Greenland (~0.73 to 0.77 mm year^{-1}), Antarctica (~0.26 to 0.49 mm year^{-1}), and land glaciers (~0.38 to 0.65 mm year^{-1}), and the terrestrial hydrology contribution (~- 0.29 to - 0.33 mm year^{-1}) (Reager et al., 2016; Rietbroek et al., 2016). While the human-induced TWS declines/changes have been proved to contribute to GMSL rise with the rate of 0.31 to 0.69 mm year^{-1} (Table 5-2) (Pokhrel, Hanasaki, Yeh, et al., 2012; Wada et al., 2012), large climate-driven TWS changes have slowed the GMSL rise with the rate of 0.71 mm year^{-1} and thus, resulting in a net GMSL decrease (i.e., ~- 0.29 to - 0.33 mm year^{-}

^{1}) caused by the terrestrial hydrology (i.e., excluding the land glaciers and ice sheets) (Reager et al., 2016).

Table 5-2. The comparison of estimated contribution of terrestrial hydrology to GMSL rise from different studies and the projected values of this studies.

			Land Hydrology Contribution to GMSL rise		
Study	**Method**	**Time Period**	**Glaciers**	**Human-induced TWS**	**Climate-driven TWS**
Llovel et al. (2010)	GRACE	2002-2009		-0.22	
Konikow et al. (2011)	In situ Obs.	2000-2008		0.41 ± 0.10	
Wada et al. (2012)	PCR-GLOBWB Model	2000		0.57 ± 0.09	
Pokhrel et al. (2012)	HiGW-MAT Model	1961-2003		0.69	0.08
IPCC AR5 (2013)	Previous Studies	1993-2010		0.38 ± 0.12	
Döll et al. (2014)	WaterGAP Model	2000-2009		0.31 ± 0.0	
Richey et al. (2015)	GRACE	2003-2014		0.24 ± 0.02	
Rietbroek et al. (2016)	GRACE	2003-2014	0.38 ± 0.07	-0.29 ± 0.26	
Reager et al. (2016)	GRACE	2002-2014	0.65 ± 0.09	0.38 ± 0.12	-0.71 ± 0.20
This Study	TWS Projection (RCP2.6)	2030-2059		0.07 ± 0.027	
This Study	TWS Projection (RCP6.0)	2030-2059		0.18 ± 0.024	
This Study	TWS Projection (RCP2.6)	2070-2099		0.08 ± 0.024	
This Study	TWS Projection (RCP6.0)	2070-2099		0.07 ± 0.016	

Figure 5-10 shows the weighted mean of annual land water storage variation expressed as the equivalent sea level with monthly climatology removed for 1861-2099 (i.e., after the results form HIST and corresponding RCP are combined) and land glaciers and ice sheets excluded. The results show that the global land, excluding glaciers, gains water (i.e., ocean loses) during 2002-2014 consistent with previous studies (e.g., Llovel et al. 2010; Reager et al. 2016). However, the TWS trend values (i.e., 0.01 ± 0.08 mm year^{-1} for RCP2.6 and 0.1 ± 0.10 for mm year^{-1} for RCP6.0) are underestimated compared to the GRACE measurements, in line with the findings of Scanlon et al. (2018) that many of the global models tend to underestimate large decadal rising and declining TWS trends.

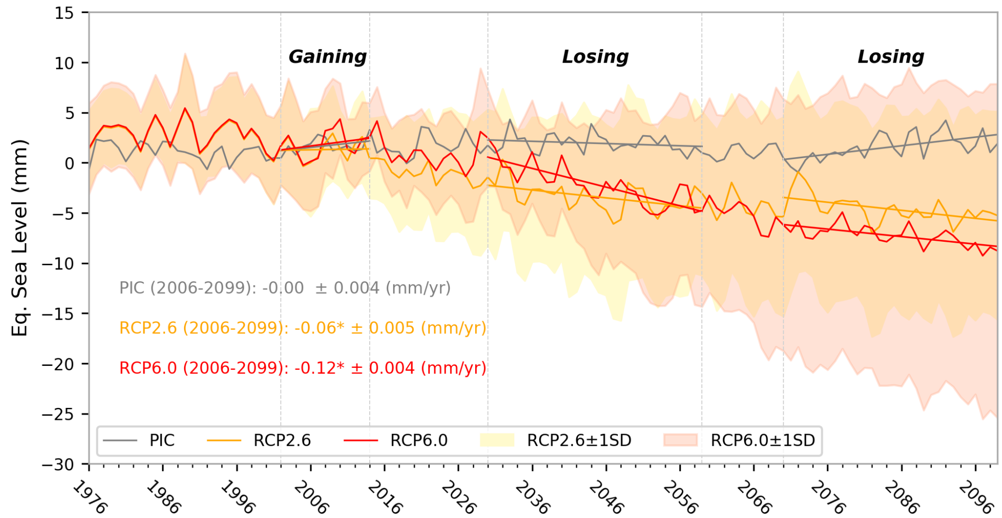

Figure 5-10. Simulation of land water storage changes, expressed as equivalent sea level changes, for 1976-2099. Ensemble weighted mean of TWS changes, grouped by climate scenarios, is shown as solid lines and the shaded areas indicate the ∓1 standard deviation (SD) from the weighted mean.

Starting from 2016 and continued in the mid (2030-2059) and late (2070-2099) 21st century, land water storage is projected to shift from gaining to losing water (i.e., ocean gaining) (Figure 5-10). Therefore, the role of the terrestrial hydrology, as a component that has decelerated the GMSL rise in the past decade, is projected to be reversed by the mid- and late-21st century. The rates of TWS changes are estimated as - 0.07±0.03 and - 0.18±0.02 mm year^{-1} based on RCP2.6 and RCP6.0 scenarios, respectively, for the mid-century and - 0.08±0.02 and - 0.07±0.02 mm year^{-1} based on RCP2.6 and RCP6.0 scenarios, respectively, for the late-century (Table 5-2). These rates are statistically significant (i.e., $p < 0.05$) based on the Wald test.

5.4. Conclusions

In summary, the impacts of climate change on global TWS variations and the implications on GMSL change are quantified by using multi-model ensemble global simulations from seven global terrestrial hydrology models (i.e., CLM4.5, CWatM, H08, LPJmL, MPI-HM, PCR-

GLOBWB, and WaterGAP) input by the forcing data of four GCMs (i.e., GFDL-esm2, HadGEM2-ES, IPSL-CM5-LR, and MIROC5). Four cases of radiative forcing are considered for each GCM: the pre-industrial control, historical climate, and the low (RCP2.6) and medium-high (RCP6.0) greenhouse gas concentration scenarios. Simulations are conducted under the framework of the ISIMIP2b. Results are indicated as multi-model weighted mean of TWS anomalies calculated by scoring the ensemble members based on their continent-level skill and independence weights. The results from the climate-induced TWS changes show that an overall north-south contrast exists, where TWS is projected to increase in northern high latitudes, south Asia, and eastern Africa, but to decrease in other regions including the Amazon, U.S., Australia, southern Europe and the Mediterranean, and southwestern Africa. There is a strong agreement among ensemble model projections suggesting that the findings are robust. We further find that the critical role of global TWS as a component that has decelerated the GMSL rise is projected to be reversed (i.e., contributing to the GMSL rise) by the mid- and late-21st century. Our results have important implications for improved assessment of climate impacts on land water resources and future GMSL changes.

CHAPTER 6

6. Summary and Conclusions

Land surface models (LSMs) are designed to be coupled with atmospheric/climate and ocean models within the framework of Earth system models (ESMs), providing the opportunity to simulate various hydrological, biogeochemical, and biogeophysical processes on land as the feedback and interactions among various Earth system components (e.g., atmosphere and oceans). Despite noteworthy progress that has been made in incorporating human footprints on global hydrology in LSMs, limitations and significant challenges still remain in representation of human impacts, particularly irrigation and groundwater extraction, which lead to failure in accurately capturing the process heterogeneities on and below the land surface and the fine-scale details of land-water management practices. Therefore, the overarching goal of my Ph.D. dissertation is to improve the irrigation and groundwater parameterizations in LSMs toward advancing our understanding of hydrology-human-climate interactions.

In Chapter 2, two state-of-the-art models (i.e., HiGW-MAT and PCR-GLOBWB) together with multiple GRACE spherical harmonic (SH) products are used to quantify the impacts of human activities on terrestrial water storage (TWS) change. Overall, the results from the TWS simulations show that a good agreement can be seen between GRACE and both HiGW-MAT and PCR-GLOBWB models in terms of the direction and magnitude of change. However, a relatively poor agreement exists between the models and GRACE over the highly-managed and snow-dominated regions, highlighting the need to improve model parameterizations for the simulation of human water management and snow physics to reliably simulate the spatial and temporal variability in TWS.

In Chapter 3, a new approach is presented to improve irrigation representation in global LSMs by assimilating soil moisture (SM) from SMAP satellite. This approach includes the derivation of vertical soil moisture profile from SMAP data and assimilation using 1-D Kalman Filter smoother to improve the representation of target soil moisture. SMAP SM data are also bias corrected using ground-based soil moisture data in one of the simulations. The approach is tested over the highly irrigated region in the central U.S. at 3 arc-minute spatial resolution in CLM4.5. The results show that significant improvements in irrigation simulations can be achieved through 1-D Kalman Filter data assimilation. Thus, while the present study is conducted at the regional scale using CLM4.5, the newly developed approach can be incorporated into any LSM and applied globally.

In Chapter 4, a prognostic groundwater model, equipped with lateral groundwater flow, conjunctive water use for irrigation, and pumping, is implemented in the latest version of CLM (CLM5) to investigate the role of lateral groundwater flow and impacts of pumping on simulation of continental-level groundwater and TWS. Specifically, an explicit parameterization for the steady-state well equation is introduced—for the first time—in the global land surface modeling. The new groundwater model with pumping is shown to promisingly simulate groundwater depletions across the two heavily irrigated aquifers in the U.S. Further, results show that large biases and false TWS trend values simulated by the default CLM5 are significantly corrected when adding the lateral groundwater flow based on Darcy's law. We find that unrealistic representation of irrigation source, i.e., withdrawing from the surface water as the only source in the default

CLM5, leads to a large water deficit in satisfying the irrigation water requirement due to the limited water availability during the irrigation season. Therefore, the majority (i.e., ~two third) of irrigation water is coming from an imaginary source, causing false wet biases in simulated TWS trend across irrigation regions. When the pumping scheme is activated to account for conjunctive water use for irrigation, the majority of the irrigation water requirement is supplied by real groundwater and surface water sources, however, the declining TWS trends are mostly overestimated. Future studies need to address this overestimation issue by including more geological information in the representation of lateral groundwater flow and pumping.

In Chapter 5, multi-model ensemble global simulations of projected TWS are used to investigate the impacts of climate change on global TWS and to quantify the consequent implications on the global mean sea level (GMSL) change. Seven global terrestrial hydrology models (i.e., CLM4.5, CWatM, H08, LPJmL, MPI-HM, PCR-GLOBWB, and WaterGAP) input by the forcing data from four general circulation models (GCMs; i.e., GFDL-esm2, Had-GEM2-ES, IPSL-CM5-LR, and MIROC5) under four cases of radiative forcing: the pre-industrial control, historical climate, and the low and medium-high greenhouse gas concentration scenarios (i.e., RCP2.6 and RCP6.0, respectively) are utilized in the analyses. Results indicate that major global hotspots of TWS deficit are mostly located in the southern hemisphere (e.g., the Amazon, Australia, and southwestern Africa), while the northern high latitudes, south Asia, and eastern Africa are projected to experience TWS increases by the mid- and late-21st century. We further find that the global TWS as a critical component of the GMSL budget is projected to shift from decelerating (i.e., in the past several decades) to accelerating the GMSL rise by the mid- and late-21st century.

REFERENCES

REFERENCES

Abramopoulos, F., Rosenzweig, C., & Choudhury, B. (1988). Improved Ground Hydrology Calculations for Global Climate Models (GCMs): Soil Water Movement and Evapotranspiration. *Journal of Climate*, *1*(9), 921–941. https://doi.org/10.1175/1520-0442(1988)001<0921:IGHCFG>2.0.CO;2

Adam, J. C., Haddeland, I., Su, F., & Lettenmaier, D. P. (2007). Simulation of reservoir influences on annual and seasonal streamflow changes for the Lena, Yenisei, and Ob' rivers. *Journal of Geophysical Research: Atmospheres*, *112*(D24). https://doi.org/10.1029/2007JD008525

Akin, E. (2003). *Object-Oriented Programming Via Fortran 90/95*. Cambridge University Press.

Albergel, C., Rüdiger, C., Pellarin, T., Calvet, J.-C., Fritz, N., Froissard, F., et al. (2008). From near-surface to root-zone soil moisture using an exponential filter: an assessment of the method based on in-situ observations and model simulations. *Hydrol. Earth Syst. Sci.*, *12*(6), 1323–1337. https://doi.org/10.5194/hess-12-1323-2008

Alcamo, J., Döll, P., Kaspar, F., & Siebert, S. (1997). Global change and global scenarios of water use and availability: an application of WaterGAP 1.0. *Centre for Environmental Systems Research, University of Kassel, Germany*, (Report A9701).

Alcamo, J., Döll, P., Henrichs, T., Kaspar, F., Lehner, B., Rösch, T., & Siebert, S. (2003). Development and testing of the WaterGAP 2 global model of water use and availability. *Hydrological Sciences Journal*, *48*(3), 317–337. https://doi.org/10.1623/hysj.48.3.317.45290

Alkama, R., Decharme, B., Douville, H., Becker, M., Cazenave, A., Sheffield, J., et al. (2010). Global Evaluation of the ISBA-TRIP Continental Hydrological System. Part I: Comparison to GRACE Terrestrial Water Storage Estimates and In Situ River Discharges. *Journal of Hydrometeorology*, *11*(3), 583–600. https://doi.org/10.1175/2010JHM1211.1

Alley, W. M., Healy, R. W., LaBaugh, J. W., & Reilly, T. E. (2002). Flow and Storage in Groundwater Systems. *Science*, *296*(5575), 1985–1990. https://doi.org/10.1126/science.1067123

Alvarez-Garreton, C., Ryu, D., Western, A. W., Crow, W. T., Su, C.-H., & Robertson, D. R. (2016). Dual assimilation of satellite soil moisture to improve streamflow prediction in data-scarce catchments. *Water Resources Research*, *52*(7), 5357–5375. https://doi.org/10.1002/2015WR018429

Anderson, M. P., Woessner, W. W., & Hunt, R. J. (2015). *Applied Groundwater Modeling: Simulation of Flow and Advective Transport*. Academic Press.

Arnell, N. W. (1999). Climate change and global water resources. *Global Environmental Change*, *9*, S31–S49. https://doi.org/10.1016/S0959-3780(99)00017-5

Arnell, N. W. (2004). Climate change and global water resources: SRES emissions and socio-economic scenarios. *Global Environmental Change*, *14*(1), 31–52. https://doi.org/10.1016/j.gloenvcha.2003.10.006

Batjes, N. H. (2005). *ISRIC-WISE global data set of derived soil properties on a 0.5 by 0.5 degree grid (version 3.0, with data set).* ISRIC, World Soil Inf. Ctr., Wageningen, the Netherlands.

van Beek, L. P. H., Wada, Y., & Bierkens, M. F. P. (2011). Global monthly water stress: 1. Water balance and water availability. *Water Resources Research*, *47*(7), W07517. https://doi.org/10.1029/2010WR009791

Bell, J. E., Palecki, M. A., Baker, C. B., Collins, W. G., Lawrimore, J. H., Leeper, R. D., et al. (2013). U.S. Climate Reference Network Soil Moisture and Temperature Observations. *Journal of Hydrometeorology*, *14*(3), 977–988. https://doi.org/10.1175/JHM-D-12-0146.1

Bertoldi, G. L. (1989). *Ground-water resources of the Central Valley of California* (USGS Numbered Series No. 89–251). Department of the Interior, U.S. Geological Survey,. Retrieved from http://pubs.er.usgs.gov/publication/ofr89251

Bertoldi, G. L., Johnston, R. H., & Evenson, K. D. (1991). *Ground water in the Central Valley, California; a summary report* (USGS Numbered Series No. 1401- A). U.S. Geological Survey. Retrieved from http://pubs.er.usgs.gov/publication/pp1401A

Beven, K. J., & Kirkby, M. J. (1979). A physically based, variable contributing area model of basin hydrology / Un modèle à base physique de zone d'appel variable de l'hydrologie du bassin versant. *Hydrological Sciences Bulletin*, *24*(1), 43–69. https://doi.org/10.1080/02626667909491834

Biemans, H., Haddeland, I., Kabat, P., Ludwig, F., Hutjes, R. W. A., Heinke, J., et al. (2011). Impact of reservoirs on river discharge and irrigation water supply during the 20th century. *Water Resources Research*, *47*(3), W03509. https://doi.org/10.1029/2009WR008929

Bierkens, M. F. P. (2015). Global hydrology 2015: State, trends, and directions. *Water Resources Research*, *51*(7), 4923–4947. https://doi.org/10.1002/2015WR017173

Bitar, A. A., Leroux, D., Kerr, Y. H., Merlin, O., Richaume, P., Sahoo, A., & Wood, E. F. (2012). Evaluation of SMOS Soil Moisture Products Over Continental U.S. Using the SCAN/SNOTEL Network. *IEEE Transactions on Geoscience and Remote Sensing*, *50*(5), 1572–1586. https://doi.org/10.1109/TGRS.2012.2186581

Bondeau, A., Smith, P. C., Zaehle, S., Schaphoff, S., Lucht, W., Cramer, W., et al. (2007). Modelling the role of agriculture for the 20th century global terrestrial carbon balance. *Global Change Biology*, *13*(3), 679–706. https://doi.org/10.1111/j.1365-2486.2006.01305.x

Boucher, O., Myhre, G., & Myhre, A. (2004). Direct human influence of irrigation on atmospheric water vapour and climate. *Climate Dynamics*, *22*(6–7), 597–603. https://doi.org/10.1007/s00382-004-0402-4

Brocca, L., Tarpanelli, A., Filippucci, P., Dorigo, W., Zaussinger, F., Gruber, A., & Fernández-Prieto, D. (2018). How much water is used for irrigation? A new approach exploiting coarse resolution satellite soil moisture products. *International Journal of Applied Earth Observation and Geoinformation*, *73*, 752–766. https://doi.org/10.1016/j.jag.2018.08.023

Burek, P., Satoh, Y., Kahil, T., Tang, T., Greve, P., Smilovic, M., et al. (2019). Development of the Community Water Model (CWatM v1.04) A high-resolution hydrological model for global and regional assessment of integrated water resources management. *Geoscientific Model Development Discussions*, 1–49. https://doi.org/10.5194/gmd-2019-214

Castellazzi, P., Martel, R., Rivera, A., Huang, J., Pavlic, G., Calderhead, A. I., et al. (2016). Groundwater depletion in Central Mexico: Use of GRACE and InSAR to support water resources management. *Water Resources Research*, *52*(8), 5985–6003. https://doi.org/10.1002/2015WR018211

Chambers, D. P., Cazenave, A., Champollion, N., Dieng, H., Llovel, W., Forsberg, R., et al. (2017). Evaluation of the Global Mean Sea Level Budget Between 1993 and 2014. In A. Cazenave, N. Champollion, F. Paul, & J. Benveniste (Eds.), *Integrative Study of the Mean Sea Level and Its Components* (pp. 315–333). Cham: Springer International Publishing. https://doi.org/10.1007/978-3-319-56490-6_14

Chan, S. K., Bindlish, R., O'Neill, P. E., Njoku, E., Jackson, T., Colliander, A., et al. (2016). Assessment of the SMAP Passive Soil Moisture Product. *IEEE Transactions on Geoscience and Remote Sensing*, *54*(8), 4994–5007. https://doi.org/10.1109/TGRS.2016.2561938

Chaudhari, S., Felfelani, F., Shin, S., & Pokhrel, Y. (2018). Climate and anthropogenic contributions to the desiccation of the second largest saline lake in the twentieth century. *Journal of Hydrology*, *560*, 342–353. https://doi.org/10.1016/j.jhydrol.2018.03.034

Chaudhari, S., Pokhrel, Y., Moran, E., & Miguez-Macho, G. (2019). Multi-decadal hydrologic change and variability in the Amazon River basin: understanding terrestrial water storage variations and drought characteristics. *Hydrology and Earth System Sciences*, *23*(7), 2841–2862. https://doi.org/10.5194/hess-23-2841-2019

Chen, X., Long, D., Hong, Y., Zeng, C., & Yan, D. (2017). Improved modeling of snow and glacier melting by a progressive two-stage calibration strategy with GRACE and multisource data: How snow and glacier meltwater contributes to the runoff of the Upper

Brahmaputra River basin? *Water Resources Research*, *53*(3), 2431–2466. https://doi.org/10.1002/2016WR019656

Clapp, R. B., & Hornberger, G. M. (1978). Empirical equations for some soil hydraulic properties. *Water Resources Research*, *14*(4), 601–604. https://doi.org/10.1029/WR014i004p00601

Clerman, N. S., & Spector, W. (2011). *Modern Fortran: Style and Usage*. Cambridge University Press.

Collatz, G. J., Ball, J. T., Grivet, C., & Berry, J. A. (1991). Physiological and environmental regulation of stomatal conductance, photosynthesis and transpiration: a model that includes a laminar boundary layer. *Agricultural and Forest Meteorology*, *54*(2), 107–136. https://doi.org/10.1016/0168-1923(91)90002-8

Condon, L. E., & Maxwell, R. M. (2019). Simulating the sensitivity of evapotranspiration and streamflow to large-scale groundwater depletion. *Science Advances*, *5*(6), eaav4574. https://doi.org/10.1126/sciadv.aav4574

Cuthbert, M. O., Taylor, R. G., Favreau, G., Todd, M. C., Shamsudduha, M., Villholth, K. G., et al. (2019). Observed controls on resilience of groundwater to climate variability in sub-Saharan Africa. *Nature*, *572*(7768), 230–234. https://doi.org/10.1038/s41586-019-1441-7

Decharme, B., & Douville, H. (2006). Uncertainties in the GSWP-2 precipitation forcing and their impacts on regional and global hydrological simulations. *Climate Dynamics*, *27*(7–8), 695–713. https://doi.org/10.1007/s00382-006-0160-6

Decharme, B., Alkama, R., Douville, H., Becker, M., & Cazenave, A. (2010). Global Evaluation of the ISBA-TRIP Continental Hydrological System. Part II: Uncertainties in River Routing Simulation Related to Flow Velocity and Groundwater Storage. *Journal of Hydrometeorology*, *11*(3), 601–617. https://doi.org/10.1175/2010JHM1212.1

Deines, J. M., Kendall, A. D., & Hyndman, D. W. (2017). Annual Irrigation Dynamics in the U.S. Northern High Plains Derived from Landsat Satellite Data. *Geophysical Research Letters*, GL074071. https://doi.org/10.1002/2017GL074071

Dennehy, K. F., Litke, D. W., & McMahon, P. B. (2002). The High Plains Aquifer, USA: Groundwater development and sustainability. *Geological Society Special Publication*, (193), 21.

Dieter, C. A., Maupin, M. A., Caldwell, R. R., Harris, M. A., Ivahnenko, T. I., Lovelace, J. K., et al. (2018). Estimated use of water in the United States in 2015: U.S. Geological Survey Circular 1441, 65 p. https://doi.org/10.3133/cir1441. [Supersedes USGS Open-File Report 2017–1131.]

van Dijk, A. I. J. M., & Renzullo, L. J. (2011). Water resource monitoring systems and the role of satellite observations. *Hydrology and Earth System Sciences*, *15*(1), 39–55. https://doi.org/10.5194/hess-15-39-2011

Dirmeyer, P. A., Gao, X., Zhao, M., Guo, Z., Oki, T., & Hanasaki, N. (2006). GSWP-2: Multimodel Analysis and Implications for Our Perception of the Land Surface. *Bulletin of the American Meteorological Society*, *87*(10), 1381–1397. https://doi.org/10.1175/BAMS-87-10-1381

Dirmeyer, P. A., Wu, J., Norton, H. E., Dorigo, W. A., Quiring, S. M., Ford, T. W., et al. (2016). Confronting Weather and Climate Models with Observational Data from Soil Moisture Networks over the United States. *Journal of Hydrometeorology*, *17*(4), 1049–1067. https://doi.org/10.1175/JHM-D-15-0196.1

Dirmeyer, P. A., Chen, L., Wu, J., Shin, C.-S., Huang, B., Cash, B. A., et al. (2017). Verification of Land–Atmosphere Coupling in Forecast Models, Reanalyses, and Land Surface Models Using Flux Site Observations. *Journal of Hydrometeorology*, *19*(2), 375–392. https://doi.org/10.1175/JHM-D-17-0152.1

Döll, P. (2002). Impact of Climate Change and Variability on Irrigation Requirements: A Global Perspective. *Climatic Change*, *54*(3), 269–293. https://doi.org/10.1023/A:1016124032231

Döll, P., & Siebert, S. (2002). Global modeling of irrigation water requirements. *Water Resources Research*, *38*(4), 8-1-8–10. https://doi.org/10.1029/2001WR000355

Döll, P., Kaspar, F., & Alcamo, J. (1999). Computation of global water availability and water use at the scale of large drainage basins. *Mathematische Geologie*, (4), 115–122.

Döll, P., Kaspar, F., & Lehner, B. (2003). A global hydrological model for deriving water availability indicators: model tuning and validation. *Journal of Hydrology*, *270*(1–2), 105–134. https://doi.org/10.1016/S0022-1694(02)00283-4

Döll, P., Hoffmann-Dobrev, H., Portmann, F. T., Siebert, S., Eicker, A., Rodell, M., et al. (2012). Impact of water withdrawals from groundwater and surface water on continental water storage variations. *Journal of Geodynamics*, *59–60*, 143–156. https://doi.org/10.1016/j.jog.2011.05.001

Döll, P., Müller Schmied, H., Schuh, C., Portmann, F. T., & Eicker, A. (2014). Global-scale assessment of groundwater depletion and related groundwater abstractions: Combining hydrological modeling with information from well observations and GRACE satellites. *Water Resources Research*, *50*(7), 5698–5720. https://doi.org/10.1002/2014WR015595

Döll, P., Douville, H., Güntner, A., Müller Schmied, H., & Wada, Y. (2016). Modelling Freshwater Resources at the Global Scale: Challenges and Prospects. In A. Cazenave, N. Champollion, J. Benveniste, & J. Chen (Eds.), *Remote Sensing and Water Resources* (pp. 5–31). Springer International Publishing. https://doi.org/10.1007/978-3-319-32449-4_2

Dong, J., Crow, W. T., & Bindlish, R. (2018). The Error Structure of the SMAP Single and Dual Channel Soil Moisture Retrievals. *Geophysical Research Letters*, *45*(2), 2017GL075656. https://doi.org/10.1002/2017GL075656

Duffy, C. J. (1996). A Two-State Integral-Balance Model for Soil Moisture and Groundwater Dynamics in Complex Terrain. *Water Resources Research*, *32*(8), 2421–2434. https://doi.org/10.1029/96WR01049

Eicker, A., Schumacher, M., Kusche, J., Döll, P., & Müller Schmied, H. (2014). Calibration/Data Assimilation Approach for Integrating GRACE Data into the WaterGAP Global Hydrology Model (WGHM) Using an Ensemble Kalman Filter: First Results. *Surveys in Geophysics*, *35*(6), 1285–1309. https://doi.org/10.1007/s10712-014-9309-8

Eicker, A., Forootan, E., Springer, A., Longuevergne, L., & Kusche, J. (2016). Does GRACE see the terrestrial water cycle "intensifying"? *Journal of Geophysical Research: Atmospheres*, *121*(2), 2015JD023808. https://doi.org/10.1002/2015JD023808

Eyring, V., Cox, P. M., Flato, G. M., Gleckler, P. J., Abramowitz, G., Caldwell, P., et al. (2019). Taking climate model evaluation to the next level. *Nature Climate Change*, *9*(2), 102. https://doi.org/10.1038/s41558-018-0355-y

Famiglietti, J. S. (2014). The global groundwater crisis. *Nature Climate Change*, *4*(11), 945–948. https://doi.org/10.1038/nclimate2425

Famiglietti, J. S., Lo, M., Ho, S. L., Bethune, J., Anderson, K. J., Syed, T. H., et al. (2011). Satellites measure recent rates of groundwater depletion in California's Central Valley. *Geophysical Research Letters*, *38*(3), L03403. https://doi.org/10.1029/2010GL046442

Famiglietti, J. S., Cazenave, A., Eicker, A., Reager, J. T., Rodell, M., & Velicogna, I. (2015). Satellites provide the big picture. *Science*, *349*(6249), 684–685. https://doi.org/10.1126/science.aac9238

Fan, Y. (2015). Groundwater in the Earth's critical zone: Relevance to large-scale patterns and processes. *Water Resources Research*, *51*(5), 3052–3069. https://doi.org/10.1002/2015WR017037

Fan, Y., Miguez-Macho, G., Weaver, C. P., Walko, R., & Robock, A. (2007). Incorporating water table dynamics in climate modeling: 1. Water table observations and equilibrium water table simulations. *Journal of Geophysical Research: Atmospheres*, *112*(D10), D10125. https://doi.org/10.1029/2006JD008111

Fan, Y., Li, H., & Miguez-Macho, G. (2013). Global Patterns of Groundwater Table Depth. *Science*, *339*(6122), 940–943. https://doi.org/10.1126/science.1229881

Fan, Y., Clark, M., Lawrence, D. M., Swenson, S., Band, L. E., Brantley, S. L., et al. (2019). Hillslope Hydrology in Global Change Research and Earth System Modeling. *Water Resources Research*, *55*(2), 1737–1772. https://doi.org/10.1029/2018WR023903

FAO. (2003). *Food and Agriculture Organization of the United Nations (FAO) (2003), Digital Soil Map of the World, Version 3.6.* Rome, Italy.

Faunt, C. C. (2009). *Groundwater Availability of the Central Valley Aquifer, California* (USGS Numbered Series) (p. 225 p). U.S. Geological Survey Professional Paper 1766. Retrieved from URL: https://pubs.usgs.gov/pp/1766/

Feinstein, D. T., Fienen, M. N., Reeves, H. W., & Langevin, C. D. (2016). A Semi-Structured MODFLOW-USG Model to Evaluate Local Water Sources to Wells for Decision Support. *Groundwater*, *54*(4), 532–544. https://doi.org/10.1111/gwat.12389

Felfelani, F., Wada, Y., Longuevergne, L., & Pokhrel, Y. (2017). Natural and human-induced terrestrial water storage change: A global analysis using hydrological models and GRACE. *Journal of Hydrology*, *553*, 105–118. https://doi.org/10.1016/j.jhydrol.2017.07.048

Felfelani, F., Pokhrel, Y., Guan, K., & Lawrence, D. M. (2018). Utilizing SMAP Soil Moisture Data to Constrain Irrigation in the Community Land Model. *Geophysical Research Letters*, *0*(ja). https://doi.org/10.1029/2018GL080870

Feng, W., Zhong, M., Lemoine, J.-M., Biancale, R., Hsu, H.-T., & Xia, J. (2013). Evaluation of groundwater depletion in North China using the Gravity Recovery and Climate Experiment (GRACE) data and ground-based measurements. *Water Resources Research*, *49*(4), 2110–2118. https://doi.org/10.1002/wrcr.20192

Foley, J. A., DeFries, R., Asner, G. P., Barford, C., Bonan, G., Carpenter, S. R., et al. (2005). Global Consequences of Land Use. *Science*, *309*(5734), 570–574. https://doi.org/10.1126/science.1111772

Freedman, F. R., Pitts, K. L., & Bridger, A. F. C. (2014). Evaluation of CMIP climate model hydrological output for the Mississippi River Basin using GRACE satellite observations. *Journal of Hydrology*, *519, Part D*, 3566–3577. https://doi.org/10.1016/j.jhydrol.2014.10.036

Frieler, K., Lange, S., Piontek, F., Reyer, C. P. O., Schewe, J., Warszawski, L., et al. (2017). Assessing the impacts of 1.5 °C global warming – simulation protocol of the Inter-Sectoral Impact Model Intercomparison Project (ISIMIP2b). *Geoscientific Model Development*, *10*(12), 4321–4345. https://doi.org/10.5194/gmd-10-4321-2017

Ge, S., Yang, D., & Kane, D. L. (2013). Yukon River Basin long-term (1977–2006) hydrologic and climatic analysis. *Hydrological Processes*, *27*(17), 2475–2484. https://doi.org/10.1002/hyp.9282

Giordano, M. (2009). Global Groundwater? Issues and Solutions. *Annual Review of Environment and Resources*, *34*(1), 153–178. https://doi.org/10.1146/annurev.environ.030308.100251

Girotto, M., De Lannoy, G. J. M., Reichle, R. H., & Rodell, M. (2016). Assimilation of gridded terrestrial water storage observations from GRACE into a land surface model. *Water Resources Research*, *52*(5), 4164–4183. https://doi.org/10.1002/2015WR018417

Gleeson, T., Wada, Y., Bierkens, M. F. P., & van Beek, L. P. H. (2012). Water balance of global aquifers revealed by groundwater footprint. *Nature*, *488*(7410), 197–200. https://doi.org/10.1038/nature11295

Goldewijk, K. K., Beusen, A., van Drecht, G., & de Vos, M. (2011). The HYDE 3.1 spatially explicit database of human-induced global land-use change over the past 12,000 years. *Global Ecology and Biogeography*, *20*(1), 73–86. https://doi.org/10.1111/j.1466-8238.2010.00587.x

Gosling, S. N., & Arnell, N. W. (2016). A global assessment of the impact of climate change on water scarcity. *Climatic Change*, *134*(3), 371–385. https://doi.org/10.1007/s10584-013-0853-x

de Graaf, I. E. M., Sutanudjaja, E. H., van Beek, L. P. H., & Bierkens, M. F. P. (2015). A high-resolution global-scale groundwater model. *Hydrology and Earth System Sciences*, *19*(2), 823–837. https://doi.org/10.5194/hess-19-823-2015

de Graaf, I. E. M., van Beek, R. L. P. H., Gleeson, T., Moosdorf, N., Schmitz, O., Sutanudjaja, E. H., & Bierkens, M. F. P. (2017). A global-scale two-layer transient groundwater model: Development and application to groundwater depletion. *Advances in Water Resources*, *102*, 53–67. https://doi.org/10.1016/j.advwatres.2017.01.011

de Graaf, I. E. M., Gleeson, T., van Beek, L. P. H., Sutanudjaja, E. H., & Bierkens, M. F. P. (2019). Environmental flow limits to global groundwater pumping. *Nature*, *574*(7776), 90–94. https://doi.org/10.1038/s41586-019-1594-4

Grippa, M., Kergoat, L., Frappart, F., Araud, Q., Boone, A., de Rosnay, P., et al. (2011). Land water storage variability over West Africa estimated by Gravity Recovery and Climate Experiment (GRACE) and land surface models. *Water Resources Research*, *47*(5), W05549. https://doi.org/10.1029/2009WR008856

Gudmundsson, L., Seneviratne, S. I., & Zhang, X. (2017). Anthropogenic climate change detected in European renewable freshwater resources. *Nature Climate Change*, *7*(11), 813–816. https://doi.org/10.1038/nclimate3416

Güntner, A. (2008). Improvement of Global Hydrological Models Using GRACE Data. *Surveys in Geophysics*, *29*(4–5), 375–397. https://doi.org/10.1007/s10712-008-9038-y

Haddeland, I., Skaugen, T., & Lettenmaier, D. P. (2006). Anthropogenic impacts on continental surface water fluxes. *Geophysical Research Letters*, *33*(8), L08406. https://doi.org/10.1029/2006GL026047

Haddeland, I., Lettenmaier, D. P., & Skaugen, T. (2006). Effects of irrigation on the water and energy balances of the Colorado and Mekong river basins. *Journal of Hydrology*, *324*(1), 210–223. https://doi.org/10.1016/j.jhydrol.2005.09.028

Haddeland, I., Clark, D. B., Franssen, W., Ludwig, F., Voß, F., Arnell, N. W., et al. (2011). Multimodel Estimate of the Global Terrestrial Water Balance: Setup and First Results. *Journal of Hydrometeorology*, *12*(5), 869–884. https://doi.org/10.1175/2011JHM1324.1

Haddeland, I., Heinke, J., Biemans, H., Eisner, S., Flörke, M., Hanasaki, N., et al. (2014). Global water resources affected by human interventions and climate change. *Proceedings of the National Academy of Sciences*, *111*(9), 3251–3256. https://doi.org/10.1073/pnas.1222475110

Hagemann, S. (2002). *An improved land surface parameter dataset for global and regional climate models* (Vol. 336). Hamburg: Max-Planck-Institut für Meteorologie.

Hanasaki, N., Kanae, S., & Oki, T. (2006). A reservoir operation scheme for global river routing models. *Journal of Hydrology*, *327*(1–2), 22–41. https://doi.org/10.1016/j.jhydrol.2005.11.011

Hanasaki, N., Kanae, S., Oki, T., Masuda, K., Motoya, K., Shirakawa, N., et al. (2008a). An integrated model for the assessment of global water resources – Part 1: Model description and input meteorological forcing. *Hydrology and Earth System Sciences*, *12*(4), 1007–1025. https://doi.org/10.5194/hess-12-1007-2008

Hanasaki, N., Kanae, S., Oki, T., Masuda, K., Motoya, K., Shirakawa, N., et al. (2008b). An integrated model for the assessment of global water resources – Part 2: Applications and assessments. *Hydrology and Earth System Sciences*, *12*(4), 1027–1037. https://doi.org/10.5194/hess-12-1027-2008

Hanasaki, N., Fujimori, S., Yamamoto, T., Yoshikawa, S., Masaki, Y., Hijioka, Y., et al. (2013a). A global water scarcity assessment under Shared Socio-economic Pathways – Part 1: Water use. *Hydrology and Earth System Sciences*, *17*(7), 2375–2391. https://doi.org/10.5194/hess-17-2375-2013

Hanasaki, N., Fujimori, S., Yamamoto, T., Yoshikawa, S., Masaki, Y., Hijioka, Y., et al. (2013b). A global water scarcity assessment under Shared Socio-economic Pathways – Part 2: Water availability and scarcity. *Hydrology and Earth System Sciences*, *17*(7), 2393–2413. https://doi.org/10.5194/hess-17-2393-2013

Hanasaki, N., Yoshikawa, S., Pokhrel, Y., & Kanae, S. (2018). A global hydrological simulation to specify the sources of water used by humans. *Hydrol. Earth Syst. Sci.*, *22*(1), 789–817. https://doi.org/10.5194/hess-22-789-2018

Harding, K. J., & Snyder, P. K. (2012). Modeling the Atmospheric Response to Irrigation in the Great Plains. Part I: General Impacts on Precipitation and the Energy Budget. *Journal of Hydrometeorology*, *13*(6), 1667–1686. https://doi.org/10.1175/JHM-D-11-098.1

He, L., Chen, J. M., Liu, J., Bélair, S., & Luo, X. (2017). Assessment of SMAP soil moisture for global simulation of gross primary production. *Journal of Geophysical Research: Biogeosciences*, *122*(7), 1549–1563. https://doi.org/10.1002/2016JG003603

Hempel, S., Frieler, K., Warszawski, L., Schewe, J., & Piontek, F. (2013). A trend-preserving bias correction – the ISI-MIP approach. *Earth Syst. Dynam.*, *4*(2), 219–236. https://doi.org/10.5194/esd-4-219-2013

Hirabayashi, Y., Kanae, S., Struthers, I., & Oki, T. (2005). A 100-year (1901–2000) global retrospective estimation of the terrestrial water cycle. *Journal of Geophysical Research: Atmospheres*, *110*(D19), D19101. https://doi.org/10.1029/2004JD005492

Hirschi, M., Seneviratne, S. I., & Schär, C. (2006). Seasonal Variations in Terrestrial Water Storage for Major Midlatitude River Basins. *Journal of Hydrometeorology*, *7*(1), 39–60. https://doi.org/10.1175/JHM480.1

Houborg, R., Rodell, M., Li, B., Reichle, R., & Zaitchik, B. F. (2012). Drought indicators based on model-assimilated Gravity Recovery and Climate Experiment (GRACE) terrestrial water storage observations. *Water Resources Research*, *48*(7), W07525. https://doi.org/10.1029/2011WR011291

Huang, Y., Salama, M. S., Krol, M. S., Su, Z., Hoekstra, A. Y., Zeng, Y., & Zhou, Y. (2015). Estimation of human-induced changes in terrestrial water storage through integration of GRACE satellite detection and hydrological modeling: A case study of the Yangtze River basin. *Water Resources Research*, *51*(10), 8494–8516. https://doi.org/10.1002/2015WR016923

IPCC. (2013). *Climate Change 2013—The Physical Science Basis: Working Group I Contribution to the Fifth Assessment Report of the Intergovernmental Panel on Climate Change*. Cambridge University Press. Retrieved from https://www.ipcc.ch/report/ar5/wg1/

Jägermeyr, J., Gerten, D., Heinke, J., Schaphoff, S., Kummu, M., & Lucht, W. (2015). Water savings potentials of irrigation systems: global simulation of processes and linkages. *Hydrol. Earth Syst. Sci.*, *19*(7), 3073–3091. https://doi.org/10.5194/hess-19-3073-2015

Jin, J., & Miller, N. L. (2011). Regional simulations to quantify land use change and irrigation impacts on hydroclimate in the California Central Valley. *Theoretical and Applied Climatology*, *104*(3–4), 429–442. https://doi.org/10.1007/s00704-010-0352-1

Jin, S., & Feng, G. (2013). Large-scale variations of global groundwater from satellite gravimetry and hydrological models, 2002–2012. *Global and Planetary Change*, *106*, 20–30. https://doi.org/10.1016/j.gloplacha.2013.02.008

Khaki, M., & Awange, J. (2019). The application of multi-mission satellite data assimilation for studying water storage changes over South America. *Science of The Total Environment*, *647*, 1557–1572. https://doi.org/10.1016/j.scitotenv.2018.08.079

Kim, H., Yeh, P. J.-F., Oki, T., & Kanae, S. (2009). Role of rivers in the seasonal variations of terrestrial water storage over global basins. *Geophysical Research Letters*, *36*(17), L17402. https://doi.org/10.1029/2009GL039006

Klees, R., Liu, X., Wittwer, T., Gunter, B. C., Revtova, E. A., Tenzer, R., et al. (2008). A Comparison of Global and Regional GRACE Models for Land Hydrology. *Surveys in Geophysics*, *29*(4–5), 335–359. https://doi.org/10.1007/s10712-008-9049-8

Koirala, S., Yeh, P. J.-F., Hirabayashi, Y., Kanae, S., & Oki, T. (2014). Global-scale land surface hydrologic modeling with the representation of water table dynamics. *Journal of Geophysical Research: Atmospheres*, *119*(1), 2013JD020398. https://doi.org/10.1002/2013JD020398

Koirala, S., Kim, H., Hirabayashi, Y., Kanae, S., & Oki, T. (2019). Sensitivity of Global Hydrological Simulations to Groundwater Capillary Flux Parameterizations. *Water Resources Research*, *55*(1), 402–425. https://doi.org/10.1029/2018WR023434

Konikow, L. F. (2011). Contribution of global groundwater depletion since 1900 to sea-level rise. *Geophysical Research Letters*, *38*(17). https://doi.org/10.1029/2011GL048604

Konikow, L. F. (2013). *Groundwater depletion in the United States (1900−2008)* (USGS Numbered Series No. 2013–5079) (p. 75). Reston, VA: U.S. Geological Survey. Retrieved from http://pubs.er.usgs.gov/publication/sir20135079

Koster, R. D. (2004). Regions of Strong Coupling Between Soil Moisture and Precipitation. *Science*, *305*(5687), 1138–1140. https://doi.org/10.1126/science.1100217

Kraijenhoff Van De Leur, D. A. (1958). A study of non-steady groundwater flow with special reference to a reservoir-coefficient. *De Ingenieur*, *70*(19), 87–94.

Krakauer, N. Y., Li, H., & Fan, Y. (2014). Groundwater flow across spatial scales: importance for climate modeling. *Environmental Research Letters*, *9*(3), 034003. https://doi.org/10.1088/1748-9326/9/3/034003

Krysanova, V., Müller-Wohlfeil, D.-I., & Becker, A. (1998). Development and test of a spatially distributed hydrological/water quality model for mesoscale watersheds. *Ecological Modelling*, *106*(2–3), 261–289. https://doi.org/10.1016/S0304-3800(97)00204-4

Kucharik, C. J., Foley, J. A., Delire, C., Fisher, V. A., Coe, M. T., Lenters, J. D., et al. (2000). Testing the performance of a dynamic global ecosystem model: Water balance, carbon balance, and vegetation structure. *Global Biogeochemical Cycles*, *14*(3), 795–825. https://doi.org/10.1029/1999GB001138

Kumar, S. V., Reichle, R. H., Harrison, K. W., Peters-Lidard, C. D., Yatheendradas, S., & Santanello, J. A. (2012). A comparison of methods for a priori bias correction in soil moisture data assimilation. *Water Resources Research*, *48*(3). https://doi.org/10.1029/2010WR010261

Kumar, S. V., Peters-Lidard, C. D., Santanello, J. A., Reichle, R. H., Draper, C. S., Koster, R. D., et al. (2015). Evaluating the utility of satellite soil moisture retrievals over irrigated areas and the ability of land data assimilation methods to correct for unmodeled processes. *Hydrol. Earth Syst. Sci.*, *19*(11), 4463–4478. https://doi.org/10.5194/hess-19-4463-2015

Kumar, S. V., Dirmeyer, P. A., Peters-Lidard, C. D., Bindlish, R., & Bolten, J. (2018). Information theoretic evaluation of satellite soil moisture retrievals. *Remote Sensing of Environment*, *204*, 392–400. https://doi.org/10.1016/j.rse.2017.10.016

Kustu, M. D., Fan, Y., & Robock, A. (2010). Large-scale water cycle perturbation due to irrigation pumping in the US High Plains: A synthesis of observed streamflow changes. *Journal of Hydrology*, *390*(3), 222–244. https://doi.org/10.1016/j.jhydrol.2010.06.045

Landerer, F. W., & Swenson, S. C. (2012). Accuracy of scaled GRACE terrestrial water storage estimates. *Water Resources Research*, *48*(4), W04531. https://doi.org/10.1029/2011WR011453

Landerer, F. W., Dickey, J. O., & Güntner, A. (2010). Terrestrial water budget of the Eurasian pan-Arctic from GRACE satellite measurements during 2003–2009. *Journal of Geophysical Research: Atmospheres*, *115*(D23), D23115. https://doi.org/10.1029/2010JD014584

Landerer, F. W., Gleckler, P. J., & Lee, T. (2013). Evaluation of CMIP5 dynamic sea surface height multi-model simulations against satellite observations. *Climate Dynamics*, *43*(5–6), 1271–1283. https://doi.org/10.1007/s00382-013-1939-x

Lange, S. (2018). Bias correction of surface downwelling longwave and shortwave radiation for the EWEMBI dataset. *Earth System Dynamics*, *9*(2), 627–645. https://doi.org/10.5194/esd-9-627-2018

Lange, S. (2019). Trend-preserving bias adjustment and statistical downscaling with ISIMIP3BASD (v1.0). *Geoscientific Model Development*, *12*(7), 3055–3070. https://doi.org/10.5194/gmd-12-3055-2019

Lawrence, D. M., Oleson, K. W., Flanner, M. G., Thornton, P. E., Swenson, S. C., Lawrence, P. J., et al. (2011). Parameterization improvements and functional and structural advances in Version 4 of the Community Land Model. *Journal of Advances in Modeling Earth Systems*, *3*(1), M03001. https://doi.org/10.1029/2011MS00045

Lawrence, D. M., Fisher, R. A., Koven, C. D., Oleson, K. W., Swenson, S. C., Bonan, G., et al. (2019). The Community Land Model version 5: Description of new features, benchmarking, and impact of forcing uncertainty. *Journal of Advances in Modeling Earth Systems*, *0*(ja). https://doi.org/10.1029/2018MS001583

Lawston, P. M., Santanello Jr., J. A., Zaitchik, B. F., & Rodell, M. (2015). Impact of Irrigation Methods on Land Surface Model Spinup and Initialization of WRF Forecasts. *Journal of Hydrometeorology*, *16*(3), 1135–1154. https://doi.org/10.1175/JHM-D-14-0203.1

Lawston, P. M., Santanello Jr., J. A., Franz, T. E., & Rodell, M. (2017). Assessment of irrigation physics in a land surface modeling framework using non-traditional and human-practice datasets. *Hydrol. Earth Syst. Sci.*, *21*(6), 2953–2966. https://doi.org/10.5194/hess-21-2953-2017

Lawston, P. M., Santanello Jr., J. A., & Kumar, S. V. (2017). Irrigation Signals Detected From SMAP Soil Moisture Retrievals. *Geophysical Research Letters*, 2017GL075733. https://doi.org/10.1002/2017GL075733

Lehner, B., Liermann, C. R., Revenga, C., Vörösmarty, C., Fekete, B., Crouzet, P., et al. (2011). High-resolution mapping of the world's reservoirs and dams for sustainable river-flow management. *Frontiers in Ecology and the Environment*, *9*(9), 494–502. https://doi.org/10.1890/100125

Leng, G., Huang, M., Tang, Q., Gao, H., & Leung, L. R. (2013). Modeling the Effects of Groundwater-Fed Irrigation on Terrestrial Hydrology over the Conterminous United States. *Journal of Hydrometeorology*, *15*(3), 957–972. https://doi.org/10.1175/JHM-D-13-049.1

Leng, G., Huang, M., Tang, Q., Sacks, W. J., Lei, H., & Leung, L. R. (2013). Modeling the effects of irrigation on land surface fluxes and states over the conterminous United States: Sensitivity to input data and model parameters. *Journal of Geophysical Research: Atmospheres*, *118*(17), 9789–9803. https://doi.org/10.1002/jgrd.50792

Leng, G., Huang, M., Tang, Q., & Leung, L. R. (2015). A modeling study of irrigation effects on global surface water and groundwater resources under a changing climate. *Journal of Advances in Modeling Earth Systems*, *7*(3), 1285–1304. https://doi.org/10.1002/2015MS000437

Levis, S., Bonan, G. B., Kluzek, E., Thornton, P. E., Jones, A., Sacks, W. J., & Kucharik, C. J. (2012). Interactive Crop Management in the Community Earth System Model (CESM1): Seasonal Influences on Land–Atmosphere Fluxes. *Journal of Climate*, *25*(14), 4839–4859. https://doi.org/10.1175/JCLI-D-11-00446.1

Li, B., & Rodell, M. (2015). Evaluation of a model-based groundwater drought indicator in the conterminous U.S. *Journal of Hydrology*, *526*, 78–88. https://doi.org/10.1016/j.jhydrol.2014.09.027

Li, B., Rodell, M., Zaitchik, B. F., Reichle, R. H., Koster, R. D., & van Dam, T. M. (2012). Assimilation of GRACE terrestrial water storage into a land surface model: Evaluation and potential value for drought monitoring in western and central Europe. *Journal of Hydrology*, *446–447*, 103–115. https://doi.org/10.1016/j.jhydrol.2012.04.035

Li, H., Wigmosta, M. S., Wu, H., Huang, M., Ke, Y., Coleman, A. M., & Leung, L. R. (2013). A Physically Based Runoff Routing Model for Land Surface and Earth System Models. *Journal of Hydrometeorology*, *14*(3), 808–828. https://doi.org/10.1175/JHM-D-12-015.1

Li, S.-G., & Liu, Q. (2006). Interactive Ground Water (IGW). *Environmental Modelling & Software*, *21*(3), 417–418. https://doi.org/10.1016/j.envsoft.2005.05.010

Li, S.-G., Liu, Q., & Afshari, S. (2006). An object-oriented hierarchical patch dynamics paradigm (HPDP) for modeling complex groundwater systems across multiple-scales. *Environmental Modelling & Software*, *21*(5), 744–749. https://doi.org/10.1016/j.envsoft.2005.11.001

Liang, X., Xie, Z., & Huang, M. (2003). A new parameterization for surface and groundwater interactions and its impact on water budgets with the variable infiltration capacity (VIC) land surface model. *Journal of Geophysical Research: Atmospheres*, *108*(D16). https://doi.org/10.1029/2002JD003090

Lievens, H., Tomer, S. K., Al Bitar, A., De Lannoy, G. J. M., Drusch, M., Dumedah, G., et al. (2015). SMOS soil moisture assimilation for improved hydrologic simulation in the Murray Darling Basin, Australia. *Remote Sensing of Environment*, *168*, 146–162. https://doi.org/10.1016/j.rse.2015.06.025

Lievens, H., Reichle, R. H., Liu, Q., De Lannoy, G. J. M., Dunbar, R. S., Kim, S. B., et al. (2017). Joint Sentinel-1 and SMAP data assimilation to improve soil moisture estimates. *Geophysical Research Letters*, *44*(12), 2017GL073904. https://doi.org/10.1002/2017GL073904

Llovel, W., Becker, M., Cazenave, A., Crétaux, J.-F., & Ramillien, G. (2010). Global land water storage change from GRACE over 2002–2009; Inference on sea level. *Comptes Rendus Geoscience*, *342*(3), 179–188. https://doi.org/10.1016/j.crte.2009.12.004

Lo, M.-H., & Famiglietti, J. S. (2013). Irrigation in California's Central Valley strengthens the southwestern U.S. water cycle. *Geophysical Research Letters*, *40*(2), 301–306. https://doi.org/10.1002/grl.50108

Long, D., Longuevergne, L., & Scanlon, B. R. (2014). Uncertainty in evapotranspiration from land surface modeling, remote sensing, and GRACE satellites. *Water Resources Research*, *50*(2), 1131–1151. https://doi.org/10.1002/2013WR014581

Long, D., Yang, Y., Wada, Y., Hong, Y., Liang, W., Chen, Y., et al. (2015). Deriving scaling factors using a global hydrological model to restore GRACE total water storage changes for China's Yangtze River Basin. *Remote Sensing of Environment*, *168*, 177–193. https://doi.org/10.1016/j.rse.2015.07.003

Long, D., Longuevergne, L., & Scanlon, B. R. (2015). Global analysis of approaches for deriving total water storage changes from GRACE satellites. *Water Resources Research*, *51*(4), 2574–2594. https://doi.org/10.1002/2014WR016853

Long, D., Chen, X., Scanlon, B. R., Wada, Y., Hong, Y., Singh, V. P., et al. (2016). Have GRACE satellites overestimated groundwater depletion in the Northwest India Aquifer? *Scientific Reports*, *6*, 24398. https://doi.org/10.1038/srep24398

Long, D., Pan, Y., Zhou, J., Chen, Y., Hou, X., Hong, Y., et al. (2017). Global analysis of spatiotemporal variability in merged total water storage changes using multiple GRACE products and global hydrological models. *Remote Sensing of Environment*, *192*, 198–216. https://doi.org/10.1016/j.rse.2017.02.011

Longuevergne, L., Scanlon, B. R., & Wilson, C. R. (2010). GRACE Hydrological estimates for small basins: Evaluating processing approaches on the High Plains Aquifer, USA. *Water Resources Research*, *46*(11), W11517. https://doi.org/10.1029/2009WR008564

Maupin, M. A., Kenny, J. F., Hutson, S. S., Lovelace, J. K., Barber, N. L., & Linsey, K. S. (2014). Estimated use of water in the United States in 2010. *U.S. Geological Survey Circular 1405*, 56 p. https://dx.doi.org/10.3133/cir1405

Maxwell, R. M., & Condon, L. E. (2016). Connections between groundwater flow and transpiration partitioning. *Science*, *353*(6297), 377–380. https://doi.org/10.1126/science.aaf7891

Maxwell, R. M., & Miller, N. L. (2005). Development of a Coupled Land Surface and Groundwater Model. *Journal of Hydrometeorology*, *6*(3), 233–247. https://doi.org/10.1175/JHM422.1

McGuire, V. L. (2011). Water-Level Changes in the High Plains Aquifer, Predevelopment to 2009, 2007–08, and 2008–09, and Change in Water in Storage, Predevelopment to 2009. *Publications of the US Geological Survey*. Retrieved from https://digitalcommons.unl.edu/usgspubs/105

McGuire, V. L. (2014). *Water-Level Changes and Change in Water in Storage in the High Plains Aquifer, Predevelopment to 2013 and 2011–13* (USGS Numbered Series No. 2014–5218) (p. 14). Reston, VA: U.S. Geological Survey. Retrieved from https://pubs.usgs.gov/sir/2014/5218/

McGuire, V. L. (2017). *Water-level and recoverable water in storage changes, High Plains aquifer, predevelopment to 2015 and 2013–15* (USGS Numbered Series No. 2017–5040) (p. 24). Reston, VA: U.S. Geological Survey. Retrieved from http://pubs.er.usgs.gov/publication/sir20175040

Miao, C., Duan, Q., Sun, Q., Huang, Y., Kong, D., Yang, T., et al. (2014). Assessment of CMIP5 climate models and projected temperature changes over Northern Eurasia. *Environmental Research Letters*, *9*(5), 055007. https://doi.org/10.1088/1748-9326/9/5/055007

Müller Schmied, H., Adam, L., Eisner, S., Fink, G., Flörke, M., Kim, H., et al. (2016). Variations of global and continental water balance components as impacted by climate forcing uncertainty and human water use. *Hydrology and Earth System Sciences*, *20*(7), 2877–2898. https://doi.org/10.5194/hess-20-2877-2016

Nanteza, J., de Linage, C. R., Thomas, B. F., & Famiglietti, J. S. (2016). Monitoring groundwater storage changes in complex basement aquifers: An evaluation of the

GRACE satellites over East Africa. *Water Resources Research*, *52*(12), 9542–9564. https://doi.org/10.1002/2016WR018846

Nazemi, A., & Wheater, H. S. (2015a). On inclusion of water resource management in Earth system models - Part 1: Problem definition and representation of water demand. *Hydrology and Earth System Sciences*, *19*(1), 33–61. https://doi.org/10.5194/hess-19-33-2015

Nazemi, A., & Wheater, H. S. (2015b). On inclusion of water resource management in Earth system models – Part 1: Problem definition and representation of water demand. *Hydrol. Earth Syst. Sci.*, *19*(1), 33–61. https://doi.org/10.5194/hess-19-33-2015

Nie, W., Zaitchik, B. F., Rodell, M., Kumar, S. V., Anderson, M. C., & Hain, C. (2018). Groundwater Withdrawals Under Drought: Reconciling GRACE and Land Surface Models in the United States High Plains Aquifer. *Water Resources Research*, *54*(8), 5282–5299. https://doi.org/10.1029/2017WR022178

Niu, G.-Y., Yang, Z.-L., Dickinson, R. E., & Gulden, L. E. (2005). A simple TOPMODEL-based runoff parameterization (SIMTOP) for use in global climate models. *Journal of Geophysical Research: Atmospheres*, *110*(D21), D21106. https://doi.org/10.1029/2005JD006111

Niu, G.-Y., Yang, Z.-L., Mitchell, K. E., Chen, F., Ek, M. B., Barlage, M., et al. (2011). The community Noah land surface model with multiparameterization options (Noah-MP): 1. Model description and evaluation with local-scale measurements. *Journal of Geophysical Research: Atmospheres*, *116*(D12), D12109. https://doi.org/10.1029/2010JD015139

Oki, T., & Kanae, S. (2006). Global Hydrological Cycles and World Water Resources. *Science*, *313*(5790), 1068–1072. https://doi.org/10.1126/science.1128845

Oki, T., & Sud, Y. C. (1998). Design of Total Runoff Integrating Pathways (TRIP)—A Global River Channel Network. *Earth Interactions*, *2*(1), 1–37. https://doi.org/10.1175/1087-3562(1998)002<0001:DOTRIP>2.3.CO;2

Oleson, K., Lawrence, D. M., & Coauthors. (2013). Technical description of version 4.5 of the Community Land Model (CLM). *NCAR Technical Note NCAR/TN-503+STR*, 420 pp. https://doi.org/10.5065/D6RR1W7M

Onogi, K., Tsutsui, J., Koide, H., Sakamoto, M., Kobayashi, S., Hatsushika, H., et al. (2007). The JRA-25 Reanalysis. *Journal of the Meteorological Society of Japan. Ser. II*, *85*(3), 369–432. https://doi.org/10.2151/jmsj.85.369

Overgaard, J., Rosbjerg, D., & Butts, M. B. (2006). Land-surface modelling in hydrological perspective – a review. *Biogeosciences*, *3*(2), 229–241. https://doi.org/10.5194/bg-3-229-2006

Ozdogan, M., Rodell, M., Beaudoing, H. K., & Toll, D. L. (2010). Simulating the Effects of Irrigation over the United States in a Land Surface Model Based on Satellite-Derived Agricultural Data. *Journal of Hydrometeorology*, *11*(1), 171–184. https://doi.org/10.1175/2009JHM1116.1

Pail, R., Bingham, R., Braitenberg, C., Dobslaw, H., Eicker, A., Güntner, A., et al. (2015). Science and User Needs for Observing Global Mass Transport to Understand Global Change and to Benefit Society. *Surveys in Geophysics*, *36*(6), 743–772. https://doi.org/10.1007/s10712-015-9348-9

Pan, M., Cai, X., Chaney, N. W., Entekhabi, D., & Wood, E. F. (2016). An initial assessment of SMAP soil moisture retrievals using high-resolution model simulations and in situ observations. *Geophysical Research Letters*, *43*(18), 9662–9668. https://doi.org/10.1002/2016GL069964

Pan, Y., Zhang, C., Gong, H., Yeh, P. J.-F., Shen, Y., Guo, Y., et al. (2016). Detection of human-induced evapotranspiration using GRACE satellite observations in the Haihe River basin of China. *Geophysical Research Letters*, 2016GL071287. https://doi.org/10.1002/2016GL071287

Panday, S., Langevin, C. D., Niswonger, R. G., Ibaraki, M., & Hughes, J. D. (2013). *MODFLOW–USG version 1: An unstructured grid version of MODFLOW for simulating groundwater flow and tightly coupled processes using a control volume finite-difference formulation: U.S. Geological Survey Techniques and Methods*. book 6, chap. A45, 66 p., https://pubs.usgs.gov/tm/06/a45.

Pei, L., Moore, N., Zhong, S., Kendall, A. D., Gao, Z., & Hyndman, D. W. (2016). Effects of Irrigation on Summer Precipitation over the United States. *Journal of Climate*, *29*(10), 3541–3558. https://doi.org/10.1175/JCLI-D-15-0337.1

Peng, B., Guan, K., Chen, M., Lawrence, D. M., Pokhrel, Y., Suyker, A., et al. (2018). Improving maize growth processes in the community land model: Implementation and evaluation. *Agricultural and Forest Meteorology*, *250–251*, 64–89. https://doi.org/10.1016/j.agrformet.2017.11.012

Pitman, A. J. (2003). The evolution of, and revolution in, land surface schemes designed for climate models. *International Journal of Climatology*, *23*(5), 479–510. https://doi.org/10.1002/joc.893

Pokhrel, Y., Hanasaki, N., Koirala, S., Cho, J., Yeh, P. J.-F., Kim, H., et al. (2012). Incorporating Anthropogenic Water Regulation Modules into a Land Surface Model. *Journal of Hydrometeorology*, *13*(1), 255–269. https://doi.org/10.1175/JHM-D-11-013.1

Pokhrel, Y., Hanasaki, N., Yeh, P. J.-F., Yamada, T. J., Kanae, S., & Oki, T. (2012). Model estimates of sea-level change due to anthropogenic impacts on terrestrial water storage. *Nature Geoscience*, *5*(6), 389–392. https://doi.org/10.1038/ngeo1476

Pokhrel, Y., Fan, Y., Miguez-Macho, G., Yeh, P. J.-F., & Han, S.-C. (2013). The role of groundwater in the Amazon water cycle: 3. Influence on terrestrial water storage computations and comparison with GRACE. *Journal of Geophysical Research: Atmospheres*, *118*(8), 3233–3244. https://doi.org/10.1002/jgrd.50335

Pokhrel, Y., Fan, Y., & Miguez-Macho, G. (2014). Potential hydrologic changes in the Amazon by the end of the 21st century and the groundwater buffer. *Environmental Research Letters*, *9*(8), 084004. https://doi.org/10.1088/1748-9326/9/8/084004

Pokhrel, Y., Koirala, S., Yeh, P. J.-F., Hanasaki, N., Longuevergne, L., Kanae, S., & Oki, T. (2015). Incorporation of groundwater pumping in a global Land Surface Model with the representation of human impacts. *Water Resources Research*, *51*(1), 78–96. https://doi.org/10.1002/2014WR015602

Pokhrel, Y., Hanasaki, N., Wada, Y., & Kim, H. (2016). Recent progresses in incorporating human land–water management into global land surface models toward their integration into Earth system models. *Wiley Interdisciplinary Reviews: Water*, *3*(4), 548–574. https://doi.org/10.1002/wat2.1150

Pokhrel, Y., Felfelani, F., Shin, S., Yamada, T. J., & Satoh, Y. (2017). Modeling large-scale human alteration of land surface hydrology and climate. *Geoscience Letters*, *4*(1), 10. https://doi.org/10.1186/s40562-017-0076-5

Portmann, F. T., Siebert, S., & Döll, P. (2010). MIRCA2000—Global monthly irrigated and rainfed crop areas around the year 2000: A new high-resolution data set for agricultural and hydrological modeling. *Global Biogeochemical Cycles*, *24*(1), GB1011. https://doi.org/10.1029/2008GB003435

Qian, Y., Huang, M., Yang, B., & Berg, L. K. (2013). A Modeling Study of Irrigation Effects on Surface Fluxes and Land–Air–Cloud Interactions in the Southern Great Plains. *Journal of Hydrometeorology*, *14*(3), 700–721. https://doi.org/10.1175/JHM-D-12-0134.1

Rahman, M. M., Lu, M., & Kyi, K. H. (2015). Variability of soil moisture memory for wet and dry basins. *Journal of Hydrology*, *523*, 107–118. https://doi.org/10.1016/j.jhydrol.2015.01.033

Ramankutty, N., Evan, A. T., Monfreda, C., & Foley, J. A. (2008). Farming the planet: 1. Geographic distribution of global agricultural lands in the year 2000. *Global Biogeochemical Cycles*, *22*(1). https://doi.org/10.1029/2007GB002952

Reager, J. T., Thomas, B. F., & Famiglietti, J. S. (2014). River basin flood potential inferred using GRACE gravity observations at several months lead time. *Nature Geoscience*, *7*(8), 588–592. https://doi.org/10.1038/ngeo2203

Reager, J. T., Gardner, A. S., Famiglietti, J. S., Wiese, D. N., Eicker, A., & Lo, M.-H. (2016). A decade of sea level rise slowed by climate-driven hydrology. *Science*, *351*(6274), 699–703. https://doi.org/10.1126/science.aad8386

Reichle, R. H., & Koster, R. D. (2004). Bias reduction in short records of satellite soil moisture. *Geophysical Research Letters*, *31*(19). https://doi.org/10.1029/2004GL020938

Richards, L. A. (1931). CAPILLARY CONDUCTION OF LIQUIDS THROUGH POROUS MEDIUMS. *Journal of Applied Physics*, *1*(5), 318–333. https://doi.org/10.1063/1.1745010

Richey, A. S., Thomas, B. F., Lo, M.-H., Reager, J. T., Famiglietti, J. S., Voss, K., et al. (2015). Quantifying renewable groundwater stress with GRACE. *Water Resources Research*, *51*(7), 5217–5238. https://doi.org/10.1002/2015WR017349

Rietbroek, R., Brunnabend, S.-E., Kusche, J., Schröter, J., & Dahle, C. (2016). Revisiting the contemporary sea-level budget on global and regional scales. *Proceedings of the National Academy of Sciences*, *113*(6), 1504–1509. https://doi.org/10.1073/pnas.1519132113

Rodell, M., Famiglietti, J. S., Chen, J., Seneviratne, S. I., Viterbo, P., Holl, S., & Wilson, C. R. (2004). Basin scale estimates of evapotranspiration using GRACE and other observations. *Geophysical Research Letters*, *31*(20), L20504. https://doi.org/10.1029/2004GL020873

Rodell, M., Velicogna, I., & Famiglietti, J. S. (2009). Satellite-based estimates of groundwater depletion in India. *Nature*, *460*(7258), 999–1002. https://doi.org/10.1038/nature08238

Rodell, M., Famiglietti, J. S., Wiese, D. N., Reager, J. T., Beaudoing, H. K., Landerer, F. W., & Lo, M.-H. (2018). Emerging trends in global freshwater availability. *Nature*, 1. https://doi.org/10.1038/s41586-018-0123-1

Rosenberg, E. A., Clark, E. A., Steinemann, A. C., & Lettenmaier, D. P. (2013). On the contribution of groundwater storage to interannual streamflow anomalies in the Colorado River basin. *Hydrol. Earth Syst. Sci.*, *17*(4), 1475–1491. https://doi.org/10.5194/hess-17-1475-2013

de Rosnay, P., Polcher, J., Laval, K., & Sabre, M. (2003). Integrated parameterization of irrigation in the land surface model ORCHIDEE. Validation over Indian Peninsula. *Geophysical Research Letters*, *30*(19), 1986. https://doi.org/10.1029/2003GL018024

Russo, T. A., & Lall, U. (2017). Depletion and response of deep groundwater to climate-induced pumping variability. *Nature Geoscience*, *10*(2), 105–108. https://doi.org/10.1038/ngeo2883

Sabater, J. M., Jarlan, L., Calvet, J.-C., Bouyssel, F., & De Rosnay, P. (2007). From Near-Surface to Root-Zone Soil Moisture Using Different Assimilation Techniques. *Journal of Hydrometeorology*, *8*(2), 194–206. https://doi.org/10.1175/JHM571.1

Sacks, W. J., Cook, B. I., Buenning, N., Levis, S., & Helkowski, J. H. (2009). Effects of global irrigation on the near-surface climate. *Climate Dynamics*, *33*(2–3), 159–175. https://doi.org/10.1007/s00382-008-0445-z

Sakaguchi, K., & Zeng, X. (2009). Effects of soil wetness, plant litter, and under-canopy atmospheric stability on ground evaporation in the Community Land Model (CLM3.5). *Journal of Geophysical Research: Atmospheres*, *114*(D1). https://doi.org/10.1029/2008JD010834

Sakumura, C., Bettadpur, S., & Bruinsma, S. (2014). Ensemble prediction and intercomparison analysis of GRACE time-variable gravity field models. *Geophysical Research Letters*, *41*(5), 1389–1397. https://doi.org/10.1002/2013GL058632

Sanderson, B. M., Wehner, M., & Knutti, R. (2017). Skill and independence weighting for multi-model assessments. *Geoscientific Model Development*, *10*(6), 2379–2395. https://doi.org/10.5194/gmd-10-2379-2017

Save, H., Bettadpur, S., & Tapley, B. D. (2016). High-resolution CSR GRACE RL05 mascons. *Journal of Geophysical Research: Solid Earth*, *121*(10), 7547–7569. https://doi.org/10.1002/2016JB013007

Scanlon, B. R., Longuevergne, L., & Long, D. (2012). Ground referencing GRACE satellite estimates of groundwater storage changes in the California Central Valley, USA. *Water Resources Research*, *48*(4), W04520. https://doi.org/10.1029/2011WR011312

Scanlon, B. R., Faunt, C. C., Longuevergne, L., Reedy, R. C., Alley, W. M., McGuire, V. L., & McMahon, P. B. (2012). Groundwater depletion and sustainability of irrigation in the US High Plains and Central Valley. *Proceedings of the National Academy of Sciences*, *109*(24), 9320–9325. https://doi.org/10.1073/pnas.1200311109

Scanlon, B. R., Zhang, Z., Reedy, R. C., Pool, D. R., Save, H., Long, D., et al. (2015). Hydrologic implications of GRACE satellite data in the Colorado River Basin. *Water Resources Research*, *51*(12), 9891–9903. https://doi.org/10.1002/2015WR018090

Scanlon, B. R., Zhang, Z., Save, H., Wiese, D. N., Landerer, F. W., Long, D., et al. (2016). Global evaluation of new GRACE mascon products for hydrologic applications. *Water Resources Research*, *52*(12), 9412–9429. https://doi.org/10.1002/2016WR019494

Scanlon, B. R., Zhang, Z., Save, H., Sun, A. Y., Müller Schmied, H., van Beek, L. P. H., et al. (2018). Global models underestimate large decadal declining and rising water storage trends relative to GRACE satellite data. *Proceedings of the National Academy of Sciences*, 201704665. https://doi.org/10.1073/pnas.1704665115

Schaefer, G. L., Cosh, M. H., & Jackson, T. J. (2007). The USDA Natural Resources Conservation Service Soil Climate Analysis Network (SCAN). *Journal of Atmospheric and Oceanic Technology*, *24*(12), 2073–2077. https://doi.org/10.1175/2007JTECHA930.1

Schewe, J., Heinke, J., Gerten, D., Haddeland, I., Arnell, N. W., Clark, D. B., et al. (2014). Multimodel assessment of water scarcity under climate change. *Proceedings of the*

National Academy of Sciences, *111*(9), 3245–3250. https://doi.org/10.1073/pnas.1222460110

Sellers, P. J., Dickinson, R. E., Randall, D. A., Betts, A. K., Hall, F. G., Berry, J. A., et al. (1997). Modeling the Exchanges of Energy, Water, and Carbon Between Continents and the Atmosphere. *Science*, *275*(5299), 502–509. https://doi.org/10.1126/science.275.5299.502

Sheffield, J., Goteti, G., & Wood, E. F. (2006). Development of a 50-Year High-Resolution Global Dataset of Meteorological Forcings for Land Surface Modeling. *Journal of Climate*, *19*(13), 3088–3111. https://doi.org/10.1175/JCLI3790.1

Sheffield, J., Wood, E. F., Pan, M., Beck, H., Coccia, G., Serrat-Capdevila, A., & Verbist, K. (2018). Satellite Remote Sensing for Water Resources Management: Potential for Supporting Sustainable Development in Data-Poor Regions. *Water Resources Research*, *54*(12), 9724–9758. https://doi.org/10.1029/2017WR022437

Sippel, S., Zscheischler, J., Heimann, M., Otto, F. E. L., Peters, J., & Mahecha, M. D. (2015). Quantifying changes in climate variability and extremes: Pitfalls and their overcoming. *Geophysical Research Letters*, *42*(22), 9990–9998. https://doi.org/10.1002/2015GL066307

Sivapalan, M. (2018). From engineering hydrology to Earth system science: milestones in the transformation of hydrologic science. *Hydrol. Earth Syst. Sci.*, *22*(3), 1665–1693. https://doi.org/10.5194/hess-22-1665-2018

Smidt, S. J., Haacker, E. M. K., Kendall, A. D., Deines, J. M., Pei, L., Cotterman, K. A., et al. (2016). Complex water management in modern agriculture: Trends in the water-energy-food nexus over the High Plains Aquifer. *Science of The Total Environment*, *566–567*, 988–1001. https://doi.org/10.1016/j.scitotenv.2016.05.127

Sorooshian, S., Li, J., Hsu, K.-L., & Gao, X. (2011). How significant is the impact of irrigation on the local hydroclimate in California's Central Valley? Comparison of model results with ground and remote-sensing data. *Journal of Geophysical Research: Atmospheres*, *116*(D6), D06102. https://doi.org/10.1029/2010JD014775

Spence, C. (2002). Streamflow Variability (1965 to 1998) in Five Northwest Territories and Nunavut Rivers. *Canadian Water Resources Journal / Revue Canadienne Des Ressources Hydriques*, *27*(2), 135–154. https://doi.org/10.4296/cwrj2702135

St. Jacques, J.-M., & Sauchyn, D. J. (2009). Increasing winter baseflow and mean annual streamflow from possible permafrost thawing in the Northwest Territories, Canada. *Geophysical Research Letters*, *36*(1), L01401. https://doi.org/10.1029/2008GL035822

Stacke, T., & Hagemann, S. (2012). Development and evaluation of a global dynamical wetlands extent scheme. *Hydrology and Earth System Sciences*, *16*(8), 2915–2933. https://doi.org/10.5194/hess-16-2915-2012

Stieglitz, M., Rind, D., Famiglietti, J., & Rosenzweig, C. (1997). An Efficient Approach to Modeling the Topographic Control of Surface Hydrology for Regional and Global Climate Modeling. *Journal of Climate*, *10*(1), 118–137. https://doi.org/10.1175/1520-0442(1997)010<0118:AEATMT>2.0.CO;2

Swenson, S. C., & Lawrence, D. M. (2014). Assessing a dry surface layer-based soil resistance parameterization for the Community Land Model using GRACE and FLUXNET-MTE data. *Journal of Geophysical Research: Atmospheres*, *119*(17), 10,299-10,312. https://doi.org/10.1002/2014JD022314

Swenson, S. C., & Lawrence, D. M. (2015). A GRACE-based assessment of interannual groundwater dynamics in the Community Land Model. *Water Resources Research*, *51*(11), 8817–8833. https://doi.org/10.1002/2015WR017582

Syed, T. H., Famiglietti, J. S., Rodell, M., Chen, J., & Wilson, C. R. (2008). Analysis of terrestrial water storage changes from GRACE and GLDAS. *Water Resources Research*, *44*(2), W02433. https://doi.org/10.1029/2006WR005779

Takata, K., Emori, S., & Watanabe, T. (2003). Development of the minimal advanced treatments of surface interaction and runoff. *Global and Planetary Change*, *38*(1–2), 209–222. https://doi.org/10.1016/S0921-8181(03)00030-4

Tapley, B. D., Watkins, M. M., Flechtner, F., Reigber, C., Bettadpur, S., Rodell, M., et al. (2019). Contributions of GRACE to understanding climate change. *Nature Climate Change*, *9*(5), 358–369. https://doi.org/10.1038/s41558-019-0456-2

Taylor, K. E., Stouffer, R. J., & Meehl, G. A. (2011). An Overview of CMIP5 and the Experiment Design. *Bulletin of the American Meteorological Society*, *93*(4), 485–498. https://doi.org/10.1175/BAMS-D-11-00094.1

Taylor, R. G., Scanlon, B., Döll, P., Rodell, M., van Beek, R., Wada, Y., et al. (2013). Ground water and climate change. *Nature Climate Change*, *3*(4), 322–329. https://doi.org/10.1038/nclimate1744

Thomas, A. C., Reager, J. T., Famiglietti, J. S., & Rodell, M. (2014). A GRACE-based water storage deficit approach for hydrological drought characterization. *Geophysical Research Letters*, *41*(5), 1537–1545. https://doi.org/10.1002/2014GL059323

Tiwari, V. M., Wahr, J., & Swenson, S. (2009). Dwindling groundwater resources in northern India, from satellite gravity observations. *Geophysical Research Letters*, *36*(18), L18401. https://doi.org/10.1029/2009GL039401

Trancoso, R., Larsen, J. R., McVicar, T. R., Phinn, S. R., & McAlpine, C. A. (2017). CO2-vegetation feedbacks and other climate changes implicated in reducing base flow. *Geophysical Research Letters*, *44*(5), 2017GL072759. https://doi.org/10.1002/2017GL072759

Vahmani, P., & Hogue, T. S. (2014). Incorporating an Urban Irrigation Module into the Noah Land Surface Model Coupled with an Urban Canopy Model. *Journal of Hydrometeorology*, *15*(4), 1440–1456. https://doi.org/10.1175/JHM-D-13-0121.1

Veldkamp, T. I. E., Wada, Y., Aerts, J. C. J. H., Döll, P., Gosling, S. N., Liu, J., et al. (2017). Water scarcity hotspots travel downstream due to human interventions in the 20th and 21st century. *Nature Communications*, *8*, ncomms15697. https://doi.org/10.1038/ncomms15697

Vérant, S., Laval, K., Polcher, J., & De Castro, M. (2004). Sensitivity of the Continental Hydrological Cycle to the Spatial Resolution over the Iberian Peninsula. *Journal of Hydrometeorology*, *5*(2), 267–285. https://doi.org/10.1175/1525-7541(2004)005<0267:SOTCHC>2.0.CO;2

Vörösmarty, C. J., Fekete, B. M., Meybeck, M., & Lammers, R. (2000). A simulated topological network representing the global system of rivers at 30-minute spatial resolution (STN-30), *14*, 599–621.

Wada, Y., van Beek, L. P. H., van Kempen, C. M., Reckman, J. W. T. M., Vasak, S., & Bierkens, M. F. P. (2010). Global depletion of groundwater resources. *Geophysical Research Letters*, *37*(20), L20402. https://doi.org/10.1029/2010GL044571

Wada, Y., van Beek, L. P. H., Weiland, F. C. S., Chao, B. F., Wu, Y.-H., & Bierkens, M. F. P. (2012). Past and future contribution of global groundwater depletion to sea-level rise. *Geophysical Research Letters*, *39*(9). https://doi.org/10.1029/2012GL051230

Wada, Y., Wisser, D., & Bierkens, M. F. P. (2014). Global modeling of withdrawal, allocation and consumptive use of surface water and groundwater resources. *Earth Syst. Dynam.*, *5*(1), 15–40. https://doi.org/10.5194/esd-5-15-2014

Wada, Y., Wisser, D., Eisner, S., Flörke, M., Gerten, D., Haddeland, I., et al. (2015). Multimodel projections and uncertainties of irrigation water demand under climate change. *Geophysical Research Letters*, 4626–4632. https://doi.org/10.1002/grl.50686@10.1002/(ISSN)1944-8007.GRLCMIP5

Wada, Y., Lo, M.-H., Yeh, P. J.-F., Reager, J. T., Famiglietti, J. S., Wu, R.-J., & Tseng, Y.-H. (2016). Fate of water pumped from underground and contributions to sea-level rise. *Nature Climate Change*, *6*(8), 777–780. https://doi.org/10.1038/nclimate3001

Wada, Y., Bierkens, M. F. P., de Roo, A., Dirmeyer, P. A., Famiglietti, J. S., Hanasaki, N., et al. (2017). Human–water interface in hydrological modelling: current status and future directions. *Hydrology and Earth System Sciences*, *21*(8), 4169–4193. https://doi.org/10.5194/hess-21-4169-2017

Wagner, W., Lemoine, G., & Rott, H. (1999). A Method for Estimating Soil Moisture from ERS Scatterometer and Soil Data. *Remote Sensing of Environment*, *70*(2), 191–207. https://doi.org/10.1016/S0034-4257(99)00036-X

Wahr, J., Molenaar, M., & Bryan, F. (1998). Time variability of the Earth's gravity field: Hydrological and oceanic effects and their possible detection using GRACE. *Journal of Geophysical Research: Solid Earth*, *103*(B12), 30205–30229. https://doi.org/10.1029/98JB02844

Wahr, J., Swenson, S., & Velicogna, I. (2006). Accuracy of GRACE mass estimates. *Geophysical Research Letters*, *33*(6), L06401. https://doi.org/10.1029/2005GL025305

Wang, S., Pan, M., Mu, Q., Shi, X., Mao, J., Brümmer, C., et al. (2015). Comparing Evapotranspiration from Eddy Covariance Measurements, Water Budgets, Remote Sensing, and Land Surface Models over Canada. *Journal of Hydrometeorology*, *16*(4), 1540–1560. https://doi.org/10.1175/JHM-D-14-0189.1

Wang, S., Huang, J., Yang, D., Pavlic, G., & Li, J. (2015). Long-term water budget imbalances and error sources for cold region drainage basins. *Hydrological Processes*, *29*(9), 2125–2136. https://doi.org/10.1002/hyp.10343

Warszawski, L., Frieler, K., Huber, V., Piontek, F., Serdeczny, O., & Schewe, J. (2014). The Inter-Sectoral Impact Model Intercomparison Project (ISI–MIP): Project framework. *Proceedings of the National Academy of Sciences*, *111*(9), 3228–3232. https://doi.org/10.1073/pnas.1312330110

Watanabe, T. (1994). Bulk parameterization for a vegetated surface and its application to a simulation of nocturnal drainage flow. *Boundary-Layer Meteorology*, *70*(1), 13–35. https://doi.org/10.1007/BF00712521

Watkins, M. M., Wiese, D. N., Yuan, D.-N., Boening, C., & Landerer, F. W. (2015). Improved methods for observing Earth's time variable mass distribution with GRACE using spherical cap mascons. *Journal of Geophysical Research: Solid Earth*, *120*(4), 2014JB011547. https://doi.org/10.1002/2014JB011547

Weedon, G. P., Balsamo, G., Bellouin, N., Gomes, S., Best, M. J., & Viterbo, P. (2014). The WFDEI meteorological forcing data set: WATCH Forcing Data methodology applied to ERA-Interim reanalysis data. *Water Resources Research*, *50*(9), 7505–7514. https://doi.org/10.1002/2014WR015638

Wei, J., Dirmeyer, P. A., Wisser, D., Bosilovich, M. G., & Mocko, D. M. (2012). Where Does the Irrigation Water Go? An Estimate of the Contribution of Irrigation to Precipitation Using MERRA. *Journal of Hydrometeorology*, *14*(1), 275–289. https://doi.org/10.1175/JHM-D-12-079.1

Werth, S., Güntner, A., Schmidt, R., & Kusche, J. (2009). Evaluation of GRACE filter tools from a hydrological perspective. *Geophysical Journal International*, *179*(3), 1499–1515. https://doi.org/10.1111/j.1365-246X.2009.04355.x

Wiese, D. N., Landerer, F. W., & Watkins, M. M. (2016). Quantifying and reducing leakage errors in the JPL RL05M GRACE mascon solution: GRACE JPL RL05M LEAKAGE

ERROR REDUCTION. *Water Resources Research*, *52*(9), 7490–7502. https://doi.org/10.1002/2016WR019344

Williamson, A. K., Prudic, D. E., & Swain, L. A. (1989). Ground-water flow in the Central Valley, California. *United States Geological Survey, Professional Paper; (USA)*, *1401-D*. Retrieved from https://www.osti.gov/biblio/6265446

Wu, W., & Dickinson, R. E. (2004). Time Scales of Layered Soil Moisture Memory in the Context ofLand–Atmosphere Interaction. *Journal of Climate*, *17*(14), 2752–2764. https://doi.org/10.1175/1520-0442(2004)017<2752:TSOLSM>2.0.CO;2

Xia, Y., Mitchell, K., Ek, M., Sheffield, J., Cosgrove, B., Wood, E., et al. (2012). Continental-scale water and energy flux analysis and validation for the North American Land Data Assimilation System project phase 2 (NLDAS-2): 1. Intercomparison and application of model products. *Journal of Geophysical Research: Atmospheres*, *117*(D3). https://doi.org/10.1029/2011JD016048

Xie, H., Longuevergne, L., Ringler, C., & Scanlon, B. R. (2012). Calibration and evaluation of a semi-distributed watershed model of Sub-Saharan Africa using GRACE data. *Hydrology and Earth System Sciences*, *16*(9), 3083–3099. https://doi.org/10.5194/hess-16-3083-2012

Xie, Z., Liu, S., Zeng, Y., Gao, J., Qin, P., Jia, B., et al. (2018). A High-Resolution Land Model With Groundwater Lateral Flow, Water Use, and Soil Freeze-Thaw Front Dynamics and its Applications in an Endorheic Basin. *Journal of Geophysical Research: Atmospheres*, *123*(14), 7204–7222. https://doi.org/10.1029/2018JD028369

Yamada, T., & Pokhrel, Y. (2019). Effect of Human-Induced Land Disturbance on Subseasonal Predictability of Near-Surface Variables Using an Atmospheric General Circulation Model. *Atmosphere, in Revision*.

Yang, Z.-L., Niu, G.-Y., Mitchell, K. E., Chen, F., Ek, M. B., Barlage, M., et al. (2011). The community Noah land surface model with multiparameterization options (Noah-MP): 2. Evaluation over global river basins. *Journal of Geophysical Research: Atmospheres*, *116*(D12), D12110. https://doi.org/10.1029/2010JD015140

Yilmaz, M. T., Anderson, M. C., Zaitchik, B., Hain, C. R., Crow, W. T., Ozdogan, M., et al. (2014). Comparison of prognostic and diagnostic surface flux modeling approaches over the Nile River basin. *Water Resources Research*, *50*(1), 386–408. https://doi.org/10.1002/2013WR014194

Zaitchik, B. F., Rodell, M., & Reichle, R. H. (2008). Assimilation of GRACE Terrestrial Water Storage Data into a Land Surface Model: Results for the Mississippi River Basin. *Journal of Hydrometeorology*, *9*(3), 535–548. https://doi.org/10.1175/2007JHM951.1

Zeng, N., Yoon, J.-H., Mariotti, A., & Swenson, S. (2008). Variability of Basin-Scale Terrestrial Water Storage from a PER Water Budget Method: The Amazon and the Mississippi. *Journal of Climate*, *21*(2), 248–265. https://doi.org/10.1175/2007JCLI1639.1

Zeng, X., & Decker, M. (2009). Improving the Numerical Solution of Soil Moisture–Based Richards Equation for Land Models with a Deep or Shallow Water Table. *Journal of Hydrometeorology*, *10*(1), 308–319. https://doi.org/10.1175/2008JHM1011.1

Zeng, Y., Xie, Z., Yu, Y., Liu, S., Wang, L., Zou, J., et al. (2016). Effects of anthropogenic water regulation and groundwater lateral flow on land processes. *Journal of Advances in Modeling Earth Systems*, *8*(3), 1106–1131. https://doi.org/10.1002/2016MS000646

Zeng, Y., Xie, Z., Liu, S., Xie, J., Jia, B., Qin, P., & Gao, J. (2018). Global Land Surface Modeling Including Lateral Groundwater Flow. *Journal of Advances in Modeling Earth Systems*, *10*(8), 1882–1900. https://doi.org/10.1029/2018MS001304

Zhang, X. F., Zhang, T., Zhou, P., Shao, Y., & Gao, S. (2017). Validation Analysis of SMAP and AMSR2 Soil Moisture Products over the United States Using Ground-Based Measurements. *Remote Sensing*, *9*(2), 104. https://doi.org/10.3390/rs9020104

Zhang, X. Z., Xiong, Z., & Tang, Q. (2017). Modeled effects of irrigation on surface climate in the Heihe River Basin, Northwest China. *Journal of Geophysical Research: Atmospheres*, 2017JD026732. https://doi.org/10.1002/2017JD026732

Zhao, F., Veldkamp, T., Frieler, K., Schewe, J., Ostberg, S., Willner, S., et al. (2017). Choice of routing scheme considerably influences peak river discharge simulation in global hydrological models. *Environmental Research Letters*.

Zhao, M., A, G., Velicogna, I., & Kimball, J. S. (2017). Satellite Observations of Regional Drought Severity in the Continental United States Using GRACE-Based Terrestrial Water Storage Changes. *Journal of Climate*, *30*(16), 6297–6308. https://doi.org/10.1175/JCLI-D-16-0458.1

Zhou, L., Tian, Y., Myneni, R. B., Ciais, P., Saatchi, S., Liu, Y. Y., et al. (2014). Widespread decline of Congo rainforest greenness in the past decade. *Nature*, *509*(7498), 86–90. https://doi.org/10.1038/nature13265